The Breakup Reactions of Polarized ^7Li

Thesis

Submitted by

Claire Heather Shepherd–Themistocleous, B.A.

for the degree of

Doctor of Philosophy

Department of Physics
University of Edinburgh

August 1991

I would like to dedicate this thesis to my parents.

Abstract

This thesis describes an investigation of the breakup of 70MeV polarized ^{7}Li on a ^{120}Sn target. The reaction of primary interest is the direct breakup of ^{7}Li into an α and a t.

The analysing power $^{T}T_{20}$ has been measured for this reaction for angles ranging between 9° and 25°. The data between 9° and 15° was found to agree with a semi-classical calculation for $^{T}T_{20}$ which assumed that $\lambda = 1$ for the breakup. This implies that at these angles the direct breakup reaction is a Coulomb one.

This method of investigation of the reaction mechanism is an improvement on the previously used method of measuring differential cross sections. Analysing powers are inherently more sensitive measures of deviations from assumptions that are made in reaction models and should therefore enable a more accurate test of the mechanism in question than differential cross sections would allow. The greatly reduced possibility of systematic errors and the requirement of relative rather than absolute yields are also major advantages of analysing powers over differential cross sections.

The analysing powers of the sequential breakup of ^{7}Li and the transfer breakup reactions $^{120}Sn(^{7}Li, \alpha + d)^{121}Sn_{g.s.,0.06}$ and $^{120}Sn(^{7}Li, \alpha + \alpha)^{119}In_{g.s.,0.31}$ were also measured. A comparison of the sequential breakup data with a semi-classical calculation did not provide any evidence for a Coulomb dominated process. Calculations do not at present exist for the transfer breakup reactions, but qualitative explanations of the sign and angular distribution of the analysing power $^{T}T_{20}$ have been proposed.

Declaration

The data discussed in this thesis unless otherwise stated was obtained by myself and other members of the Edinburgh Nuclear Physics Group. The analysis and interpretation of the data are entirely my own work and this thesis was written by myself.

Acknowledgements

I would like to thank :-

- My supervisors Prof. A. C. Shotter and Dr. N. J. Davis for all their help.
- Prof. R.C. Johnson for all his help.
- All the past and present members of the Edingburgh Nuclear Physics Group whose help and encouragment was invaluable.
- Dr. E. Garman whose tutorials gave me a love of Nuclear Physics.
- Prof. A. C. Shotter and Prof. Cowley for the use of the J.C.M.B. facilities.
- The staff of the N.S.F. for beam etc. .
- The S.E.R.C. for their studentship.
- and last but by no means least my parents for everything.

Contents

1 Introduction 1

1.1 Terminology 3

1.2 Review of Experimental and Theoretical Data 4

1.2.1 Light Ions 5

1.2.2 Light-Heavy Ions 6

1.2.3 The Serber Model 13

1.2.4 Coulomb Excitation 14

1.2.5 Born Approximations 16

1.2.6 The Adiabatic Approximation 20

1.2.7 Coupled Discretized Continuum Channels (CDCC) 22

1.3 Aims and Outline 24

2 Theory 25

2.1 Introduction 25

2.2 Coordinate Systems 25

2.3 Polarization 26

2.4 Analysing Powers 31

2.5 Calculation for Analysing Powers 33

2.6 Advantages and Disadvantages of Analysing Powers 37

2.7 Cross sections 40

2.8 Kinematics 42

3 Experimental Method 47

3.1 Introduction 47

3.2 The Polarized Source 47

3.3 Accelerator and Beam Line 52

3.4 Targets 54

3.5 Detection System 54

3.6 Detectors 57

3.6.1 Charge Sharing in Strip Detectors 58

3.6.2 Problems with Si(Li) Detectors 61

3.7 Polarimeter 64

3.8 Data Acquisition Hardware 64

3.8.1 Electronics 64

3.8.2 The Event Manager 69

3.8.3 Computers 69

3.8.4 Software 70

4 The Monte Carlo code 74

4.1 Introduction 74

4.2 Description of monte_7Li.c 74

4.3 Applications of the Monte Carlo code 77

5 Data Analysis and Results 78

5.1 Determination of Beam Polarization 78

5.2 The Wien Filter Curve 82

5.3 Analysis Procedure 84

5.4 Analysing Power Determination and Errors 85

5.5 Differential Cross section Determination 87

5.6 Discussion of Data 89

5.6.1 α t Coincidence Data 89

5.6.2 α d Coincidence Data 108

5.6.3 α α Coincidence Data 114

6 Summary and Conclusion **120**

6.1 Future Work 124

A Data Tabulation **127**

A.1 Analysing power $^{T}T_{20}$ 127

A.2 Differential cross sections 130

References **132**

Chapter 1

Introduction

This thesis describes an investigation of the breakup of ^7Li on ^{120}Sn using a 10MeV/A polarized beam. The mechanism resulting in the direct breakup of ^7Li into an α and a t at forward angles is of primary interest, however data resulting from transfer breakup reactions will also be discussed.

The earliest work on breakup reactions was conducted by Oppenheimer and Phillips [Op35a, Op35b] using deuterons. The observations of beam velocity bumps of neutrons by Helmholtz et al. [He47] prompted Serber [Se47] to develop a model invoking the breakup of the deuterons as the origin of these neutrons. Subsequent experiments have involved the use of a variety of heavier projectiles such as ^3He, ^4He [Me85], ^6Li and ^7Li [Ca80, Da87]. In all cases broad continuous spectra centred around the beam velocity have been observed for a variety of fragments i.e. p, d, t, ^3He and ^4He. A large fraction of these yields has been identified as resulting from the breakup of the projectiles. Most work on breakup reactions has resulted from a desire to understand mechanisms contributing to inclusive spectra such as that in figure 1.1. At high energies one can see discrete peaks resulting from low energy excitations of the residual nucleus. At lower energies the spectrum consists of a featureless continuum. This continuum results from the excitation of broad high energy states and from processes, such as breakup, resulting in three or more bodies in the final state.

Since the establishment of the breakup mode of reaction a great deal of work

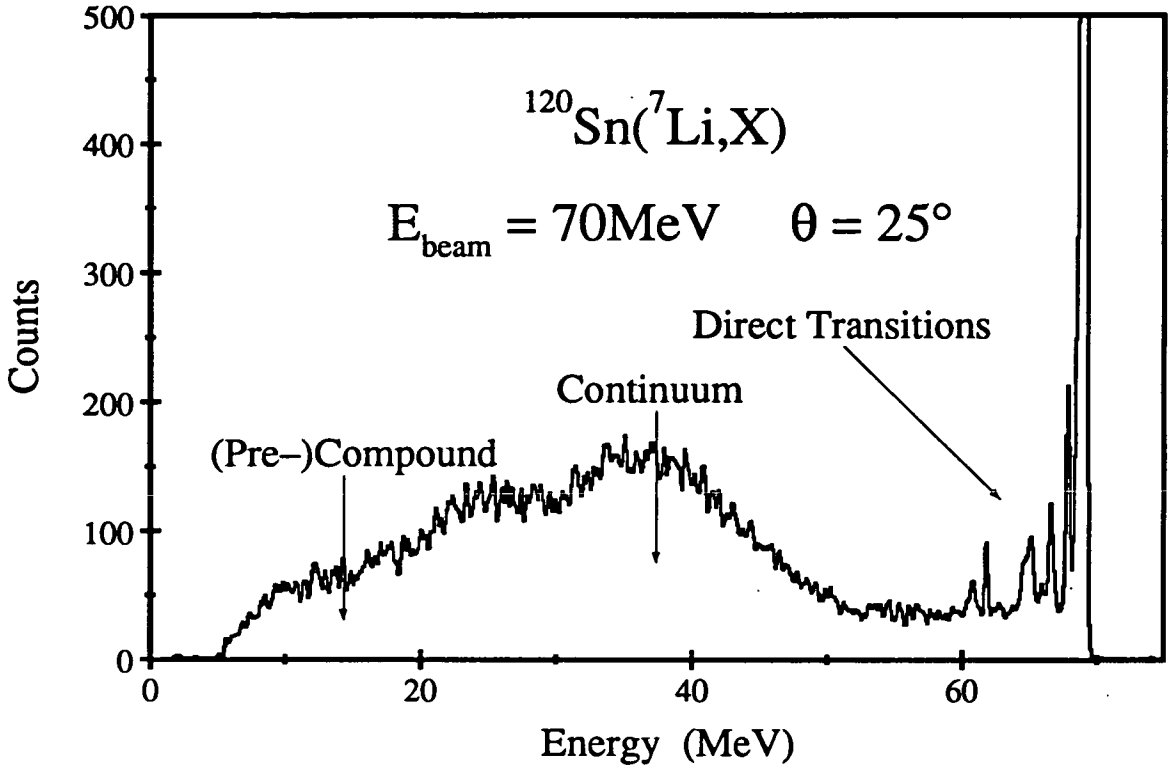

Figure 1.1: *Inclusive energy spectrum for the reaction* $^{120}Sn(^{7}Li, X)$ *illustrating the various contributions to the total yield.*

has gone into developing models to explain these processes. Some of the models will be briefly explained in subsequent sections. The proper inclusion of breakup channels is required to model such seemingly simple processes as elastic scattering of such nuclei as ^{6}Li and ^{7}Li which have low breakup thresholds[1]. The CDCC, coupled discretized continuum channels, model [Sa86] has met with considerable success, being able to model the elastic scattering of these projectiles without the need to resort to renormalization of the potential. Breakup calculations have however proved to be fraught with difficulties particularly when attempting to include both nuclear and Coulomb potentials in the interactions.

The work in this thesis was inspired by the work of Shotter et al. [Sh81, Sh84] on the direct breakup of ^{7}Li. This work suggested that at forward angles the observed direct breakup was due to the Coulomb interaction. Various models such as the CDCC and the adiabatic approximation, have been used in an attempt to

[1] For $^{6}Li \rightarrow \alpha + d$ and $^{7}Li \rightarrow \alpha + t$ these are 1.475MeV and 2.468MeV respectively.

explain this data and though meeting with some success when only using a nuclear potential have failed to include a Coulomb one successfully.

The present work is designed to be a further and more exacting probe of the breakup mechanism of ^7Li than differential cross section determination allows. In this work the analysing power $^7T_{20}$ is determined for the breakup of ^7Li. Analysing powers are quantities which are more sensitive than cross sections to reaction mechanisms and the forces involved, (see section 2.6) because unlike cross sections they depend on interference terms between scattering amplitudes.

Breakup reactions can also in principle provide information on the inverse i.e. fusion reaction. The $\alpha(t,\gamma)^7Li$ reaction is important in the creation of ^7Li in the Big Bang standard model. The acquisition of data via fusion reactions for low relative energies is very difficult because of the Coulomb repulsion between the participants resulting in cross sections of the order of μb. These energies are far more accessible via breakup reactions where this problem does not arise. Information on the fusion reaction can only be obtained however from the Coulomb component of the breakup reaction, necessitating a detailed knowledge of the reaction mechanism involved in breakup. The problems apparent at the present time have been reviewed by Shotter and Nagarajan [Sh88b, Sh90, Sh91].

1.1 Terminology

Some ambiguity exists in the terminology used when refering to breakup reactions. The contentious terms and the definitions pertaining to them in this thesis are listed below. These definitions are not in any way claimed to be definitive, but are merely the meanings intended within this thesis.

Breakup A reaction for which the final state consists of three or more bodies.

Sequential Breakup This type of breakup occurs via two distinct processes. The projectile is excited into a discrete energy state, this state then dissociates into two fragments at a distance from the nucleus such that the final state interactions

of these fragments with the nucleus are insignificant.

Direct Breakup This type of breakup is not easily separable into distinct processes. The projectile is not excited to a discrete state but dissociates into two fragments close to the target nucleus. Interactions between the fragments and the target are thus possible and probable.

Transfer A reaction whereby the projectile either accepts or donates a particle from or to the target. The particle refered to may comprise one or more nucleons.

Transfer Breakup A transfer reaction followed by the fragmentation of the resulting nucleus which may exist in its ground, if unstable to particle emission, or an excited state e.g. $(^7Li, ^8Be \rightarrow \alpha + \alpha)$.

Elastic Breakup A breakup reaction in which all the particles in the final state are in their ground states.

Inelastic Breakup A breakup reaction in which some or all of the particles in the final state are not in their ground states. The target like fragment is the one that is most usually excited.

Final State Interactions The interactions between any of the particles finally resulting from the reaction. The most usual interactions considered are those between the breakup fragments and the residual nucleus.

1.2 Review of Experimental and Theoretical Data

Experiments on the breakup of ions have been performed since $\sim$ 1935. The earliest experiments dealt with the simplest ions i.e. deuterons. The later study of more complex ions e.g. He has revealed a greater variety of types of reaction. A comprehensive review of the breakup reactions of He projectiles by de Meijer

and Kamermans [Me85] describes all the basic reaction paths for breakup. Work on heavy ions, not surprisingly, results in more complex final states. The reaction channels elucidated upon in the above paper though still apply. A brief review of these reaction channels will therefore be given below. In the section on light-heavy ions work done on ions such as ^6Li, ^7Li etc. will be reviewed.

1.2.1 Light Ions

The first breakup reactions were performed using deuterons [Op35a, Op35b]. Work done by Jarczyk and Lang [Ja73] at energies below the Coulomb barrier on the reaction $d \longrightarrow p + n$ implies that the breakup is due to a Coulomb interaction. Including a nuclear interaction in the form of a neutron target final state interaction in a post DWBA analysis by Baur and Trautmann resulted in very good agreement between theory and data [Ba76].

At energies above the Coulomb barrier the nuclear interaction between the projectile and the target must be taken into account. Work at energies above the Coulomb barrier (56 MeV) has been done by Matsuoka et al. [Ma82]. A prior form DWBA calculation had some success with low momentum transfer data, but failed at higher momentum transfers. The inclusion of nuclear interactions is thus seen to be far from trivial even with the simplest possible ion, the deuteron.

In the paper by de Meijer and Kamermans both direct breakup and processes involving an intermediate nucleus have been identified for ^3He and ^4He projectiles. The latter type of process though has only been observed to take place after a transfer reaction for ^3He. Examples of these reactions are :-

$(^3He, ^2He \rightarrow p + p)$
$(^3He, d \rightarrow p + n)$
$(\alpha, ^5Li \rightarrow \alpha + p)$
$(\alpha, ^2He \rightarrow p + p)$
$(\alpha, ^7Li^* \rightarrow \alpha + t)$

The absence of observation of sequential breakup of ^3He can be attributed to the

lack of any well defined excited states.

Similar direct breakup processes are observed for both ^3He and ^4He projectiles. Extensive coincidence studies have been carried out using ^3He projectiles (see [Me85] and references therein). Inclusive spectra show bumps occuring near an energy which corresponds to the beam velocity. This implies that the reaction process is fast, resulting in the detected fragment leaving the vicinity of the target nucleus in a relatively undisturbed condition. This fragment is then termed the spectator and the fragment that interacts with the nucleus is the participant.

The participant target interactions correspond to well known processes like elastic scattering, inelastic scattering, particle transfer and absorption. These processes are shown schematically for a ^7Li nucleus in figure 1.2. The breakup transfer and transfer breakup processes result in the same products, but are kinematically distinguishable. This is because the energies of the t and p in transfer breakup are limited by the distinct states of the intermediate $^4He^*$. Within the terminology used here the breakup transfer interaction would be termed a direct process whilst the transfer breakup would be a sequential process. These events are distinguished by using a 2D plot of the energies of the breakup products. The use of these plots is described in section 2.8. The absorptive breakup process is one in which the proton is initially absorbed by the nucleus and is then emitted from the equilibrium or pre-equilibrium state, whilst the d continues on relatively undisturbed. These types of events appear on a 2D plot as a mass of events which do not correspond to any particular locus.

These observations provide information on the basic reaction mechanisms of breakup processes. More complicated projectiles are found to undergo similar processes which are discussed in the next section.

1.2.2 Light-Heavy Ions

Light-heavy ions are found to undergo breakup in a similar way to light ions. The most extensively studied ions are ^6Li and ^7Li. The breakup of these ions reflects the loosely bound cluster structures of their ground states.

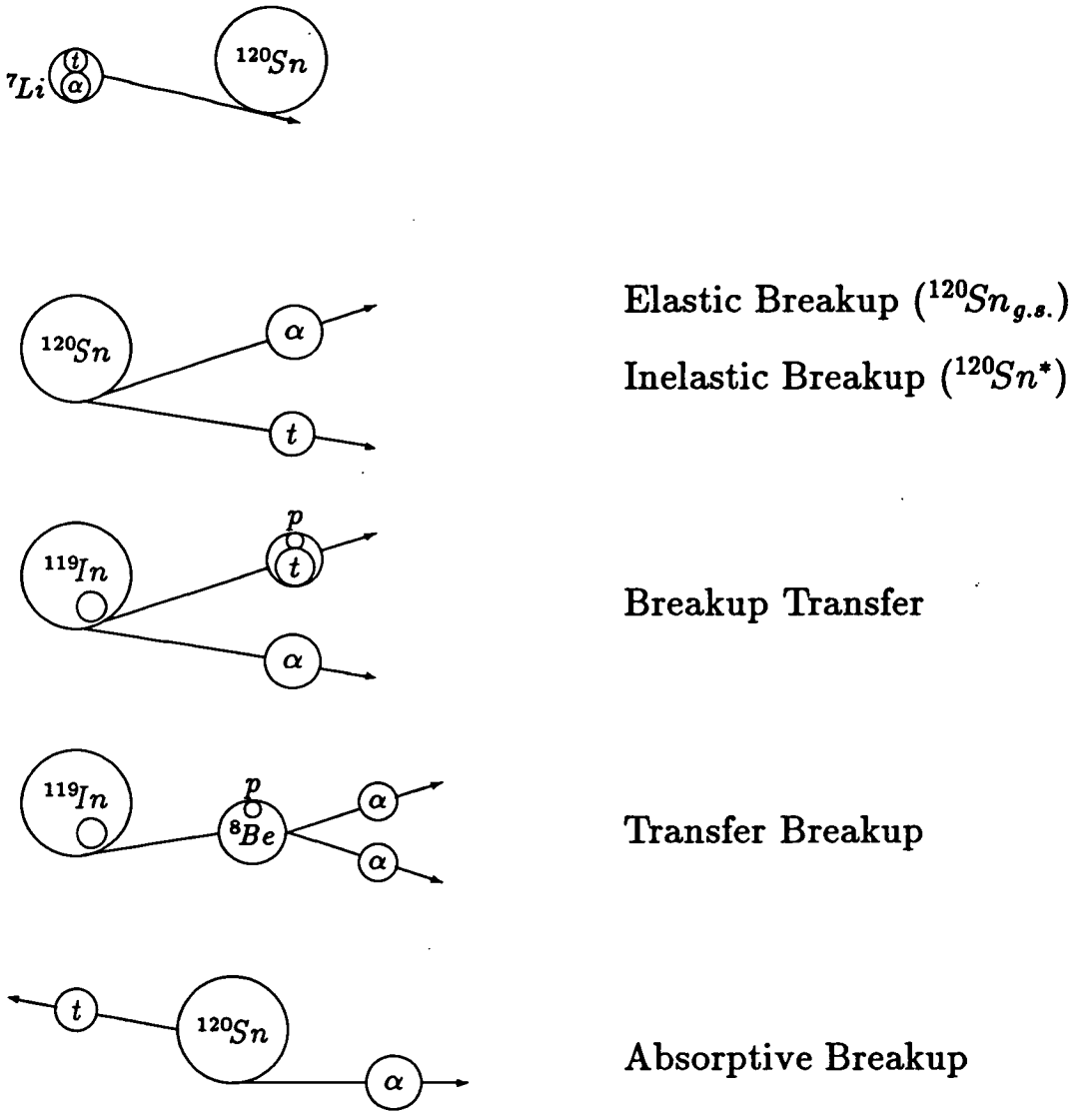

Figure 1.2: *Schematic diagrams of various possible breakup processes for ^{7}Li. (N.B. Not all of these processes are observed.)*

Reactions initiated by ^{6}Li have been studied at energies around (22-30MeV on ^{118}Sn and ^{208}Pb [Os74] [Sc77]) and well above (75MeV on ^{197}Au [Ca80]) the Coulomb barrier. Inclusive data shows a broad bump in the spectra for p, d, t,^{3}He and ^{4}He centred at energies corresponding to the beam velocity. These yields also show an $A^{1/3}$ target mass dependence suggesting a peripheral mechanism for the production of the detected particles.

The absence of a dependence on target mass of the relative particle yields implies that the particle production is a reflection of the projectile structure. These observations are also found to apply to ^7Li initiated reactions [Da87].

Data from reactions initiated by ^6Li have revealed five main reaction channels.

1. The sequential breakup of ^6Li to an α and a d via its 2.18MeV 3^+ excited state.

2. The direct breakup of ^6Li into an α and a d.

3. The transfer of a neutron from ^6Li to the target followed by the breakup of $^5Li_{g.s.}$ to an α and a p.

4. The transfer of a d from the target to ^6Li followed by the breakup of $^8Be_{g.s.,3.04MeV}$ into two αs.

5. The fusion of part of the ^6Li with the target, the remainder behaving as a spectator. This process is known as incomplete fusion.

The first four mechanisms were identified from particle particle coincidences and the last from particle prompt γ coincidences. In the last case the detected particles had energies commensurate with the beam velocity suggesting that they did not take part in the interaction. At sub-Coulomb energies the sequential breakup process has been found to dominate, but super-Coulomb energies allow the nuclear interaction to increase in importance causing other reaction channels to become more significant.

^7Li undergoes similar reactions to ^6Li. Shotter et al. have observed the sequential breakup into an α and a t of 70MeV ^7Li on ^{12}C and ^{208}Pb [Sh81] and on ^{120}Sn [Sh84]. Davinson [Da87] has observed sequential breakup on ^{12}C, ^{96}Zr, ^{120}Sn and ^{208}Pb targets and has also identified transfer breakup reactions similar to those undergone by ^6Li e.g. ($^7Li, ^8Be^*_{g.s.,3.04MeV} \rightarrow \alpha + \alpha$), ($^7Li, ^6Li^*_{2.18MeV} \rightarrow \alpha + d$) Breakup transfer reactions however, as for ^6Li initiated reactions were not seen. ^7Li was also seen to undergo the following incomplete fusion reactions.

$^{120}Sn, ^{208}Pb$ $(^7Li, \alpha x n \gamma)$

$(^7Li, t x n \gamma)$

$(^7Li, d x n \gamma)$

where x is a number. This interaction was found to account for a significant fraction of the inclusive yields of the relevant particles.

The reaction of most interest to this thesis i.e. the direct breakup of ^7Li was first identified by Shotter et al. [Sh81]. α t coincidence events were identified at energies kinematically inaccessible to a breakup reaction proceeding via an excited state of ^7Li. This process was only seen for the ^{208}Pb target and the yield was peaked at forward angles. Later work [Sh84, Da87] also identified this process for ^{96}Zr, ^{120}Sn targets, but also saw no evidence for direct breakup on a ^{12}C target.

The dominance of direct breakup at forward angles led Shotter et al. to suggest that the breakup was mainly due to the differential Coulomb force experienced by the cluster constituents of the projectile. They used the semi-classical model described in section 1.2.4 and good agreement with the data was found at forward angles, but it was overpredicted at backward angles. They also used a Monte Carlo code to predict the shape of the experimental projected energy spectra and good agreement was found. This model has been further tested by Shotter et al. [Sh88a] for a variety of targets (^{96}Zr, ^{120}Sn and ^{208}Pb) and at several energies (50, 60 and 70MeV). The model was found to fit the ^{96}Zr and ^{120}Sn data well, but the ^{208}Pb data was underpredicted by a factor of two. The discrepancy was attributed to the greater importance of the nuclear interaction for ^{208}Pb because the nuclear interaction, being a peripheral phenomenon, would be expected to vary as $A^{1/3}$ thus being of greater importance for the more massive target.

Work on the breakup of ^7Li has also been performed by Utsunomiya et al. [Ut88, Ut90]. They used an Enge Split Pole Spectrograph instead of telescope pairs to detect the α and t breakup fragments in coincidence. This type of experiment enables the detection of particles which have zero relative energy, a feat

not possible when using a telescope configuration of detectors. The problem of coping with a high flux of elastically scattered ^7Li at small scattering angles is also overcome. The use of a spectrograph does however impose restrictions on the coincidence phase space that is observable.

The ability to detect particles at a relative energy (ε) of zero enables an interesting test of final state interactions. If no such interactions between the projectile fragments and the target exist then the minima in the energy spectra of particles detected in coincidence and gated on a particular state of the recoil nucleus, henceforward refered to as projected energy spectra (see section 2.8), should occur at energies of $4E_{SUM}/7$ and $3E_{SUM}/7$ respectively, where E_{SUM} is the the sum of the α and t detected energies for a particular state of the recoil nucleus. If final state interactions do occur the α and t will undergo different accelerations in the Coulomb field because of their different charge to mass ratios hence shifting the position of the minimum. Utsunomiya et al. find no evidence for such a shift and suggest that the dissociation of the α and t must therefore take place at some distance from the target. The location of the minimum is however not a simple task. The differential cross section in this region is very small resulting in a small number of counts in this part of spectrum and phase space limitations of the system only allow the detection of αs and ts which are forward and backward going in the projectile frame, to a maximum relative energy of about 200keV. This latter restriction makes it impossible to ascertain whether the asymmetry in the projected energy spectra observed by Shotter et al. [Sh81], which is evidence for final state interactions, exists. These two limitations make the location of the minimum difficult.

Utsunomiya et al. extract cross sections of the form $d^3\sigma/d\varepsilon d\Omega_{Li} d\Omega_{\alpha-t}$ by using the kinematical transformations described by Fuchs [Fu82]. They compare this data to a Coulomb calculation and find that there is some disagreement between the two for $\varepsilon \lesssim$ 500keV. The data presented in [Ut88] was however shown by E.W.Macdonald [Ma89] to be wanting. Macdonald showed that when the extracted data was used in conjunction with a Monte Carlo code the original raw

data in the form of a projected energy spectrum could not be reproduced, but when the Coulomb model was used to calculate the input to the Monte Carlo code the reproduction of the observed projected energy spectrum was very good. In the later paper [Ut90], the data was revised and the major inaccuracies have probably been removed. The accuracy of the kinematical transformation is however impaired by the existence of a large detection system solid angle. In the later paper Utsunomiya et al. show that the effect of assuming different opening angles between the outgoing fragments is most marked at energies around and below 500keV which is the region in which they noted a difference between their Coulomb calculation and data. The spectrograph method for studying particle particle correlations overcomes many of the problems encountered when using telescopes, though it does have a phase space disadvantage. Caution however needs to be exerted when using the kinematical method to extract differential cross sections.

Various other calculations have been performed, but none have met with unqualified success. A prior DWBA calculation performed by Thompson et al. [Th83] (see section 1.2.5) overpredicted the data for both nuclear and nuclear + Coulomb potentials. An adiabatic model [Th83] was found to agree well with the data when only a nuclear potential was used, but a nuclear + Coulomb potential overpredicted the data by factor of ~ 3 (see section 1.2.6).

The CDCC model (see section 1.2.7) has been applied to both sequential and direct breakup of ^{7}Li. Good fits were obtained to the sequential breakup data for ^{120}Sn and ^{12}C targets using a nuclear potential only. The inclusion of a Coulomb potential however overpredicted the data for ^{120}Sn and ^{208}Pb targets by factors of 3 and 4 respectively though there was an improvement in the phase. Direct breakup calculations were found to fit the data for ^{120}Sn well, but a substantial cross section, which is not experimentally observed, was predicted for the ^{12}C target. This problem is as yet unresolved, but it is thought that large final state interactions may be responsible for the discrepancy. Unfortunately no calculations including a Coulomb interaction exist for direct breakup. The long range nature

of the Coulomb force makes it particularly difficult to include in this type of calculation.

The breakup of particles heavier than ^7Li often results in final states of four or more bodies. The investigation of these reactions is therefore experimentally more complicated. A kinematically complete investigation of a four body final state requires the acquisition of triple coincidence data. Such data are difficult to obtain if the investigation of reactions producing small opening angles between some of the outgoing fragments is required. In his investigation of the breakup of ^9Be Macdonald [Ma88] has overcome this problem by using strip detectors (see section 3.6.1 for a description of these detectors). These detectors allowed coincidences between particles with an opening angle of $\sim 2°$. The reactions seen were predominantly elastic and resulted in $\alpha + \alpha + n$ final states. Two distinct sequential channels were identified, namely

$(^9Be, ^8Be_{g.s.} + n \rightarrow \alpha + \alpha + n)$
$(^9Be, ^5He + \alpha \rightarrow \alpha + \alpha + n)$

Bice et al. [Bi82] have investigated the breakup of ^{12}C at 132, 187 and 230MeV on ^{208}Pb. They were able to identify two coincident α particles in one telescope from the breakup of a ^8Be. In this way they were able to identify the reactions

$(^{12}C, ^{12}C^*_{7.7,9.6} \rightarrow ^8Be + \alpha \rightarrow \alpha + \alpha + \alpha)$
$(^{12}C, ^8Be_{g.s.,2.94} \rightarrow \alpha + \alpha)$

By comparing the observed cross sections for the production of two α particles in coincidence, deduced to have come from the breakup of ^8Be, with the incomplete fusion data of Siwek-Witczynska et al. [Si79] Bice et al. concluded that a direct breakup process $(^{12}C, ^8Be + \alpha)$ must account for the observed difference. They have also deduced that the $(^{12}C, \alpha + \alpha + \alpha)$ process becomes important at the higher energy of 230MeV. In order to positively identify this process however a triple coincidence measurement is required.

For heavier projectiles such as ^{14}N and ^{16}O most work has involved the detection of an α particle in coincidence with a heavy ion (HI). The breakup of ^{14}N

has been studied on a variety of targets e.g. 148MeV ^{14}N on ^{58}Ni [Bh81, Go84] 140MeV ^{14}N on ^{159}Tb [Dr81] and 208MeV ^{14}N on ^{93}Nb [Fu83]. Most of the coincidence yields have been shown to arise from sequential decays e.g.

$(^{14}N, ^{14}N^* \rightarrow ^{10}B + \alpha)$
$(^{14}N, ^{15}N^* \rightarrow ^{11}B + \alpha)$
$(^{14}N, ^{16}O^* \rightarrow ^{12}C + \alpha)$
$(^{14}N, ^{18}F^* \rightarrow ^{14}N + \alpha)$

Initial work by Bhowmik et al. [Bh81] suggested the presence of large yields for the direct breakup of ^{14}N on ^{58}Ni. Work by Goldhoorn et al. [Go84] however has shown that this conclusion resulted from an experimental angular resolution that was insufficient to allow the observation of the excited states in the primary fragment. The observation of HI + α coincidences for ^{16}O projectiles [Ra81] reveal similar breakup reactions.

This brief review of the breakup processes of light and light-heavy ions illustrates both the diversities of and the similarities between, these reactions. As one moves up in projectile mass the complexity of the final states and the difficulty of identification of the mechanisms increases. The types of breakup seen however, such as inelastic, sequential and direct breakup and incomplete fusion are common to projectiles over the whole range reviewed.

1.2.3 The Serber Model

The experiments of Helmholtz et al. in 1947 on deuteron breakup [He47] prompted the development of a model by Serber [Se47] to explain the observations. A beam velocity bump of neutrons was observed in inclusive neutron measurements. Serber suggested that the proton was stripped off the deuteron and the neutron continued on relatively undisturbed. This simple model implies that the momentum distribution of the neutron is not affected by the interaction and should be dependent upon its momentum in the deuteron i.e. its Fermi momentum. The double differential cross section should then be proportional to the

square of the internal wave function, ϕ, times a phase factor [Me85].

$$\frac{d^2\sigma}{dEd\Omega} \sim |\phi(p_i)|^2(E(E_{max} - E))^{1/2} \tag{1.1}$$

p_i internal momentum.

E, E_{max} energy of the detected particle and its kinematically allowed maximum.

The relation is remarkably successful, in view of its simplicity, at predicting the shape of the beam velocity bumps observed in light ion breakup. The model though is only applicable to inclusive measurements, it says nothing about the interaction between the participant fragment of the projectile and the target.

This model provides an intuitive picture of the interaction and suggests that treating the reaction in terms of a spectator and participant as a basis upon which to develop more sophisticated theories is not implausible.

1.2.4 Coulomb Excitation

The Coulomb interaction is well understood and a definitive description of it is given by Alder and Winther [Al]. A complete Coulomb calculation is non trivial, but this process lends itself readily to simplification. As long as the de Broglie wavelength of the projectile is small compared to a characteristic impact parameter treating the trajectory of the projectile in a classical way is a good approximation. The validity of this assumption for any particular reaction can be expressed in terms of the Sommerfeld parameter η.

$$\eta = \frac{b}{2\lambda\!\!\!^{-}} = \frac{e^2}{\hbar\sqrt{2}} \frac{Z_1 Z_2}{(E/m)^{\frac{1}{2}}} \tag{1.2}$$

b distance of closest approach.

$\lambda\!\!\!^{-}$ is the wavelength of the projectile divided by 2π.

E projectile energy.

m projectile mass.

The classical orbit is valid for values of $\eta \gtrsim 10$. The excitation ΔE resulting from the interaction must also be small i.e. $\Delta E/E \ll 1$ so that the classical orbit is not markedly modified. If the projectile breaks up, the centre of mass of the products is assumed to follow a classical orbit. Small excitation probabilities allow the use of first order quantum mechanical perturbation theory to calculate the transition probabilites. The term Semi-Classical is used to describe the type of calculation which embodies the above assumptions. The term derives from the fact that the orbital is treated classically, but the excitation is treated quantum mechanically.

A further simplification that can be made is to assume that only the lowest allowed order of electric multipole excitation is significant. The amplitudes for magnetic multipole excitation are much smaller than those for electric ones of the same multipole. Electric excitation amplitudes also decrease very rapidly with increasing multipolarity. It is therefore not unreasonable to assume the dominance of the lowest order electric multipole transition.

The differential cross section for a particular electric multipole transition may be written (see [Al]).

$$d\sigma_{E\lambda} = \left(\frac{Z_1 e}{\hbar v}\right)^2 a^{-2\lambda+2} B(E\lambda) df_{E\lambda}(\theta, \xi) \tag{1.3}$$

v is the projectile velocity
$B(E\lambda)$ is the reduced transition probability for transition of order $E\lambda$, $df_{E\lambda}(\theta, \xi)$ is the differential cross section function (see [Al]) (also called the Coulomb excitation function) where θ is the centre of mass scattering angle and $a = b/2$. The adiabaticity parameter ξ is given by equation 1.4. For large values of ξ the excitation probabilities vanish exponentially with ξ hence ξ must be small for observable processes. For one step processes $\xi \lesssim 1$.[1] The adiabaticity parameter is given by

$$\xi = \frac{a\Delta E}{v\hbar} \tag{1.4}$$

Shotter et al. [Sh81] have proposed that the breakup of certain projectiles at forward angles is due to a differential Coulomb force acting between the constituent clusters of these projectiles. This suggestion was prompted by the discov-

[1] A typical value of the adiabaticity parameter is .2

ery of direct breakup of ^7Li into an α and a t with low relative energies. The low relative energies imply a low ξ and hence make the Coulomb interaction probable. This direct breakup was observed for a variety of targets namely ^{96}Zr,^{120}Sn and ^{208}Pb. The reduced transition probabilities used were obtained from data on the inverse reaction [Ot76] i.e. $\alpha + t \longrightarrow {}^7Li + \gamma$ using the reciprocity relation [Bl]. Data over the entire required range however are not available. For the range of relative energy where data were not available the direct capture model was used in [Sh88a]. The E1 transition was assumed to be the only one of significance in these calculations. This model agreed with the differential cross section in reference [Sh84] for the furthest forward angle measured ($\theta_{lab} = 11.5$) but overpredicted the data at larger angles. In reference [Sh88a] reasonable agreement is achieved with the data at forward angles for the targets ^{96}Zr and ^{120}Sn, but there is disagreement with the data for the ^{208}Pb target. This discrepancy is attributed to a greater relative importance of the nuclear interaction.

1.2.5 Born Approximations

Breakup reactions can be treated in a completely quantum mechanical way using Born approximations. These approximations assume that the part of the potential deemed to cause the breakup is a perturbation and hence approximate wave functions can be used.

If the interaction Hamiltonian can be written

$$H = H_{o_a} + U_a + W_a = H'_a + W_a \quad (1.5)$$

$$= H_{o_b} + U_b + W_b = H'_b + W_b \quad (1.6)$$

where W is a perturbing potential and U is the part of the potential that causes elastic scattering. The transition matrix (T-matrix) element for the interaction going from channel a to b is then [Me]

and H_0 is the kinetic energy operator

$$T_{a\to b} = < \chi_b^{(-)}|U_a|\Phi_a > + < \Psi_b^{(-)}|W_a|\chi_a^{(+)} > \quad (1.7)$$

$$= \ <\Phi_b|U_b|\chi_a^{(+)}> + <\chi_b^{(-)}|W_b|\Psi_a^{(+)}> \tag{1.8}$$

where the + and − refer to boundary conditions in the initial and final states respectively and $H\Psi = E\Psi$, $H'\chi = E\chi$ and $H_o\Phi = E\Phi$. Φ is a plane wave and χ is known as a distorted wave. These two expressions are exact and equivalent, the choice of expression is governed by the type of reaction under consideration. The initial and final states are not connected by elastic scattering and hence the first terms in each of the above expressions are zero.

For a three body interaction of the type

$$a + A \longrightarrow b + x + A \tag{1.9}$$

where a is the projectile and A is the target and b and x are the outgoing fragments which formed the cluster constituents of a, the Hamiltonian can be written

$$H = T + V_{xb} + V_{xA} + V_{bA} \tag{1.10}$$

where T contains the kinetic energy operators for A, b and x and their internal Hamiltonians. In this section the internal wave functions are not explicitly written into the expressions. The potentials V_{mn} are the potentials between the particles m and n. By splitting up the potential in different ways different parts of it can be treated as the perturbation. The different divisions are applicable to different types of reaction.

The Hamiltonian is most often divided up in the following two ways e.g. see [Ba76]

$$H_i^{\text{PRIOR}} = \underbrace{T + V_{xb} + V_{aA}}_{H_i} + \underbrace{V_{xA} + V_{bA} - V_{aA}}_{V_i} \tag{1.11}$$

$$H_f^{\text{POST}} = \underbrace{T + V_{xA} + V_{bA}}_{H_f} + \underbrace{V_{xb}}_{V_f} \tag{1.12}$$

where H_i^{PRIOR} describes the initial channel and H_f^{POST} describes the final channel. The T-matrix element can now be written in two equivalent ways.

$$T^{\text{PRIOR}} = < \Psi_f^{(-)} | V_i | \chi_i^{(+)} > \quad (1.13)$$

$$T^{\text{POST}} = < \chi_f^{(-)} | V_f | \Psi_i^{(+)} > \quad (1.14)$$

where $\chi_{i,f}^{(\pm)}$ are the eigenfunctions of $H_{i,f}$ and $\Psi_{i,f}^{(\pm)}$ are the solutions of the full Hamiltonians with appropriate boundary conditions.

In the plane wave Born approximation (PWBA) both the distorted and exact wave functions are replaced by plane waves. This approximation assumes that the whole of the potential is perturbative. In most cases this is not a good assumption though Matsuoka et al. [Ma82] applied a POST plane wave approximation to $(^3He, pd)$ reactions at 90 MeV on ^{12}C, ^{51}V and ^{90}Zr with some success. They were able to fit the trends of the d differential cross section data, but not their magnitudes for a range of angles of p.

A better approximation is the so called distorted wave Born approximation (DWBA) where the exact wave functions $\Psi^{(\pm)}$ are replaced by their distorted counterparts $\chi^{(\pm)}$ giving

$$\begin{aligned} T_{\text{DWBA}}^{\text{PRIOR}} &= < \chi_f^{(-)} | V_{xA} + V_{bA} - V_{aA} | \chi_i^{(+)} > \\ T_{\text{DWBA}}^{\text{POST}} &= < \chi_f^{(-)} | V_{xb} | \chi_i^{(+)} > \end{aligned} \quad (1.15)$$

In the prior DWBA case the approximation is made in the final channel and the potential being ignored is V_{xb}. This is appropriate when the interaction between the fragments x and b in the final channel is small. In the post case the approximation is made in the initial channel and the potential ignored is $V_{xA} + V_{bA} - V_{aA}$. Inelastic processes result from the differential forces acting on the cluster constituents of the projectile hence the post approximation is most appropriate when these forces are weak.

The computation of the T-matrices in equation 1.15 requires the performance of sixfold integrals. This problem can be made more tractable if various approximations are made. In the model described by Baur and Trautmann [Ba76] a

zero range approximation is used to overcome this problem in the post DWBA formalism. The evaluation of $T_{\mathrm{DWBA}}^{\mathrm{POST}}$ rather than $T_{\mathrm{DWBA}}^{\mathrm{PRIOR}}$ is more practical because V_{xb} has a shorter range than $V_{xA} + V_{bA} - V_{aA}$, resulting in integrals which are quicker to evaluate because of the smaller range over which their computation is required. In the zero range approximation the product $V_{xb}\phi(r_{xb})$, where ϕ is the internal wavefunction of the projectile a, is replaced by a delta function. This reduces the T-matrix integral to a threefold one by removing the integration over the internal coordinates of the projectile. This approximation reduces the projectile to a point like particle with an infinitely broad momentum distribution. This patently unphysical situation can be partially rectified, when considering deuterons by the imposition of a lorentzian distribution. A better approximation is to use a Hulthèn type of potential and deuteron wave function to give

$$V_{xb}\phi \propto \frac{e^{-\beta r}}{r} \tag{1.16}$$

where r is a radial coordinate of the deuteron and β is a constant. The T-matrix integral is now six dimensional. This correction though is not adequate for heavier particles. In such cases the T-matrix integrand is multiplied by a finite range correction function, $\Lambda(r)$ [Ba84]. A term to take account of the non-locality of the potentials used is also included.

The post DWBA model described above has been applied by several people. At sub-Coulomb energies good agreement has been found with the data for the breakup of deuterons [Ba76, Pa78, Kl81]. Good agreement has also been found at higher energies e.g. [Sh83]. This model fails to work quite so well though for higher mass projectiles. Analysis of inclusive t, ^3He and α spectra from ^6Li induced breakup by Newmann et al. [Ne82] produced a reasonable reproduction of the shape of the inclusive spectra, but they failed to reproduce the angular distribution of the data. The authors suggest that this may be due to the use of the zero range approximation. The particles they are considering unlike the p and n in deuteron breakup, have internal structure and hence any constraint on the internal momentum is more significant. They also comment on the fact that

the optical model potentials that they used were derived from elastic scattering which presupposes that the breakup is properly treated in their derivation.

Shayam et al. [Sh80] have analysed the inclusive and coincidence data from the ^3He induced reactions of Matsoka et al. [Ma78, Ma80]. The calculations have some success, but the most notable aspect is that where both DWBA and PWBA calculations are available the DWBA does not do significantly better at reproducing the shape of the data though the DWBA is required to give the correct magnitude. Thompson and Nagarajan [Th83] have performed a prior DWBA calculation for the breakup of ^7Li on ^{208}Pb. A cluster model was used for the internal wave function of ^7Li. Both the nuclear and Coulomb plus nuclear calculations overestimate the data by factors of 20-40 indicating that ^7Li partially recovers from the actions of the forces tending to break it up. The authors concluded that a more realistic model with coupling between the elastic and breakup channels was required.

The DWBA is a powerful tool, but its usefulness is limited by the approximations that must be made in order to make the calculations practical.

1.2.6 The Adiabatic Approximation

The adiabatic approximation is a method of evaluating the wave functions for three body processes without performing a full three body calculation. In this approximation the energies of low lying states are assumed to be degenerate and the wave function, $\psi(\underline{R},\underline{r})$ where $\underline{R}$ is the position vector of the projectile relative to the target and $\underline{r}$ is the separation of the centres of mass of the cluster constituents of the projectile, is assumed to statisfy

$$(E - \varepsilon_a - T_R - V(\underline{R},\underline{r}))\psi(\underline{R},\underline{r}) = 0 \qquad (1.17)$$

The binding energy of the projectile, ε_a replaces the Hamiltonian for the relative motion of the components of the projectile. E is the system's energy, T_R is a kinetic energy operator for the relative motion of the projectile and the target and $V(\underline{R},\underline{r})$

is the sum of the target cluster optical potentials at appropriate fractions of the projectile incident kinetic energy. Expanding the total wave function in terms of partial waves results in a set of coupled equations which can be solved to give the set of r dependent T-matrix elements, $T^J_{l'L',lL}(r)$ where l is the projectile orbital angular momentum, L is the relative angular momentum of the target and the projectile and J is the total system angular momentum, which describe the reaction. This approximation effectively means that the nuclear motion between the constituent clusters of the projectile is "frozen" in a particular state during the collision and is most applicable where the energies of the excited states of the projectile are negligible compared to E i.e. for high projectile energies.

This model was first proposed by Johnson and Soper [Jo70] as a method for accounting for breakup in deuteron stripping and elastic scattering reactions. It was developed by Amakawa et al. [Am79a, Am79b, Am81] to include the breakup effect of higher angular momentum states of the p-n relative motion than Johnson and Soper used. The success of this method for deuterons prompted other authors to apply it to the breakup of heavier projectiles. After finding that a prior DWBA model failed to predict the differential cross sections for the direct breakup of 70MeV ^7Li on ^{208}Pb [Th83] (see section 1.2.5), Thompson and Nagarajan tried a modified adiabatic approximation which included excited states of the projectile. They found that when both Coulomb and nuclear breakup were allowed the calculation overpredicted the data by a factor of three, but a pure nuclear calculation reproduced the data well. The failure of the calculation when a Coulomb interaction was included is possibly due to the fact that the adiabatic approximation is not good for such long range forces because the interaction time is long and hence the "freezing" of the nucleus is not a good assumption.

The failure of the double folding model to describe the elastic scattering of ^6Li at 156MeV [Sa78] prompted Thompson and Nagarajan [Th81] to apply the adiabatic model to this scattering for various targets (^{12}C, ^{40}Ca and ^{208}Pb). In the double folding model the real part of the potential is determined by folding an effective nucleon-nucleon potential, v, into the nucleon densities, ρ, of the colliding

nuclei in their ground states i.e. $V_r = \int \rho(r')\rho(r'')v(r - r' + r'')dr'dr''$. A Woods-Saxon type of potential is assumed for the imaginary part of the potential. This model is deemed to be successful if the renormalization factor, N_R for the real part of the potential, determined by fitting to elastic scattering data, is close to one. In the ^6Li case mentioned above the N_R required is approximately 0.5.

In all cases the fits to angular distributions were found to be very good suggesting that the discrepancy with the folding model was due to the breakup of ^6Li. A similar calculation has been performed [Na82] for the elastic scattering of ^7Li on ^{40}Ca and ^{48}Ca. Coupling between the ground state and the first excited $\frac{1}{2}^-$ state was included. The agreement between the data and the theory is not particularly good and the authors suggest that additional breakup affects need to be included.

1.2.7 Coupled Discretized Continuum Channels (CDCC)

As already mentioned in the previous section the double folding model for scattering though meeting with substantial success in many cases fails dramatically for the loosely bound cluster like nuclei ^6Li, ^7Li and ^9Be [Sa79a, Gl80, Sa79b]. The success of the adiabatic model in attributing this discrepancy to the breakup channels available to these projectiles due to their low breakup thresholds prompted the authors of [Sa83, Ya81, Ya82] to develop a more sophisticated model that used a double folding potential, but allowed breakup via excited states of the projectile and into the continuum. Their method is dubbed the coupled discretized continuum channels or CDCC method for reasons which will become apparent below. A detailed description of the method is given in [Sa86]. References to all the data refered to below can also be found in [Sa86].

The total wave function is expanded as

$$\Psi = \sum_{ij} \psi_i \phi_j \chi_{ij}(\underline{R}) \tag{1.18}$$

where ψ_i describes the internal states of the projectile, ϕ_j the internal states of the target and $\chi_{ij}(\underline{R})$ the relative motion of the projectile and target. The χ_{ij} are

the solutions of a set of coupled channel equations produced when equation 1.18 is used in the Schrödinger equation. The inclusion of continuum breakup states results in an infinite number of coupled equations. This problem is overcome by the discretization of the projectile internal wave function. A cluster model wave function is used and cut off maxima are imposed on the relative angular l and linear k momenta. The k continuum for each l is divided into bins and the wave function is averaged over each bin. A doubly folded potential is used which is determined by folding the effective nucleon-nucleon interaction over the nucleon densities of the target and projectile. The real and imaginary parts of the potential have the same form, but are allowed to have different absolute magnitudes.

$$V = N_R U_{DF} + iN_I U_{DF} \tag{1.19}$$

The Ns are normalization constants and U_{DF} is a doubly folded potential. If this potential is valid then N_R should be equal to 1. The discrepancy for elastic scattering of ^6Li ^7Li and ^9Be mentioned earlier meant that good fits could not be obtained to the data unless N_R was reduced by a factor of about 2. In the calculations of [Sa86] N_R, was fixed at 1 so that the only adjustable parameter in the theory was N_I. This was determined by fitting to elastic scattering data and the value determined was then used for the breakup calculations.

The calculations for the elastic scattering of ^7Li from a variety of targets (^{12}C,^{48}Ca,^{58}Ni and ^{208}Pb) were found to agree well with the data. The method was also applied to the direct and sequential breakup of ^7Li, on ^{120}Sn and ^{12}C targets, into an α and a t. When the potential used was only nuclear good fits were obtained to both the sequential and direct data for ^{120}Sn. A sequential breakup calculation was also performed using a nuclear + Coulomb potential. Direct breakup (termed non resonant in [Sa86]) channels however were not included in the coupling scheme, to save on computing time. Though the form of the angular distribution was improved upon the absolute magnitude was overpredicted by a factor of ~ 3 for a ^{120}Sn and ~ 4 for a ^{208}Pb target. The exclusion of the non resonant channels was thought to be the reason for the discrepancy. A good fit

was also obtained, using a nuclear interaction, to the sequential breakup on ^{12}C, but a substantial direct breakup differential cross section was predicted. No direct breakup is observed and the authors do not suggest any explanation for this large discrepancy.

Calculations performed for the elastic scattering and breakup of ^{6}Li also provide good fits to the data.

1.3 Aims and Outline

The main aim of this thesis is to employ polarization as a tool to further the investigation of the mechanism involved in the dissociation of ^{7}Li into its cluster constituents. The brief review in this chapter of the various calculations available for breakup illustrates both their successes and limitations. The DWBA, adiabatic and CDCC calculations have all met with varying degrees of success when considering only nuclear interactions, but have all failed to satisfactorily include a Coulomb one. The Coulomb calculation of Shotter et al. [Sh84] has demonstrated that at forward angles the Coulomb interaction appears to be of primary importance. As already mentioned the measurement of analysing powers provides a more sensitive probe of the mechanism causing breakup than the measurement of differential cross sections will allow. The object of this work is therefore to exploit the advantages of analysing powers in an attempt at a more rigorous examination of the breakup mechanism of ^{7}Li.

In the next chapter after a brief explanation of polarization and analysing powers, a description of a simple semi-classical calculation for analysing powers is given followed by a discussion of their advantages. Chapter 3 gives a description of the experimental system used. A description of the Monte Carlo code used to simulate the breakup reactions is given in chapter 4. The method of analysis and the data are presented in chapter 5 and the conclusions are presented in chapter 6.

Chapter 2

Theory

2.1 Introduction

In any experiment the smaller the number of variables that are averaged over the more sensitively can the experimental results and the theory be compared. For example more can be learnt about a particular reaction if the differential cross section is determined at several angles than if the total cross section is the only datum available. Similarly the use of a polarized beam is better than the use of an unpolarized one, because a magnetic substate dependence can be determined.

2.2 Coordinate Systems

In polarization work it is important to carefully define which coordinate system is being refered to because the values of polarization dependent quantities are coordinate system dependent.

The coordinate system usually refered to is known as the Helicity frame [Ma]. It is the frame in which the z axis lies in the beam direction and the y axis lies in the direction $\underline{k}_{in} \wedge \underline{k}_{out}$ for the reaction in question. Another frame sometimes used has its y axis in the beam direction and its z axis in the direction $\underline{k}_{in} \wedge \underline{k}_{out}$. This frame is known as the transverse frame (see figure 2.1)

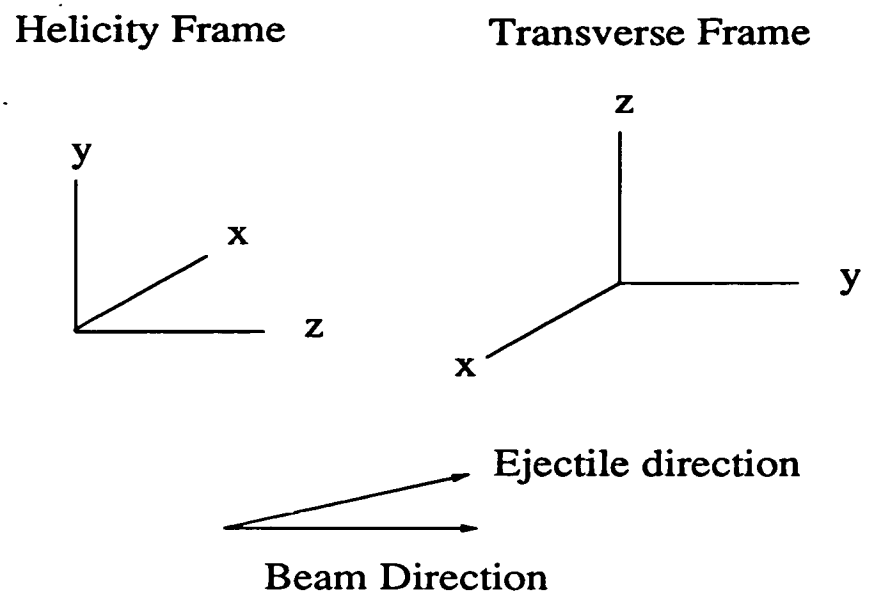

Figure 2.1: *Coordinate systems*

2.3 Polarization

A polarized beam is one in which the populations of the magnetic substates are not all equal. This though does not mean that the beam will have a prefered spin direction. Consider the diagram in figure 2.2. If the populations of the m=3/2,−3/2 states are equal and the populations of the m=1/2,−1/2 states are equal, but different to those of the m=±3/2 states the beam will be polarized, but it will not have a prefered spin direction. This type of polarization is known as tensor polarization. If the populations of the + and − states are not equal then the beam is polarized and has a prefered spin direction. This beam has vector as well as tensor components.

A beam with four magnetic substates, such as a ^7Li beam may be represented by a four component spin wave function.

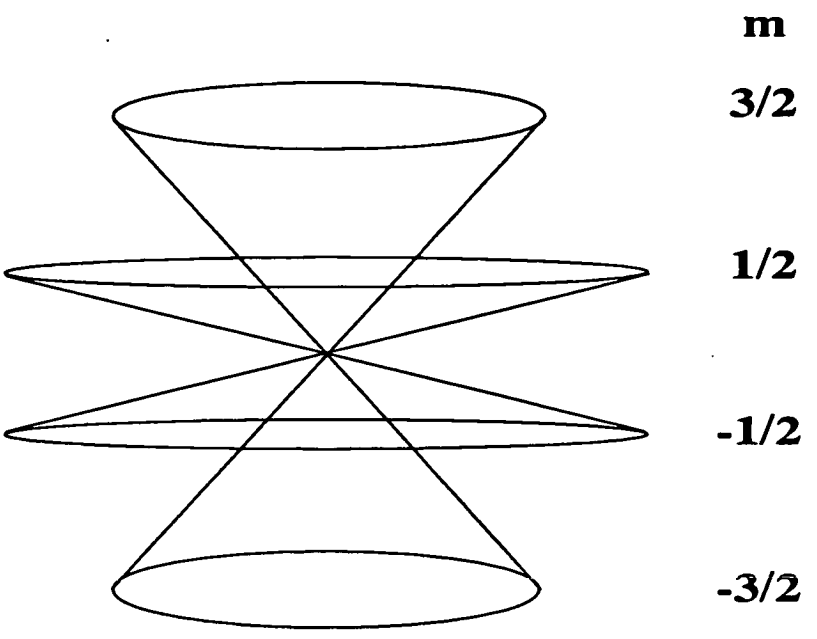

Figure 2.2: *Schematic diagram of the magnetic substates of* ^7Li.

$$\chi = \begin{pmatrix} a_1 \\ a_2 \\ a_3 \\ a_4 \end{pmatrix} \tag{2.1}$$

A convenient way of describing a polarized beam is using a density matrix ρ.

$$\rho = \chi\chi^\dagger = \begin{pmatrix} |a_1|^2 & a_1a_2^* & a_1a_3^* & a_1a_4^* \\ a_2a_1^* & |a_2|^2 & a_2a_3^* & a_2a_4^* \\ a_3a_1^* & a_3a_2^* & |a_3|^2 & a_3a_4^* \\ a_4a_1^* & a_4a_2^* & a_4a_3^* & |a_4|^2 \end{pmatrix} \tag{2.2}$$

This represents a pure polarized beam and contains 7 independent quantities, the 4 moduli $|a_n|$ + the 3 relative phases of a_2, a_3 and a_4 to a_1. In general a partially polarized beam would have 16 independent elements in its ρ and cannot be represented by a wave function.

A set of operators, analogues to Pauli spin operators, can be defined. The set of spherical tensor operators have elements given by (using the notation of [Si])

$$\{\tau_{KQ}\}_{\alpha'\alpha} = (-1)^{s-\alpha}(2s+1)^{\frac{1}{2}}\langle s\alpha' s - \alpha | KQ\rangle \tag{2.3}$$

$\langle s\alpha' s - \alpha | KQ\rangle$ is a Clebsch-Gordon coefficient.

s is the spin of the particle.

K is an integer in the range 0 to $2s$.

Q is an integer in the range $-K$ to $+K$.

The expectation values of these operators are then given by

$$t_{KQ} \equiv \langle \tau_{KQ}\rangle = \frac{Tr(\rho\tau_{KQ})}{Tr(\rho)} \tag{2.4}$$

This expectation value is what is used to describe the polarization of a beam. The t_{KQ} are also known as spin moments [Da].

The irreducible statistical tensors t_{KQ} are used because they have the desirable property of undergoing simple rotations ($t_{00} = 1$ by definition). The polarization of a beam can also be described in terms of a set of Cartesian tensors. This set is most commonly used when considering spin 1/2 systems.

- Given any non zero set of tensors t_{KQ} of a given rank K any tensor $t_{KQ'}$ can be generated by a rotation.
- Tensors of different ranks K are not mixed by rotations. If all t_{KQ}, where $K \neq 0$, are initially zero then they cannot be made non zero by rotations.

The rotations can be expressed in terms of the $D^{(K)}_{QQ'}$ rotation matrices elements [Br].

$$(t_{KQ'})_{c'} = \sum_{Q} D^{(K)}_{QQ'}(\alpha,\beta,\gamma)(t_{KQ})_c \tag{2.5}$$

where

$$D^{(K)}_{QQ'} = e^{-i\alpha Q} d^{(K)}_{QQ'}(\beta) e^{-i\gamma Q'} \tag{2.6}$$

The c and c' subscripts refer to different frames and α, β, γ are the relevant Euler angles (as defined by Brink and Satchler [Br]).

In order to visualize beam polarizations a classical analogy between them and the multipole moments that describe charge distributions may be made. Closed surfaces can be used to represent charge distributions for particular multipole moments. In a similar way (see [Da]) such surfaces can be used to represent polarizations or spin moments where the distance from the origin to the surface, $R(\theta, \phi)$, represents the number of particles having spins pointing in the direction θ, ϕ.

$$R(\theta, \phi) = R_0(1 + \sum_Q t_{KQ} Y^*_{KQ}(\theta, \phi)) \qquad K \geq 2 \qquad (2.7)$$

Within this picture an unpolarized beam would be represented by a sphere of radius R_0, rank 1 or vector polarization by a dipole and rank 2 or tensor polarization by an elipsoid. More complex surfaces are required for higher order polarizations. Examples of these surfaces are shown in figure 2.3.

The polarized ^7Li beam that was used in the experiment that forms the subject of this thesis was produced by the polarized source at the NSF at the Daresbury Laboratory (see section 3.2 for a description of the source and section 5.1 for a description of the determination of the beam polarization). This source has a natural z axis defined by the magnetic field (see section 3.2). In this coordinate system the polarization produced by the source is

$$t_{10} = \frac{1}{2\sqrt{5}} \qquad t_{20} = \pm\frac{1}{2} \qquad t_{30} = \frac{1}{\sqrt{5}} \qquad (2.8)$$

t_{20} has opposite signs in phases A and B. This z axis in the source is known as the polarization symmetry axis. For the experiment described in this thesis the polarization symmetry axis was rotated so that on arrival at the reaction chamber it lay in the y direction in the Helicity frame. In order to describe the polarization of the beam in the helicity frame therefore the above quantities must be rotated through the Euler angles $\alpha = 90°$, $\beta = 90°$, $\gamma = 90°$. The set of t_{KQ} that describe the polarization of the beam on target contains some zero elements namely t_{10}, $t_{2\pm1}$, t_{30} and $t_{3\pm2}$. The polarization of the beam on target is described by

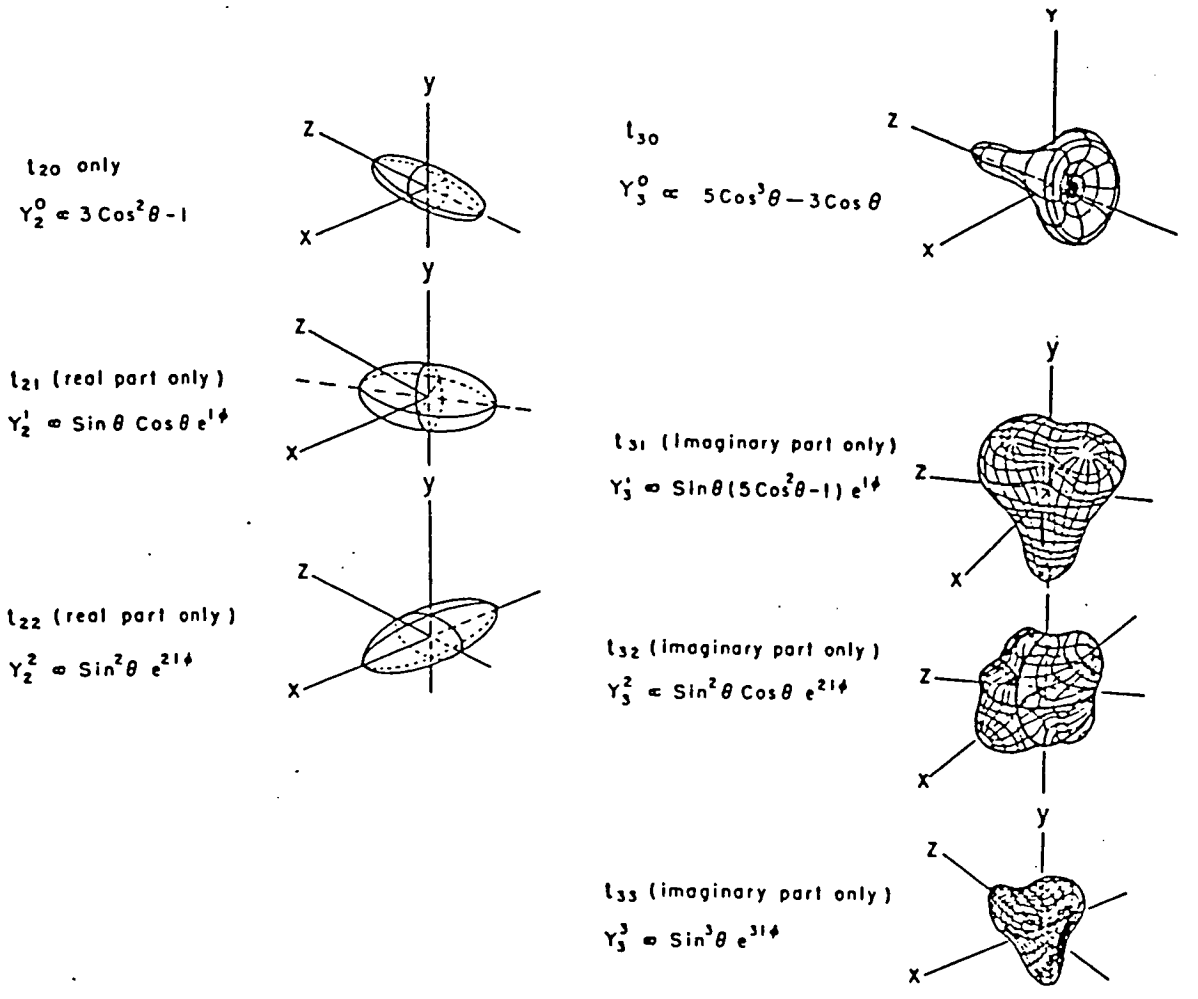

Figure 2.3: *Surfaces representing rank 2 and 3 polarizations.*

$$t'_{11} = t'_{1-1} = -id^{(1)}_{01}(\tfrac{\pi}{2})t_{10} = -\tfrac{i}{2\sqrt{10}}$$

$$t'_{20} = d^{(2)}_{00}(\tfrac{\pi}{2})t_{20} = \mp\tfrac{1}{4} \qquad t'_{22} = t'_{2-2} = -d^{(2)}_{02}(\tfrac{\pi}{2})t_{20} = \mp\tfrac{1}{4}\sqrt{\tfrac{3}{2}} \qquad (2.9)$$

$$t'_{31} = t'_{3-1} = -id^{(3)}_{01}(\tfrac{\pi}{2})t_{30} = i\tfrac{\sqrt{3}}{4\sqrt{5}} \qquad t'_{33} = t'_{3-3} = id^{(3)}_{03}(\tfrac{\pi}{2})t_{30} = \tfrac{i}{4}$$

2.4 Analysing Powers

The response of any system to a polarized beam will depend on the particular polarization present and is expressed in terms of analysing powers which are characteristic of the particular nuclear reaction taking place. This response is manifest as the counting rate measured, W, which depends linearly on the density matrix elements and thus also linearly on the tensor components t_{KQ}. This linear dependence is a result of the relation $\langle A \rangle = Tr(\rho A)/Tr(\rho)$ where A is any Hermitian operator. W can therefore be written

$$W = N \sum_{KQ} t_{KQ} T^*_{KQ} \tag{2.10}$$

This relation defines the analysing power T_{KQ}. N is a normalization constant and is chosen such that $T_{00} = 1$. As W must be real the T_{KQ} must possess the same rotational properties as the t_{KQ}. This relation can then be written in terms of measured yields Y as

$$Y = Y_0(1 + \sum_{K>0,Q} t_{KQ} T^*_{KQ}) \tag{2.11}$$

Y is the yield while the beam is polarized and Y_0 is the yield while the beam is unpolarized.

The detection system used in the experiment that forms the subject of this thesis consisted of two pairs of detector telescopes, one on either side of the beam (z direction) at polar angles (θ, ϕ) and $(\theta, \phi + \pi)$ (see section 3.5 and figures 3.7 and 3.8). The solid angles subtended by each pair of telescopes were the same. This setup was chosen so that the symmetry of the system would allow the measurement of the desired analysing power. A simple relation exists between the analysing powers for the 2 sets of detectors because of the rotational properties of the T_{KQ} which are the same as the rotational properties of t_{KQ}.

$$T_{KQ}(\theta, \phi + \pi) = e^{-i\pi Q} T_{KQ}(\theta, \phi) \tag{2.12}$$

From this simple relation it can be seen that the rotated and unrotated T_{KQ} are equal for even values of Q and $T_{KQ}(\theta, \phi + \pi) = -T_{KQ}(\theta, \phi)$ for odd values of Q. The detection system used possesses reflection symmetry about the horizontal plane (see figures 3.7 and 3.8) therefore the analysing powers obey the relation (see [Si])

$$T_{KQ} = (-1)^{K-Q} T_{K-Q} \tag{2.13}$$

so long as the reaction under consideration is parity conserving. This relation follows from the fact that a reflection in a plane is the same as a parity operation followed by a rotation of π around an axis perpendicular to the plane.

The above relations for T_{KQ} and that fact that some t_{KQ} are zero considerably simplifies the expression for the sum of the data from both pairs of telescopes in any one phase. This sum is then

$$Y_X = (Y_{left} + Y_{right})_X = 2Y_0(1 + t'_{20}T_{20} + 2t'_{22}T_{22}) \tag{2.14}$$

where Y_X is the sum of all the data in a phase X. t'_{20} and t'_{22} are given in equation 2.9 and are both related to t_{20} the polarization in the frame where the z axis is the polarization symmetry axis, hence this equation can be written

$$Y_X = 2Y_0(1 + t_{20}{}^T T_{20}) \tag{2.15}$$

where ${}^T T_{20} = -\frac{1}{2}(T_{20} + \sqrt{6}T_{22})$ and is known as transverse T_{20} because it is the value of T_{20} in the transverse frame.

For the main data collection run the beam was run in two polarized phases. If the yields in the different phases and the beam polarization are known the analysing power ${}^T T_{20}$ can be calculated.

$${}^T T_{20} = \left(\frac{Y_B - Y_A}{Y_B + Y_A}\right) \frac{1}{|t_{20}|} \tag{2.16}$$

where Y_A and Y_B are the total yields in phases A and B.

2.5 Calculation for Analysing Powers

A simple expression for analysing powers can be obtained using the DWBA to obtain expressions for the scattering amplitudes. In general in order to evaluate the expression for T_{KQ} a Rutherford orbit is assumed and the orbital integrals are evaluated using Coulomb excitation functions [Al].

In order to calculate the analysing powers a relation between them and scattering amplitudes is required. This is derived by expressing the density matrix in terms of scattering amplitudes.

$$\rho_{\alpha\alpha'}(\theta; b(\vec{a},c)d) = \frac{\sum_{\beta\gamma\delta} F^{\alpha\beta}_{\gamma\delta} F^{*\alpha'\beta}_{\gamma\delta}}{\sum_{\beta\gamma\delta} |F^{\alpha\beta}_{\gamma\delta}|^2} \tag{2.17}$$

$F^{\alpha\beta}_{\gamma\delta}$ is the scattering amplitude and a, b, c, d are the spins and $\alpha, \beta, \gamma, \delta$ are spin substates of the projectile, target, ejectile and residual nucleus respectively. The analysing power is then [Si]

$$\begin{aligned} T_{KQ} &= \sum_{\alpha\alpha'} (\tau_{KQ})^*_{\alpha'\alpha} \rho^*_{\alpha\alpha'} \\ &= \frac{\sum_{\substack{\alpha\alpha' \\ \beta\gamma\delta}} \hat{s}_a \hat{K} (-1)^{s_a-\alpha-Q} \begin{pmatrix} s_a & s_a & K \\ \alpha' & -\alpha & -Q \end{pmatrix} F^{*\alpha\beta}_{\gamma\delta} F^{\alpha'\beta}_{\gamma\delta}}{\sum_{\substack{\alpha\beta \\ \gamma\delta}} |F^{\alpha\beta}_{\gamma\delta}|^2} \end{aligned} \tag{2.18}$$

where s_a is the projectile spin and $\alpha' = \alpha + Q$. The notation $\hat{s}_a = \sqrt{(2s_a + 1)}$ is used.

A general expression for the scattering amplitudes can be derived using the DWBA. In the reaction considered here the target's ground state is a spin zero one and it remains in its ground state therefore $\beta = \delta = 0$. The scattering amplitude can be written

$$F^{\alpha}_{\gamma} = \langle \chi^{(-)}_f(\underline{R}) \phi_{s_c\gamma}(\underline{r}) | V | \chi^{(+)}_i(\underline{R}) \phi_{s_a\alpha}(\underline{r}) \rangle \tag{2.19}$$

The ϕs are the internal wavefunctions and the χs are distorted wavefunctions. r and R are the internal radial coordinates and the relative projectile target coordi-

nates respectively (s_c is the ejectile spin). Any potential which depends only on $\underline{r}$ and $\underline{R}$ and is invariant under rotations can be written as a linear combination of spherical harmonics and hence the potential V can be written

$$V = \sum_{\lambda\mu} V_{\lambda\mu}(R,r) Y^*_{\lambda\mu}(\hat{\underline{R}}) Y_{\lambda\mu}(\hat{\underline{r}}) \tag{2.20}$$

where $\hat{\underline{R}}$, $\hat{\underline{r}}$ are the polar angles for the appropriate vectors. Substituting this equation into equation 2.19 one gets

$$F^{\alpha}_{\gamma} = \sum_{\lambda\mu} \langle \chi^{(-)}_f(\underline{R}) \phi_{s_c\gamma}(\underline{r}) | V_{\lambda\mu}(R,r) Y^*_{\lambda\mu}(\hat{\underline{R}}) Y_{\lambda\mu}(\hat{\underline{r}}) | \chi^{(+)}_i(\underline{R}) \phi_{s_a\alpha}(\underline{r}) \rangle \tag{2.21}$$

Considering r dependent quantities only and using the Wigner-Eckart Theorem [Me] the magnetic substate dependence can be contained within a Clebsch-Gordan coefficient.

$$\int d\underline{r} \phi^*_{s_c\gamma}(\underline{r}) V_{\lambda\mu}(R,r) Y_{\lambda\mu}(\hat{\underline{r}}) \phi_{s_a\alpha}(\underline{r}) = \frac{1}{\sqrt{(2s_c+1)}} \langle s_a \alpha \lambda\mu | s_c\gamma \rangle \langle \phi_{s_c} \| V_\lambda \| \phi_{s_a} \rangle_R \tag{2.22}$$

Substituting this into equation 2.21 and using 3-j Wigner symbols instead of Clebsch-Gordon coefficients one obtains

$$\begin{aligned} F^{\alpha}_{\gamma} &= \sum_{\lambda\mu} (-1)^{s_a+\alpha-\lambda+\mu} \begin{pmatrix} s_a & \lambda & s_c \\ \alpha & \mu & -\gamma \end{pmatrix} \int d\underline{R} \langle \phi_{s_c} \| V_\lambda \| \phi_{s_a} \rangle_R \chi^{*(-)}_f(\underline{R}) Y^*_{\lambda\mu}(\hat{\underline{R}}) \chi^{(+)}_i(\underline{R}) \\ &= \sum_{\lambda\mu} (-1)^{s_a+\alpha} \begin{pmatrix} s_a & \lambda & s_c \\ \alpha & \mu & -\gamma \end{pmatrix} B_{\lambda\mu} \end{aligned} \tag{2.23}$$

The functions $B_{\lambda\mu}$ transform like tensors of rank λ and obey various rules as a consequence of parity and angular momentum conservation. Different coordinate systems and dynamics will produce different values of $B_{\lambda\mu}$. In the Helicity frame

$${}^{H}B_{\lambda\mu} = \pi_i \pi_f (-1)^{\lambda+\mu} \, {}^{H}B_{\lambda-\mu} \tag{2.24}$$

where π_i and π_f are the parities of the initial and final states respectively. In the transverse frame

$$^{T}B_{\lambda\mu} = (-1)^{\mu}\pi_i\pi_f \ {}^{T}B_{\lambda\mu} \tag{2.25}$$

This equation results in certain $B_{\lambda\mu}$ being zero (e.g. $B_{10} = 0$ for the transition $\frac{3}{2}^- \rightarrow \frac{1}{2}^+$).

Equation 2.23 is general and does not assume dominance of either nuclear or Coulomb forces. Assumptions about the interaction are introduced via the method of determination of $B_{\lambda\mu}$. Substituting equation 2.23 into equation 2.18 and using $\alpha + \mu - \gamma = 0$ gives

$$T_{KQ} = \sum_{\substack{\alpha\alpha' \\ \lambda\lambda'\mu}} (-1)^{s_a-\alpha-Q} \hat{s}_a \hat{K} \begin{pmatrix} s_a & \lambda & s_c \\ \alpha & \mu & -(\alpha+\mu) \end{pmatrix} \begin{pmatrix} s_a & \lambda' & s_c \\ \alpha' & \mu-Q & -(\alpha+\mu) \end{pmatrix} \begin{pmatrix} s_a & s_a & K \\ \alpha' & -\alpha & -Q \end{pmatrix} B^*_{\lambda\mu} B_{\lambda'\mu'} \Big/ \sum_{\lambda\mu} |B_{\lambda\mu}|^2 \frac{1}{\hat{\lambda}^2} \tag{2.26}$$

where $\mu' = \mu - Q$. The reduction of the sum of the 3-j Wigner symbols over α to $1/\hat{\lambda}^2$ in the denominator comes from their property of orthonormality [Br].

Direct breakup for the reaction $^{120}Sn(^7Li, \alpha + t)$ is modelled by assuming that the final state is a spin 1/2 one and that the only multipole involved in the breakup up is $\lambda = 1$ ($s_a^\pi = \frac{3}{2}^-$, $s_c^\pi = \frac{1}{2}^+$). The analysing power determined in the experiment considered in this thesis was $^{T}T_{20}$. Evaluating equation 2.26 for T_{20} gives

$$T_{20} = \frac{\frac{1}{2}(|B_{11}|^2 + |B_{1-1}|^2 - 2|B_{10}|^2)}{|B_{11}|^2 + |B_{1-1}|^2 + |B_{10}|^2} \tag{2.27}$$

This equation is not frame dependent. The value of the analysing power in a particular frame is determined by evaluating the $B_{\lambda\mu}$ in that particular frame. In the transverse frame $B_{10} = 0$ (see equation 2.25) hence

$$^{T}T_{20} = \frac{1}{2} \tag{2.28}$$

see [Jo88] for a discussion of the value at 0°.

This result is independent of angle and the only assumption is that $\lambda = 1$. In general equation 2.27 does not require a DWBA assumption. Given a set of scattering amplitudes F_γ^α deduced from any theory a set of $B_{\lambda\mu}$ can always be found using

$$B_{\lambda\mu} = \hat{\lambda}^2 \sum_{\alpha\gamma} (-1)^{s_a+\alpha} \begin{pmatrix} s_a & \lambda & s_c \\ \alpha & \mu & -\gamma \end{pmatrix} F_\gamma^\alpha \tag{2.29}$$

The $B_{\lambda\mu}$ calculated using this formula will always give the F_γ^α back when substituted into equation 2.23. The assumption that $\lambda = 1$ is not a direct Coulomb assumption, but any nuclear interaction would not necessarily favour $\lambda = 1$ as a Coulomb interaction would[4]. Therefore any coincidence between the data and the result of this calculation may be taken to indicate a Coulomb interaction.

This calculation can also be applied to the sequential breakup of ^7Li via its $\frac{7}{2}^+$ excited state. The relevant transition is then $\frac{3}{2}^+ \rightarrow \frac{7}{2}^+$. This transition does not result in an equation where the $B_{\lambda\mu}$ simply cancel. If a specific Coulomb assumption is made for this transition and the potential in equation 2.20 is replaced by a Coulomb one then the scattering amplitude can be written [Al]

$$F_\gamma^\alpha = -i \sum_{\lambda\mu} (-1)^{s_a-\alpha} \hat{s}_a \hat{\lambda} \begin{pmatrix} s_a & \lambda & s_c \\ -\alpha & \mu & \gamma \end{pmatrix} X^\lambda_{s_a \rightarrow s_c} R_{\lambda\mu}(\theta, \xi) \tag{2.30}$$

$R_{\lambda\mu}$ is an orbital integral, θ the centre of mass scattering angle, ξ the adiabaticity parameter (see equation 1.4) and $X^\lambda_{s_a \rightarrow s_c}$ is a strength parameter which does not depend on μ.

$$X^\lambda_{s_a \rightarrow s_c} \propto \langle \phi_{s_c} \| M(E\lambda) \| \phi_{s_a} \rangle \tag{2.31}$$

where $M(E\lambda)$ is an electric multipole moment. In Coulomb interactions the lowest possible multipole transition is in general dominant and is the only one that will be considered here. For the sequential reaction being considered the relevant electric multipole is E2. When equation 2.30 is put into equation 2.18 because only one λ is being considered the strength parameter, which contains all the

[4]The DWBA calculation of Bertualani et al. [Be91] is an illustration of the way in which the amplitudes for the nuclear and Coulomb transitions fall off more rapidly for the Coulomb than the nuclear interaction with increasing λ.

nuclear information, cancels out. This expression for the analysing power therefore depends only on the initial and final spins the multipole moment of the transition and the orbital integrals. A code written by El-Lithi [El] was used to evaluate the orbital integrals $R_{\lambda\mu}$. The calculated values of ${}^{T}T_{20}$ for the transition $\frac{3}{2}^{+} \rightarrow \frac{7}{2}^{+}$ and at a beam energy of 70MeV are shown in figure 2.4.

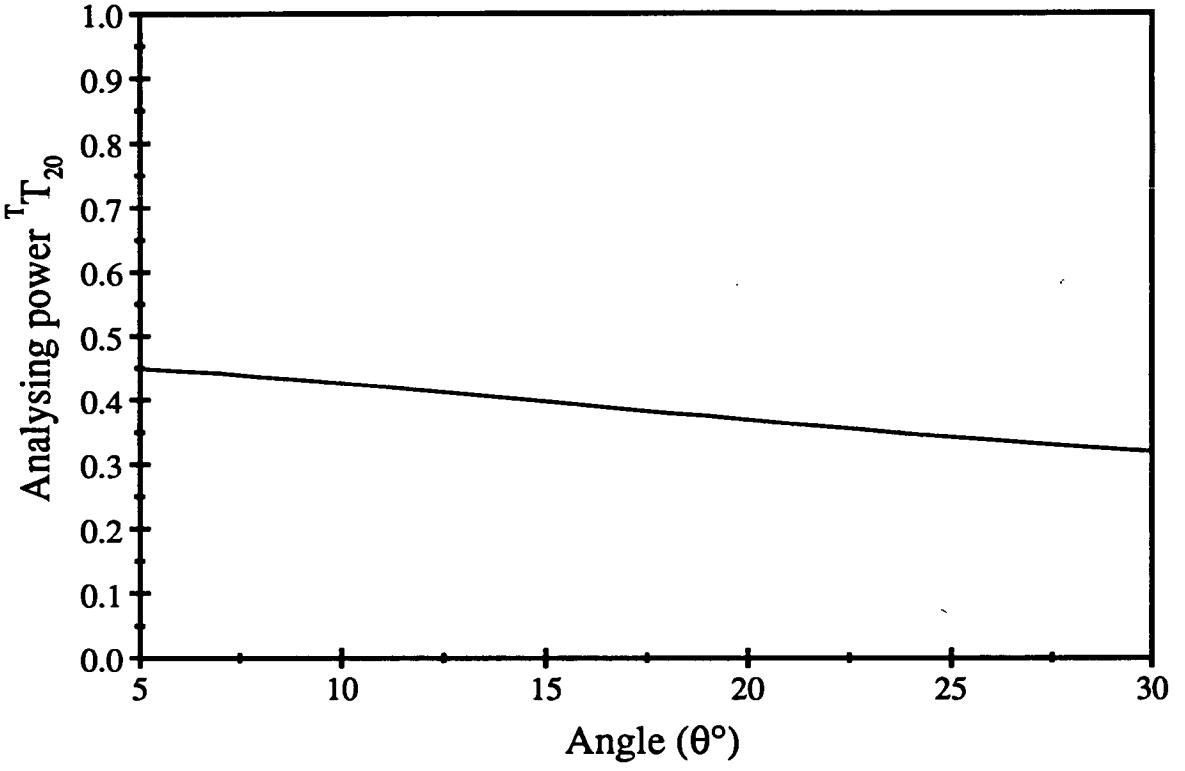

Figure 2.4: *Coulomb calculation for sequential* ${}^{T}T_{20}$

2.6 Advantages and Disadvantages of Analysing Powers

Analysing powers have certain advantages over cross sections. The most important advantage is their greater overall sensitivity. Expressions for analysing powers and cross sections are shown in equations 2.32 and 2.33.

$$T_{KQ} = \frac{\sum_{\substack{\alpha\alpha' \\ \beta\gamma\delta}} \hat{s_a}\hat{K}(-1)^{s_a-\alpha-Q} \begin{pmatrix} s_a & s_a & K \\ \alpha' & -\alpha & -Q \end{pmatrix} F^{*\alpha\beta}_{\gamma\delta} F^{\alpha'\beta}_{\gamma\delta}}{\sum_{\substack{\alpha\beta \\ \gamma\delta}} |F^{\alpha\beta}_{\gamma\delta}|^2} \tag{2.32}$$

$$\frac{d\sigma}{d\Omega} \propto \sum_{\substack{\alpha\beta \\ \gamma\delta}} |F^{\alpha\beta}_{\gamma\delta}|^2 \tag{2.33}$$

As can be seen the analysing power depends on interference terms between scattering amplitudes whereas the differential cross section does not. A good example of the greater sensitivity of analysing powers is the elastic scattering of ^6Li and ^7Li [Jo]. The differential cross sections for both these reactions are found to be very similar. The $^TT_{20}$ analysing power though is found to be very different for the two projectiles. This reflects the different shapes of the ground state nuclei. The ground state of ^7Li is oblate and hence for this particular alignment there is a greater overlap of wavefunctions for a particular impact parameter than for a randomly oriented ^7Li beam. The aligned differential cross section is therefore less than the unaligned one and hence $^TT_{20}$ is negative as observed. ^6Li has a much more spherical ground state which is reflected in the small deviation of $^TT_{20}$ from zero.

Another advantage of analysing powers is that the strength parameter $X^{\lambda}_{s_a \to s_c}$ present in the scattering amplitudes (equation 2.30) cancels out in the expression for T_{KQ} if only one value of λ is considered. This parameter is difficult to determine and experimental data is often used in calculations (e.g. [Sh84]). This is a distinct hindrance when one wishes to draw conclusions from comparisons of data with calculations as any errors present in the data used for $X^{\lambda}_{s_a \to s_c}$ determination will propagate through to the results of the calculation.

Analysing powers also have the advantage of being less subject to systematic errors than cross sections. This is because analysing powers depend on a ratio whereas cross sections depend on an absolute number.

$$^TT_{20} = \left(\frac{Y_B - Y_A}{Y_B + Y_A}\right) \frac{1}{|t_{20}|} \tag{2.34}$$

As can be seen in the above equation any percentage errors which are the same in the two phases will cancel out. Any errors which are different in the two phases (e.g. possible errors in dead times) will cause an error in the ratio, but there will still be partial cancelation and hence the error is still less significant than it would be for a cross section determination. Suppose the errors in the yields in phases A and B are expressed in terms of a and b where $Y_A^{TRUE} = aY_A$ and $Y_B^{TRUE} = bY_B$.

$$ {}^{T}T_{20} = \left(\frac{Y_B(a+c) - Y_A(a)}{Y_B(a+c) + Y_A(a)}\right)\frac{1}{|t_{20}|} \tag{2.35} $$

where $b = a + c$ and c is small then

$$ {}^{T}T_{20} \approx \left(\frac{(Y_B - Y_A)a + Y_B c}{(Y_B + Y_A)a}\right)\frac{1}{|t_{20}|} \tag{2.36} $$

where $a(Y_B + Y_A) \approx a(Y_B + Y_A) + Y_B c$

$$ {}^{T}T_{20} \approx \left(\frac{(Y_B - Y_A)}{(Y_B + Y_A)} + \frac{c}{a}\frac{1}{(1 + Y_A/Y_B)}\right)\frac{1}{|t_{20}|} \tag{2.37} $$

The significant error here is of the order of c/a whereas for a cross sections errors add up. The determination of solid angles is another source of error for direct breakup cross sections which does not affect analysing powers. In order to determine the effective solid angles using a Monte Carlo code one requires a knowledge of the population of the $\alpha + t$ continuum as a function of relative energy (see section 4). This is determined either from calculations or data, both of which imply possible error.

The major disadvantage of analysing powers is the length of time required to achieve reasonable statistical errors. The errors quoted here are of the order of 25%. A more complete analysis than was possible in the time allowed for the experiment discussed in this thesis would have included the determination of other analysing powers such as T_{20} and iT_{11}. These analysing powers are expected to have a relative energy dependence thus requiring a large number of counts to achieve reasonable errors for reasonable relative energy bins.

2.7 Cross sections

Differential cross sections as well as analysing powers were determined for the data acquired. In chapter 5 the cross sections are compared to the semi-classical Coulomb calculation mentioned in section 1.2.4 this calculation will therefore be described in a little more detail below.

The scattering amplitudes used to determine the differential cross sections are those given by equation 2.30. The assumptions used to derive the expression for the differential cross section given in equation 1.3 are therefore that the excitation is small enough to allow the assumption of a Rutherford orbit and that first order perturbation theory may be used. These approximations allow the differential cross section to be written as the excitation probability times the Rutherford differential cross section.

$$\frac{d\sigma}{d\Omega} = \left(\frac{d\sigma}{d\Omega}\right)_{Ruth} \frac{1}{2s_a+1} \sum_{\alpha\gamma} |F_\gamma^\alpha|^2 \tag{2.38}$$

which can then be written

$$d\sigma_{E\lambda} = \left(\frac{Z_1 e}{\hbar v}\right)^2 a^{-2\lambda+2} B(E\lambda) df_{E\lambda}(\theta, \xi) \tag{2.39}$$

The reduced transition probability $B(E\lambda)$ is related to the $X^\lambda_{s_a \to s_c}$ in equation 2.30 and the $df_{E\lambda}$ is related to the orbital integral R_λ [Al]. A knowledge of the reduced transition matrix element is required in order to determine $B(E\lambda)$. This requires a knowledge of the wave functions of the appropriate levels and hence is not simple to determine. This absence of the necessity to determine this parameter in the analysing power calculation discussed in section 2.5 is one of their major advantages.

One way of determining the $B(E\lambda)$ is by using experimental data from the inverse, namely photo-disintegration, reaction $\gamma + {}^7Li \rightarrow \alpha + t$. The $B(E\lambda)$ describing this reaction is the same as that describing the Coulomb breakup of ${}^7Li$ where γ is a virtual photon. The $B(E\lambda)$ can be determined using (see [de, Sh84])

$$\sigma_{dis} = \frac{8\pi^3(\lambda+1)}{\lambda[(2\lambda+1)!!]^2}\left(\frac{E_\gamma}{\hbar c}\right)^{2\lambda-1} B(E\lambda,\varepsilon) \tag{2.40}$$

where E_γ is the photon energy, ε is the α t relative energy and σ_{dis} is the photo-disintegration cross section. Unfortunately data for low enough energies do not exist, however data for the α t fusion reaction do exist at the appropriate energies. The differential cross sections for this reaction may be related to those for the photo-disintegration reaction using the reciprocity theorem [Bl].

Considering only the lowest possible multipole term i.e. $\lambda = 1$, $B(E1,\varepsilon)$ is given by

$$B(E1,\varepsilon) = \frac{9}{16\pi^3}\frac{\hbar c}{E_\gamma^3}\frac{\mu c^2}{2}\varepsilon\sigma_{fus}(\varepsilon) \tag{2.41}$$

Substituting this equation into equation 2.39 one obtains

$$d\sigma_{E1}(\varepsilon,\theta) = C\frac{\varepsilon}{E_\gamma^3}\sigma_{fus}(\varepsilon)df_{E1}(\varepsilon,\theta) \tag{2.42}$$

where σ_{fus} is the fusion cross section and C is a constant.

The fusion cross section data that were used were taken from [Ot76]. These data cover the relative energy range 0.17 to 0.9 MeV. The fusion cross section data were extended to 3.0MeV by using the direct capture model [Sh88a] and normalizing the result to the data from [Ot76]. The distribution used is shown in figure 2.5. The differential cross section is evaluated by integrating equation 2.42 over the required relative energy range. In this case the range integrated over was $0.03 - 1.8$MeV and a plot of the result is shown in figure 5.17.

The differential cross section for the sequential breakup of ^7Li was also calculated using equation 2.39. This breakup goes via the $\frac{7}{2}^+$ 4.63MeV state of ^7Li. The lowest possible multipole is therefore an E2 one. The reduced transition probability was taken to be 17.5 e^2fm^4 [Sh89]. The result of this calculation is shown in figure 5.18.

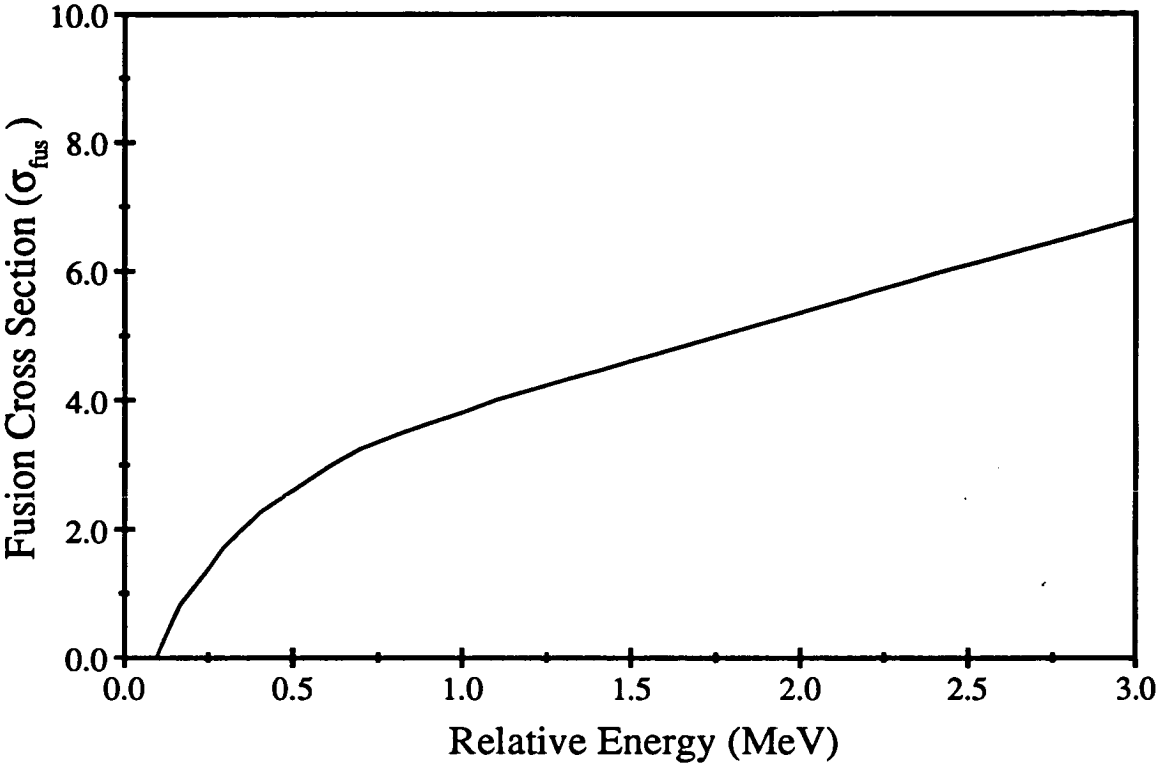

Figure 2.5: *The α t fusion data.*

2.8 Kinematics

The reactions that are of interest in this thesis result in three body final states e.g. $^{120}Sn + ^{7}Li \longrightarrow ^{120}Sn + \alpha + t$. At the energies concerned here these reactions may be described by non-relativistic three body kinematics. Using the notation of de Meijer [Me85] these reactions may be represented by

$$\mathrm{a} + \mathrm{A} \longrightarrow 1 + 2 + 3$$

where a represents the projectile, A the target and 1, 2 and 3 the outgoing particles.

For a fixed projectile energy there are 10 unknown quantities required to completely describe the kinematics of this system. These are the 9 momentum components of the outgoing particles and the total excitation energy of these particles (E_x^{tot}). This last unknown can be expressed in terms of the 3 body Q-value Q_3 which is equal to $Q_3^g - E_x^{tot}$ where Q_3^g is the ground state to ground state Q-value

(i.e. $m_a + m_A - m_1 - m_2 - m_3$). Energy and momentum conservation provide 4 equations hence 6 of the 10 unknowns must be experimentally determined for a kinematically complete solution. In the experiment described in this thesis the 6 unknowns measured are the momentum components of the projectile like fragments. These are the most convenient particles to detect because they are forward focused and are of a velocity similar to that of the beam. The variables measured are $E_1, \theta_1, \phi_1, E_2, \theta_2, \phi_2$ where the Es are the energies, θs are the polar angles and the ϕs are the asymuthal angles of particles 1 and 2. A relation between E_1 and E_2 for a given Q_3 can be derived from the 4 energy and momentum conservation relations already mentioned. The relation is

$$\begin{aligned} Q_3 + E_a\left(1 - \frac{m_a}{m_3}\right) &= \frac{1}{m_3}(E_1(m_1 + m_3) + E_2(m_2 + m_3) \\ &+ 2(m_1 m_2 E_1 E_2)^{1/2}\cos\theta_{1-2} \\ &- 2(m_a m_1 E_a E_1)^{1/2}\cos\theta_1 \\ &- 2(m_a m_2 E_a E_2)^{1/2}\cos\theta_2) \end{aligned} \tag{2.43}$$

where $\cos\theta_{1-2} = \cos\theta_1\cos\theta_2 + \sin\theta_1\sin\theta_2\cos(\phi_1 - \phi_2)$, θ_{1-2} is the angle between the velocity vectors of the particles 1 and 2.

This equation is a closed curve in E_1, E_2 space an example of which, curve (3), is shown in figure 2.6. These curves will in subsequent chapters be refered to as kinematic loci. Whether or not a complete curve appears in positive E_1, E_2 space depends on the masses involved in the reaction. If the mass of the target is much greater than that of the projectile and the detected fragments, as in the cases considered herein, then only part of the curve will appear in this quadrant. Different curves for the same reaction correspond to different values of Q_3. (e.g. curves (1) and (2) in figure 2.6).

The particular energies of the detected particles as well as satisfying equation 2.43 depend on the relative energy (ϵ_{12}) between them. This is the total kinetic energy of these particles in their centre of mass system and is the relevant quantity in determining whether a reaction is sequential or direct. In a sequential

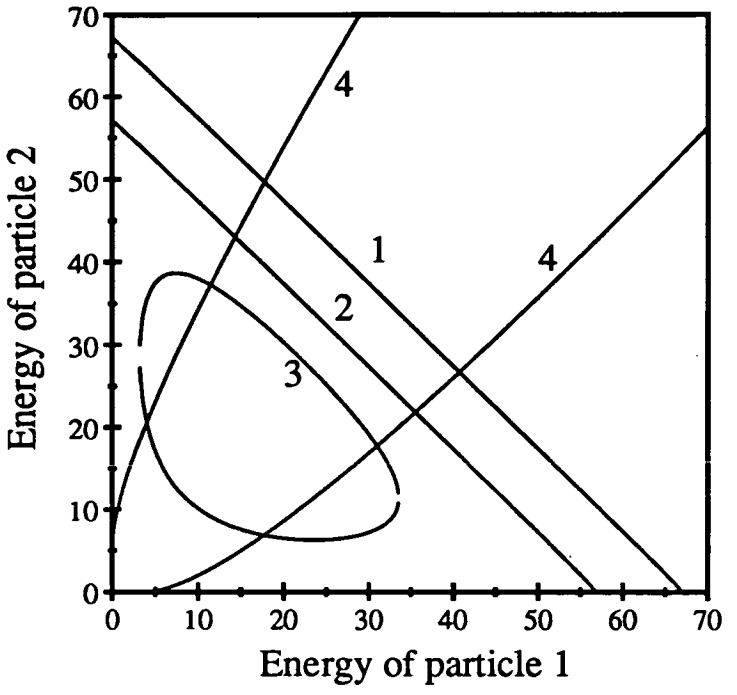

Figure 2.6: *Curves 1, 2 and 3 were produced by equation 2.43 and curve 4 was produced by equation 2.44. Curves 1 and 2 are for different excitations of* ^{120}Sn *in the reaction* $^{120}Sn(^7Li, \alpha + t)^{120}Sn^*$. *In order to produce a complete curve in* E_1, E_2 *space a target of similar mass to the projectile is required. Curve 3 was produced by the reaction* $^3H(^7Li, \alpha + t)$. *Curve 4 corresponds to a relative energy of 2.16MeV. (*θ*= 9°,* $\Delta\phi$*= 4.6° see figure 3.7 for definitions of angles).*

reaction where particles 1 and 2 are emitted in their ground states the relative energy is equal to the excitation energy of the intermediate particle that breaks up plus the ground state to ground state Q-value for the reaction $12^* \longrightarrow 1 + 2$ where 12^* is the intermediate nucleus ($\varepsilon_{12} = E_x^{12} + Q_g^{12}$). The steps in a sequential process can be written

$$a + A \longrightarrow 12^* + 3 \longrightarrow 1 + 2 + 3$$

In a sequential reaction the relative energy therefore takes discrete values. Conversely in a direct reaction no intermediate nucleus exists and the relative energy does not take discrete values. The magnitude of the relative energy ε_{12} depends

on the energy given to the fragments 1 and 2 in the projectile target interaction. Any final state interactions however will cause the experimental relative energy to be different from ε_{12}.

$$\varepsilon_{12} = K_1^c + K_2^c = \tfrac{1}{2}\mu v_{1-2}^2$$

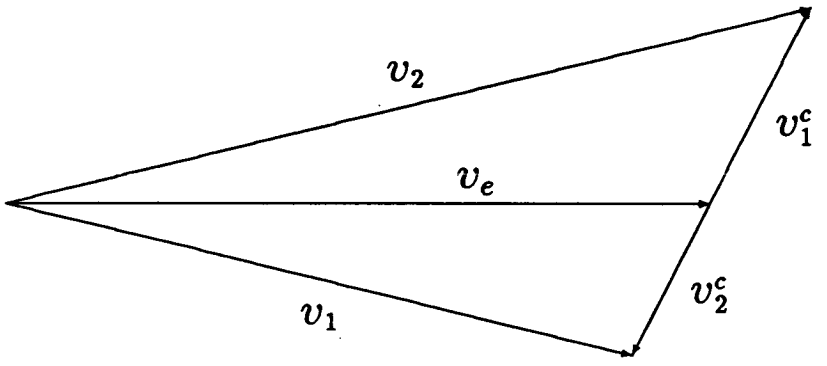

Figure 2.7: *The velocity vector diagram shows the relation between the velocities of the breakup fragments in their centre of mass system* v_1^c, v_2^c *and their laboratory velocities* v_1, v_2. $v_{1-2} = v_1^c + v_2^c$ *and* v_e *is the laboratory velocity of the ejectile that breaks up. The* K*s are the centre of mass kinetic energies of the particles 1 and 2,* θ_{1-2} *is the angle between the vectors* v_1 *and* v_2 *and* μ *is the reduced mass.*

The velocity vector diagram in figure 2.7 shows the relation between the laboratory energies E_1 and E_2 and ε_{12}. The relative energy ε_{12} is given by

$$\begin{aligned} \varepsilon_{12} = K_1^c + K_2^c &= \frac{m_1 m_2}{2(m_1+m_2)} v_{1-2}^2 \\ &= \frac{m_2 E_1 + m_1 E_2 - 2(m_1 m_2 E_1 E_2)^{1/2}\cos\theta_{1-2}}{m_1+m_2} \end{aligned} \tag{2.44}$$

where K_1^c and K_2^c are the kinetic energies of the particles in their centre of mass. For a given value of ε_{12} this equation is an elipse in E_1, E_2 space. For given values of Q_3 and ε_{12} the solutions to the equations 2.43 and 2.44 are given by the intersections of the curves generated by those equations. There are therefore a

maximum of four solutions to these two equations, but when particle 3 is much heavier than 1 and 2 only two solutions exist (see figure 2.6).

The above discussion shows that the identification of sequential and direct reactions is possible by the creation of a 2D E_1, E_2 spectrum. It is often easier, in practice, to work with 1D projected energy spectra. The ones used in this thesis are E_1 (or E_2) spectra and $E_1 + E_2$ spectra. The former allows identification of direct and sequential events and the latter shows the excited states of the recoiling nucleus (particle 3).

Chapter 3

Experimental Method

3.1 Introduction

The experiment to acquire the data discussed in this thesis was performed at the Nuclear Structure Facility (NSF) at the S.E.R.C.'s Daresbury Laboratory. The system used consists of a polarized source which injects ions into a Tandem Van de Graaff which in turn supplies accelerated ions to the experimental area. Figures 3.1 and 3.2 show the Tandem Van de Graaff and the experimental areas.

3.2 The Polarized Source

The Polarized Ion Source (P.I.S.) [Ka89] now in operation at the NSF is based on the source used at the Max-Planck Institute in Heidelburg [Kr84]. The phenomenon that the source utilizes to produce polarized nuclei is the hyperfine coupling between nuclear and electronic spin. As a result of this coupling the polarization of an atom followed by the removal of its electrons leaves a polarized nucleus.

A schematic diagram of the source is given in figure 3.3. It is housed on a HT platform which can be kept at a voltage of up to 500kV. ^7Li is vapourized in the oven and emerges as an atomic beam. This beam passes through a quadrupole Stern-Gerlach magnet which only focuses the $m_J = +\frac{1}{2}$ electronic spin substate

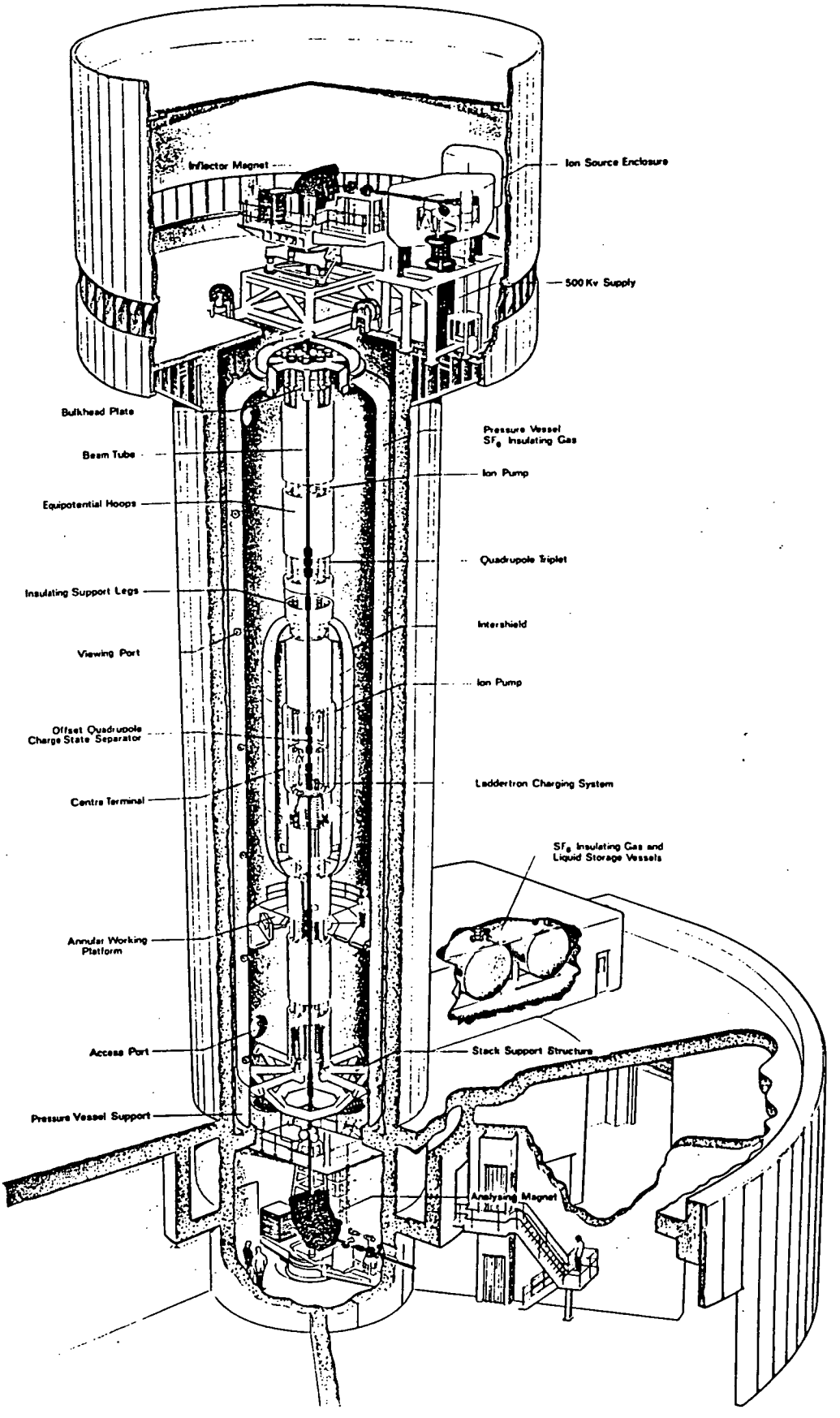

Figure 3.1: *A cut away view of the tandem Van de Graaff at the Nuclear Structure Facility at Daresbury Laboratory.*

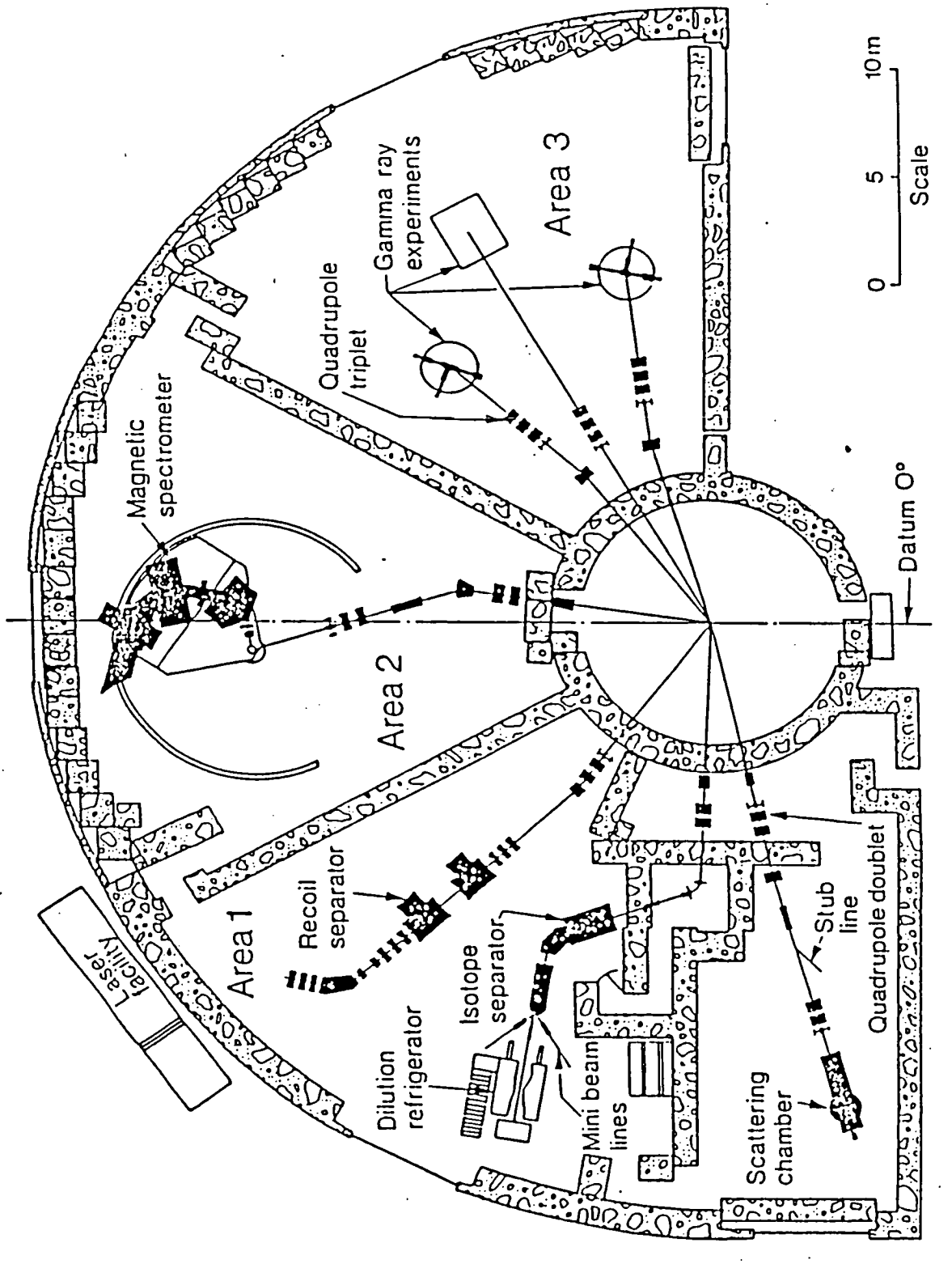

Figure 3.2: *Plan view of the experimental areas. All experiments took place in the scattering chamber on the 79° line in area 1.*

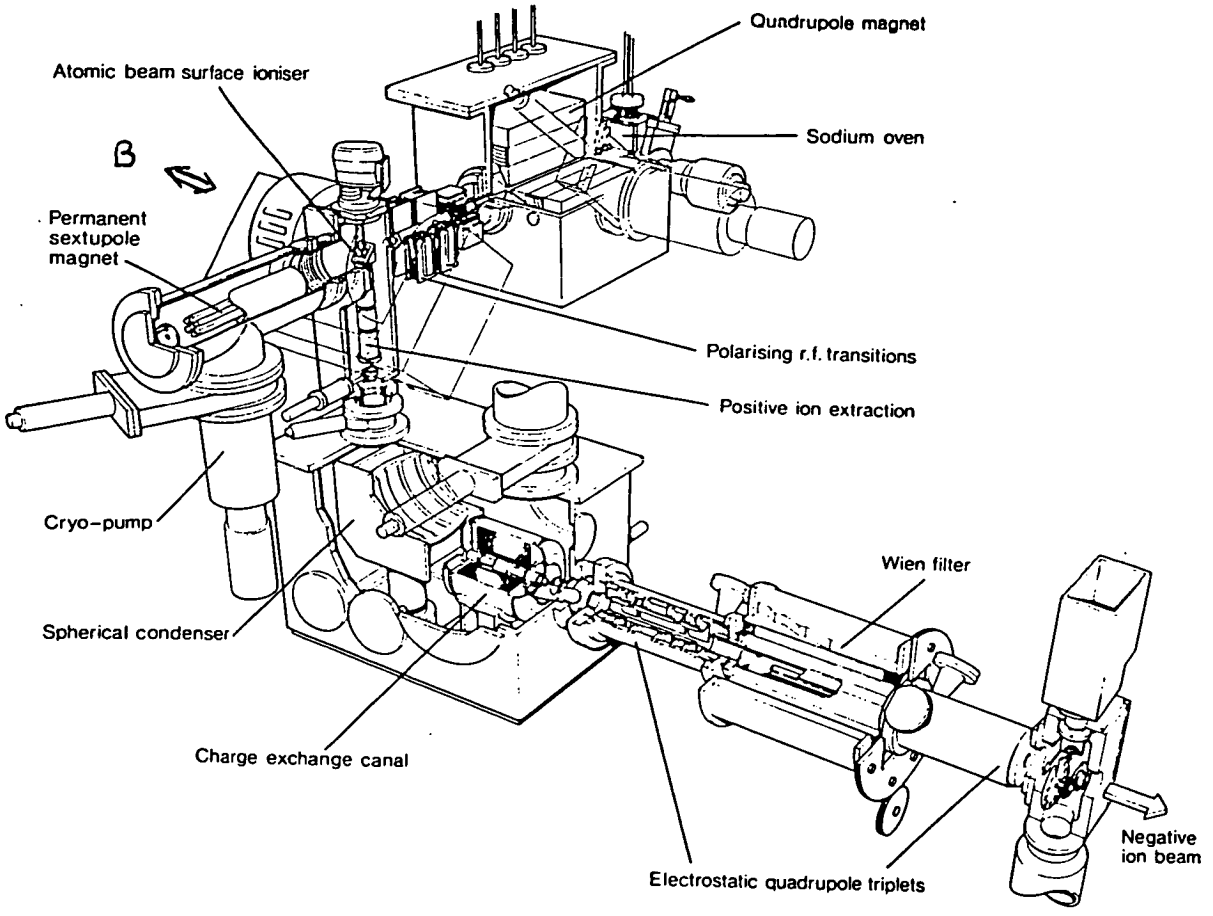

Figure 3.3: *Schematic diagram of the polarized source at the Nuclear Structure Facility at Daresbury laboratory.*

The B field which is the natural z axis referred to in section 2.3 is established in the rf transitions units. Its direction is indicated by the arrow in figure 3.3. ~~component. The beam then passes through a system of rf transition units.~~ In order to produce the polarization utilized in the experiment, transitions between the 2-8 and the 4-6 levels on the Breit-Rabi diagram (figure 3.4) were used. After emerging from the Stern-Gerlach magnet the beam is then ionized on a heated tungsten strip placed at 45° to the beam axis. This takes place in a dipole field to prevent depolarization. The resultant positive beam is then brought to a focus at the centre of the Cs charge exchange canal and a negative beam is produced with an efficiency of $\sim$ 5%. This occurs because Cs is less electropositive than Li allowing the positive Li ions to acquire electrons from the Cs atoms. This

negative beam is brought to a focus in the Wien filter, where it has an energy of 5.5keV, by an electrostatic quadrupole triplet lens. The Wien filter consists of crossed electric and magnetic fields. The direction of the polarization symmetry axis can be altered by physically rotating the assembly and by altering the field strengths accomplished by changing the current in the Wien filter magnet. The desired direction now having been selected the beam is passed to the Tandem Van de Graaff accelerator.

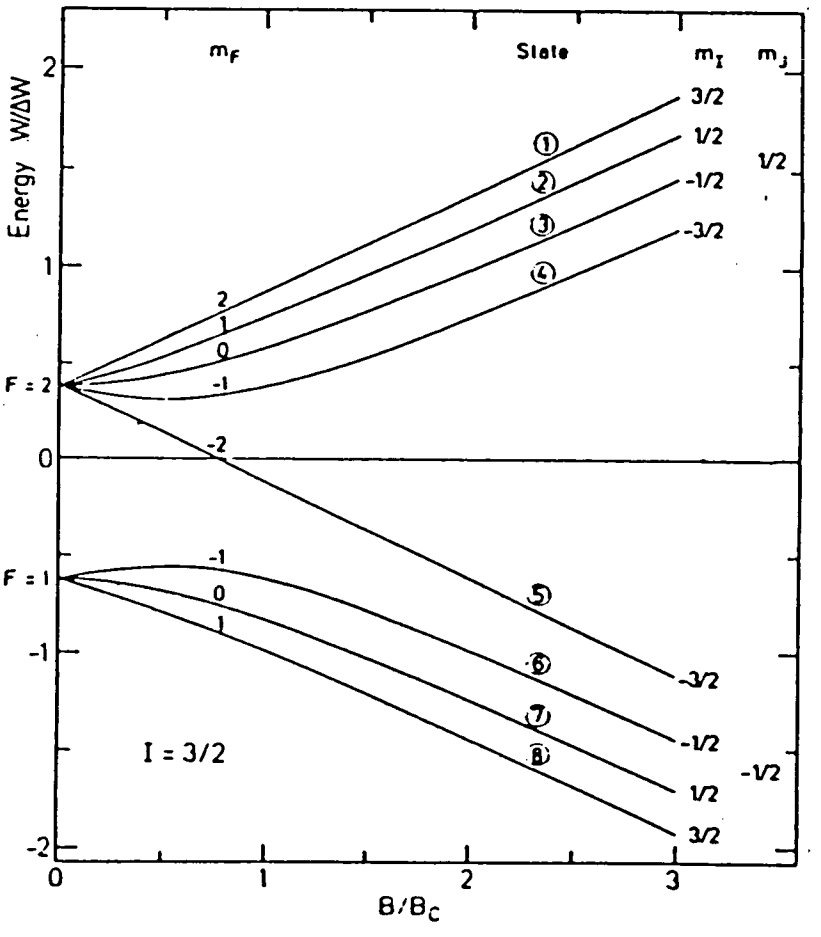

Figure 3.4: *The Breit-Rabi diagram showing the hyperfine splitting of atomic levels in an external magnetic field for an atom for electronic spin J=1/2 and nuclear spin I=3/2. B_c is the critical field which is 28.8mT for ^7Li [St77].*

The direction of the magnetic field in the source is a symmetry axis. If the

logical choice of the the z axis for the symmetry axis is made, then only the t_{KQ} where $Q = 0$ are non zero. The nuclear spin is 3/2 hence the maximum possible K is 3 (2s). This means that only three polarizations can be produced in the source. These can be written in terms of their substate populations, N_m using

$$t_{KQ} = \langle \tau_{KQ} \rangle = Tr(\tau_{KQ}\rho)/Tr(\rho) \tag{3.1}$$

$$t_{10} = \frac{3N_{\frac{3}{2}} + N_{\frac{1}{2}} - N_{-\frac{1}{2}} - 3N_{-\frac{3}{2}}}{\sqrt{5}} \tag{3.2}$$

$$t_{20} = N_{\frac{3}{2}} - N_{\frac{1}{2}} - N_{-\frac{1}{2}} + N_{-\frac{3}{2}} \tag{3.3}$$

$$t_{30} = \frac{N_{\frac{3}{2}} - 3N_{\frac{1}{2}} + 3N_{-\frac{1}{2}} - N_{-\frac{3}{2}}}{\sqrt{5}} \tag{3.4}$$

For the particular transitions used these are

$$t_{10} = \frac{1}{2\sqrt{5}}, \qquad t_{20} = \pm\frac{1}{2}, \qquad t_{30} = \frac{1}{\sqrt{5}} \tag{3.5}$$

t_{20} is positive for the transition 2-8 (phase B) and negative for the transition 4-6 (phase A).

3.3 Accelerator and Beam Line

A schematic diagram of the transport of the beam from the source to the polarimeter is given in figure 3.5. The beam emerging from the Wien filter undergoes an acceleration to 320keV before it passes through a 90° inflection magnet and enters the accelerator. The negative beam is accelerated towards a central terminal held at a positive potential. On reaching this point the ions are stripped of electrons by passing through a carbon foil. The now positively charged ^7Li ions are accelerated away from the central terminal. A quadrupole triplet after the terminal selects the 3+ charge state. The final energy of the beam is

$E = E_0 + (1 + Q)$eV where E_0 is the small amount of energy acquired in preacceleration, Q is the charge of the stripped atom and V is the voltage at which the central terminal is held. In this experiment $E = 70$MeV. The depolarization of a ^{23}Na beam during its passage through the accelerator is estimated to be $\sim 2\%$ [Ka89]. The depolarization for a ^{7}Li beam is expected to be of a similar magnitude.

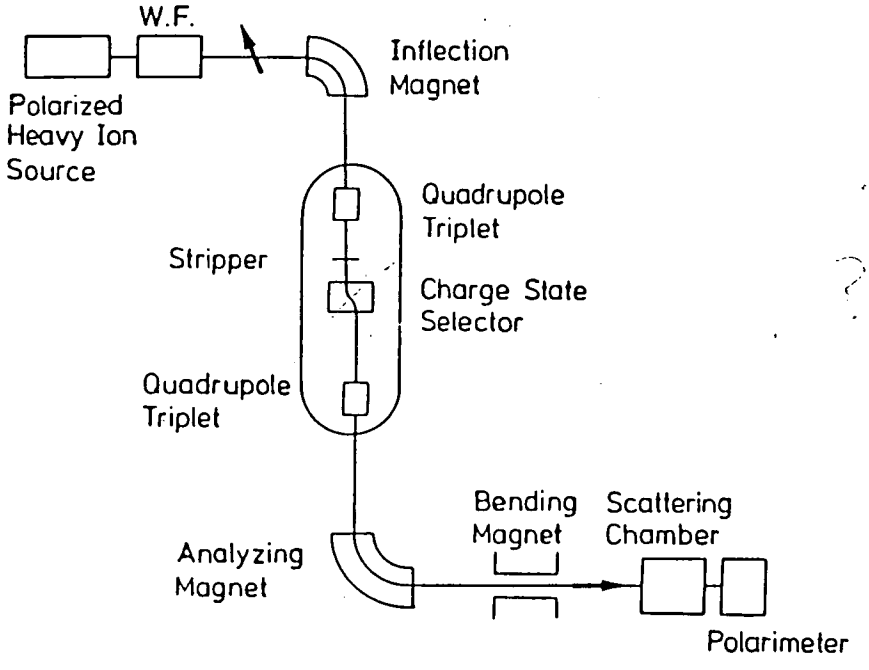

Figure 3.5: *Diagram of the path of the beam from the polarized source via the Tandem Van de Graaff to the polarimeter. Note that the diagram is schematic the beam pipe is not offset at the Charge state selector*

At the bottom of the accelerator the beam passes through a 90° analysing magnet and enters the 79° beam line shown in figure 3.6. On leaving the accelerator the beam size is defined by a set of x-y slits. It is then focused by a quadrupole doublet, deflected through 5° by a switching dipole magnet and finally focused into the chamber through a second quadrupole doublet. A 2mm×2mm collimator was positioned at 0.75m from the target and an 4mm×4mm antiscatter aperture was at 20cm from the target. At the target the polarization symmetry axis lay in

the y direction in the helicity frame.

3.4 Targets

The target used was one of ^{120}Sn. This was manufactured at the target preparation laboratory at the NSF. The target was a thin self supporting sheet of ^{120}Sn mounted on an aluminium frame. The target thickness was determined by measuring the energy loss of 5.5MeV α particles passing through it. The thickness of the target was determined to be 2.3±0.5 mg/cm^2. The code DEDX was used to determine the thickness from the energy loss. This code has an inherent error generally quoted as being $\sim$ 10% e.g. [Ma88, Yo89]. The target was not a major contributor to the observed resolution of the coincidence particles. The affect on the resolution of the lowest energy α particles, which of all the particles considered would have lost the most energy, caused by the variation in distance from the target surface of the breakup process, was $\sim$ 0.3MeV. The finite opening angle of the detection system imposes a minimum possible resolution. This is easily found using the Monte Carlo code described in chapter 4 and was determined to be $\sim$ 0.7MeV. This is the same as the observed resolution and it is therefore almost entirely due to the finite solid angle subtended by the detector system.

3.5 Detection System

The factors that determine the choice of detection geometry, for a kinematically complete measurement of the two breakup products, are the following.

a) Range of relative energy, ε.

b) Angle of detection system to the beam, θ.

c) Energy resolution required.

d) Coincidence rate.

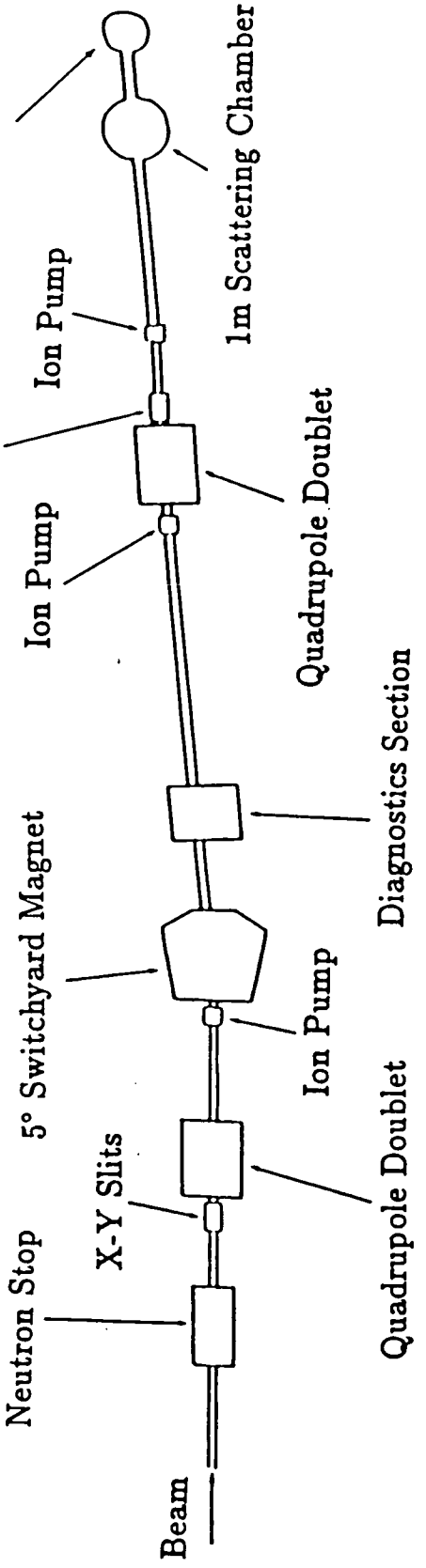

Figure 3.6: *Schematic diagram of the 79° beam line in area 1.*

The detection system was designed with the aim of producing the smallest values of ϵ and θ possible. The detection system used is illustrated in figures 3.7 and 3.8. The system consisted of two pairs of detectors at equal angles on opposite sides of the beam. The pairs were centred on the horizontal plane and the telescopes were equidistant from it. The collimator apertures were 8mm wide, 6mm high, separated by 6mm and were placed at 150mm from the target. Two sets of detectors are required to enable the calculation of ${}^{T}T_{20}$ when, as in this case, two polarized and no unpolarized phases are used. The configuration also minimised systematic errors due to any beam shift on target. Veto detectors, not shown in the diagram, were placed behind each pair in order to reject high energy low charge particles.

A restriction which the system design had to incorporate was that the active edges of the Si(Li) detectors could not be placed any closer together than 5mm. In a previous experiment to obtain cross section data on the breakup of ${}^{7}Li$ into an α and a t [Da87] the minimum angle at which data was acquired was 11.5°. Data at a smaller angle than this was desired for the present experiment. The smallest θ obtainable at a fixed distance from the target, was limited by the physical size of the mount, hence the θ chosen also defined the count rate given that the detector area and separation were fixed. The Monte Carlo code described in chapter 4 was used in order to determine counting rates for various target detector distances and it was concluded that a minimum angle of 9° provided the best compromise. Measurements at this angle entailed placing the detectors at a distance of 150mm from the target and the consequent minimum ϵ detectable for an α t coincidence was 0.03MeV. The detectors were kept at this distance throughout the run because the improvement in count rate that would have been obtained by moving the detectors closer would have been negated by the time that the operation to move them would have taken.

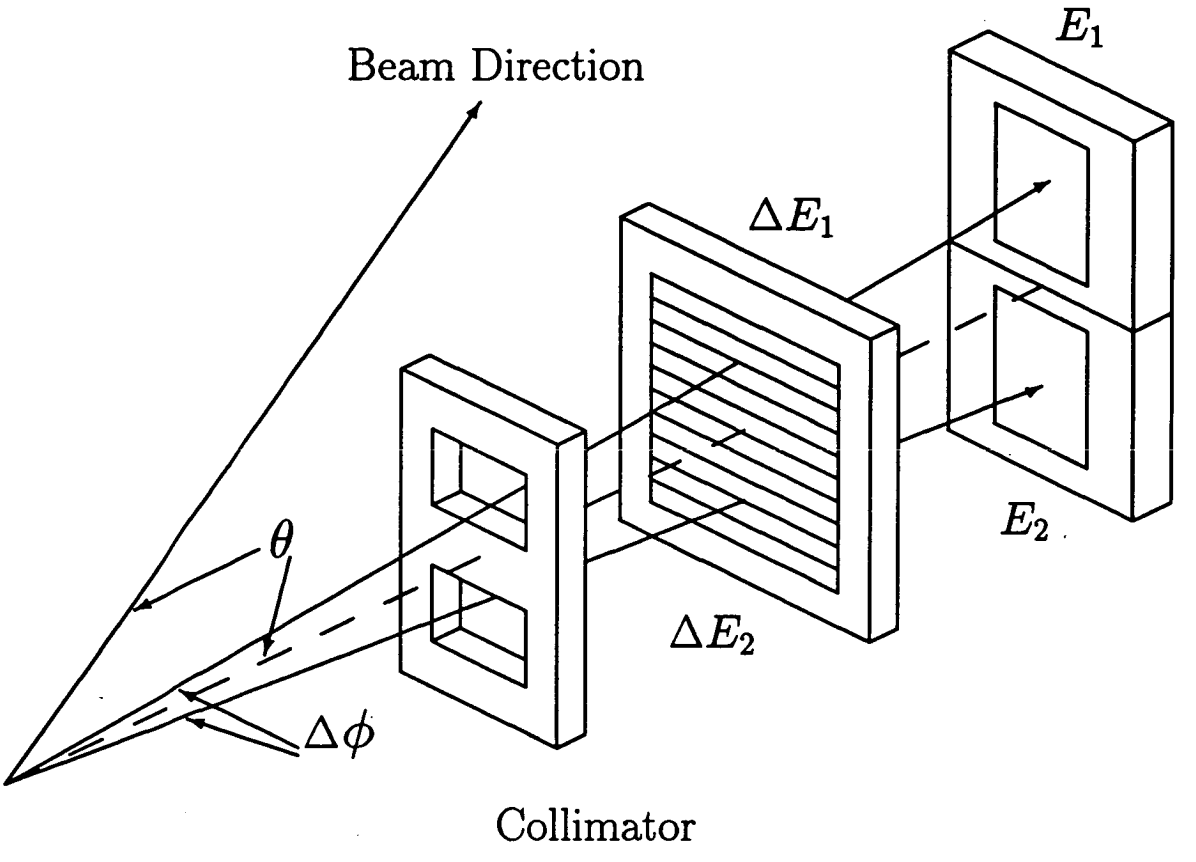

Figure 3.7: *Diagram of one telescope pair. Veto detectors (not illustrated) were place behind the E detectors. (N.B. ϕ in this diagram is not a polar angle.)*

3.6 Detectors

The E detectors were Lithium drifted Silicon detectors (Si(Li)). The ε requirement mentioned in the previous section necessitated a special design of detector case to enable the active edges of the detectors to be a minimum of 5mm apart. The active thickness of the Si(Li), determined before the experiment using electrons from a Bi source, was $\sim$ 4.5mm. The electrons were first allowed to enter the detector via its front face. Assuming that the detector did not possess a dead layer on its front face this allowed an energy calibration. On allowing the electrons to impinge on the back face of the detector a reduction in their detected

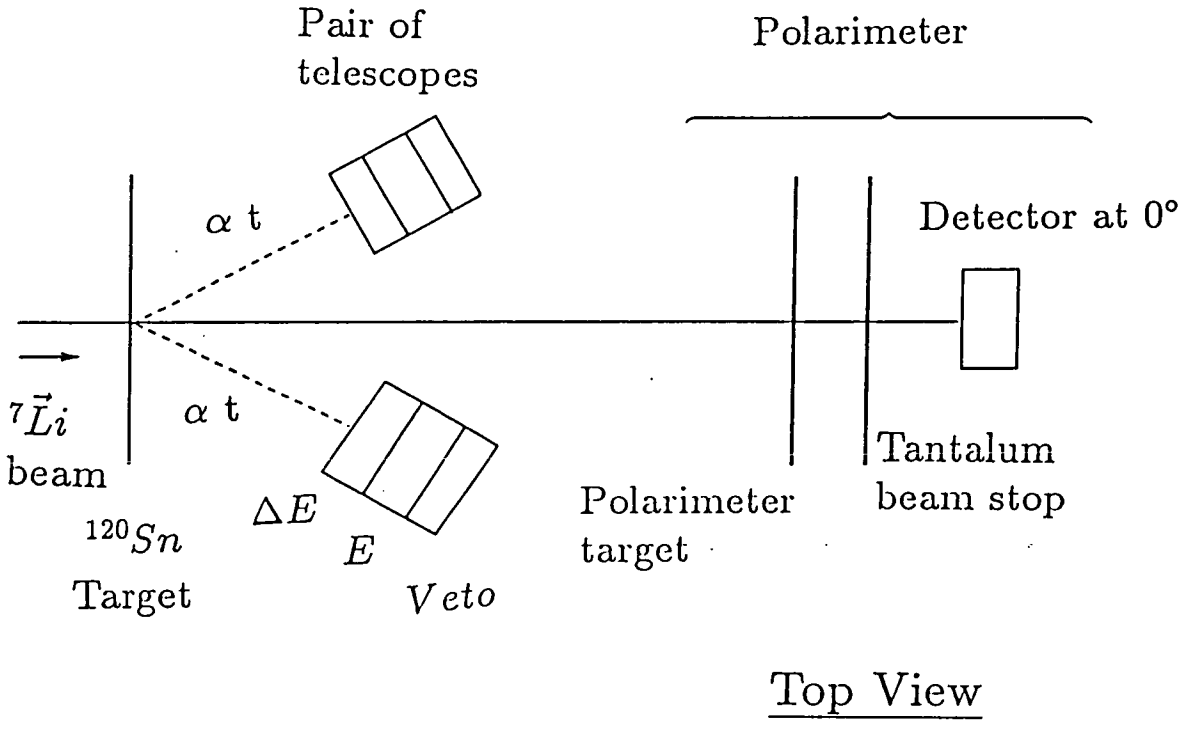

Figure 3.8: *Schematic diagram of the layout of the detectors and polarimeter.*

energy was observed and taken to be due to them losing energy in a dead layer. The ΔEs were Silicon Strip detectors (SSD) about 230μm thick. These are p-n junction detectors [Yo87, Ma88]. The active area of a single detector was divided into two by grouping the strips together in two groups of five strips. Hence one SSD provided the ΔEs for both telescopes in a pair. The veto detectors were also Si(Li)s.

Problems were encountered with both the Si(Li) detectors and the strip detectors. These problems and their affect on the results are described below.

3.6.1 Charge Sharing in Strip Detectors

Two distinct types of charge sharing have been observed for strip detectors. When particles are incident on strip detectors a small number of coincidences are

observed between adjacent strips. These coincidences are of two types. The first results in a reduced height positive pulse being seen in coincidence with negative one of a magnitude equal to the reduction in magnitude of the positive pulse. The second results in two positive pulses being observed, the sum of their magnitudes being equal to the total observed when no sharing takes place.

Positive negative charge sharing in the strip detectors used as ΔEs manifests itself as a reduction in the energy detected for a particular particle. This effect becomes more pronounced the higher the ionizing ability of the particle detected. The effect can clearly be seen for the ^7Lis in the $\Delta E, E$ plot in figure 3.9. This plot shows that for a particular energy registered in the E detector a spread of energies, all the same or lower than the true energy, is registered in the ΔE detector. The effect is not easily observable for the Z=2 and Z=1 particles. This phenomenon was first observed for α particles of energies around 10MeV per nucleon by J. Yorkston [Yo87, Yo89] the proposed mechanism for charge sharing is described below.

Charge sharing occurs when particles enter the interstrip region on strip detectors. A cross section of such a detector is shown in figure 3.10. Strip detectors are biased by applying a negative voltage to the p+ (front) side of the detector. The existence of a leakage current causes a steady flow of holes to the negatively biased strips. The interstrip region consists of a highly insulating material, SiO_2, there cannot therefore be a flow of electrons to this point, resulting in a build up of positive charge. The amount of positive charge in this region will reach an equilibrium value because the charge already in the region will repel further charge from reaching it. The presence of this charge results in a reversal of the field in a small area around the interstrip region. A potential minimum is thus created near to the surface in this area.

When a highly ionizing particle enters this interstrip region some or all of the electrons created instead of travelling towards the back of the detector (anode) become trapped in the area of field reversal. The proximity of the created charge to the area of field reversal dictates the fraction of charge trapped hence this effect

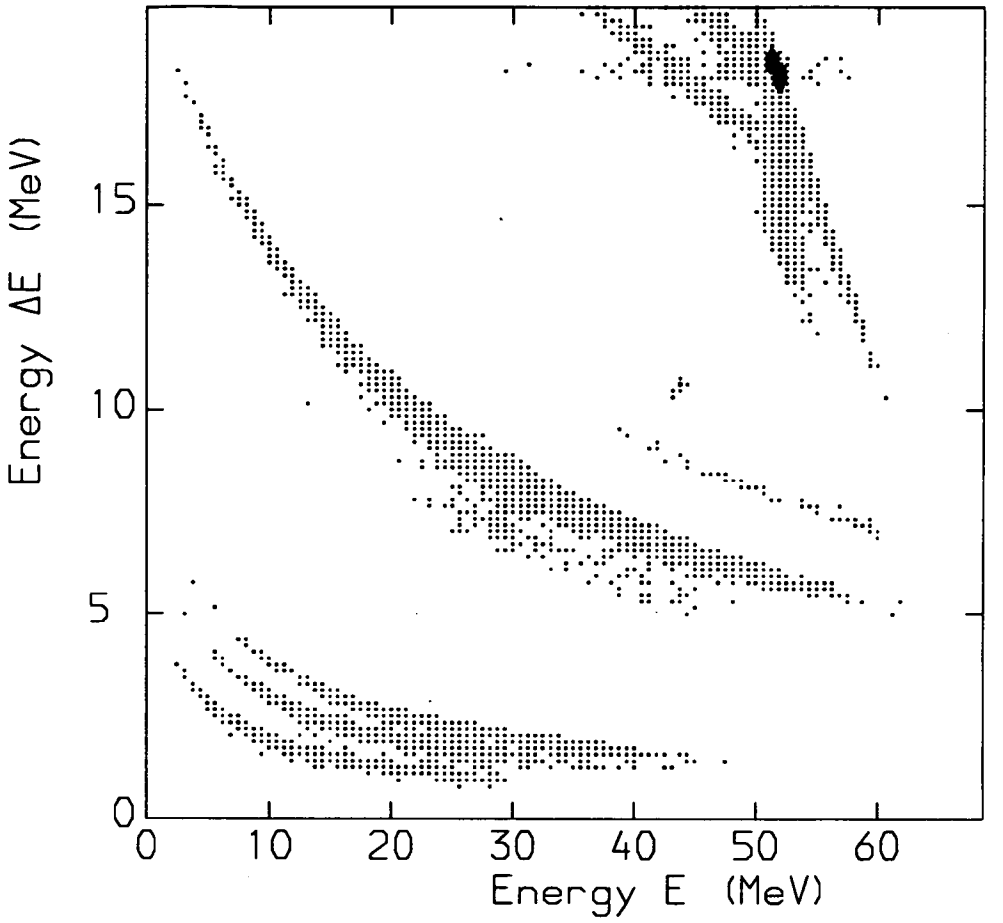

Figure 3.9: $\Delta E, E$ *plot for a telescope containing a Berkeley Si(Li).*[1]

is a function of Z. The electrons then induce charge on both strips adjacent to the gap before recombining with holes. This results in a reduced height positive pulse on one side and a coincident negative pulse on the other.

Positive positive charge sharing which is a result of the electrons created when a particle enters the inter strip region just being shared between two adjacent strips, was not a problem in this experiment. In the configuration in which the strip detectors were used any shared charge would have been summed back up before being registered.

The positive negative charge sharing only occurs for a very small percentage of particles entering the detector and though obvious for elastic ^7Lis it is not

[1] The lack of tailing due to lower energy ^7Li in the figure is mearly a consequence of the ploting routine. The tailing exists but the low number of counts makes it invisible in the plot.

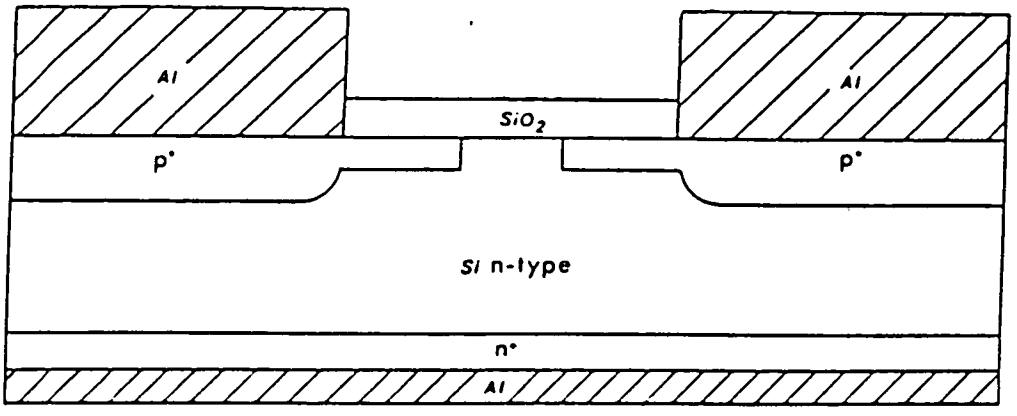

Figure 3.10: *Cross section of a strip detector showing the interstrip region.*

observable for Z=1 and Z=2 particles on a $\Delta E, E$ plot and therefore probably has very little affect on the results. As already mentioned in section 2.6 processes which affect both polarized phases result in smaller errors for analysing powers than for cross sections. This is a result of the fact that analysing powers are calculated from ratios and hence such errors tend to cancel out.

3.6.2 Problems with Si(Li) Detectors

Of the four Si(Li) E detectors used three were made at the Lawrence Berkeley Laboratory in California and one was made by Enertec. The $\Delta E, E$ plot in figure 3.11 for the Enertec detector reveals a problem with the Si(Li) as well as the strip detector.

Lobe 1 shows a spread of energies in the E detector for a fixed energy in the ΔE detector. This is probably due to a non uniform junction on the front face of E the detector. This would result in a spread of energies and would have a greater affect on higher charge and mass particles that would cause more ionization close to the surface. As can be seen from figure 3.11 the effect is much harder to see for α particles and does not appear to affect the charge one particles at all.

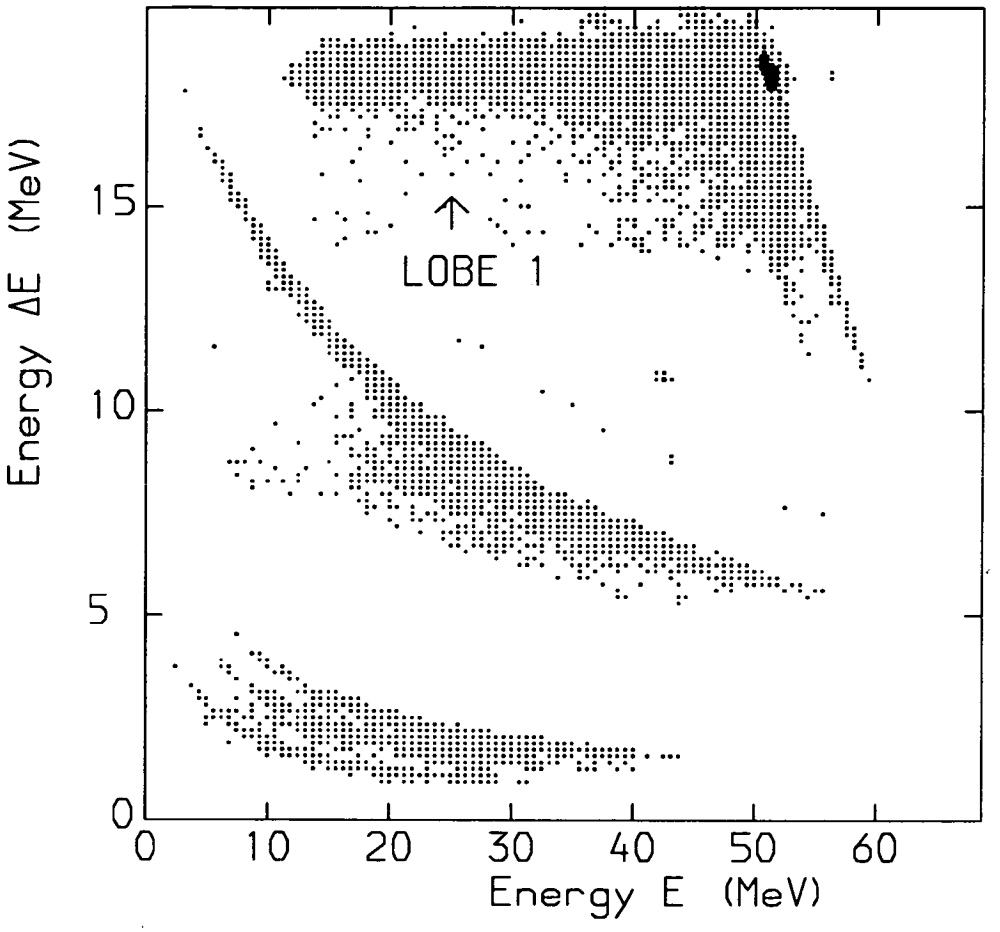

Figure 3.11: *$\Delta E, E$ plot for the telescope containing the Enertec Si(Li).*

This problem results in poor mass resolution for this telescope. A comparison of the particle identification, PI, spectra in figure 3.12 shows that the ^3He and ^4He particles are not well resolved and that both these peaks have tails. Also visible is the tail from the ^7Li peak. This however appears to have reduced to zero before reaching the ^4He peak. Previous work [Da87] however has shown that the differential cross sections for a ^3He particle in coincidence with d, t or ^3He is negligible, therefore the ^4He mass gate used was set around all ^3He and ^4He particles.

A problem was also encountered with the Berkeley Si(Li)s. It was found that for α, t coincidences it was impossible to choose a gain such that all the sequential

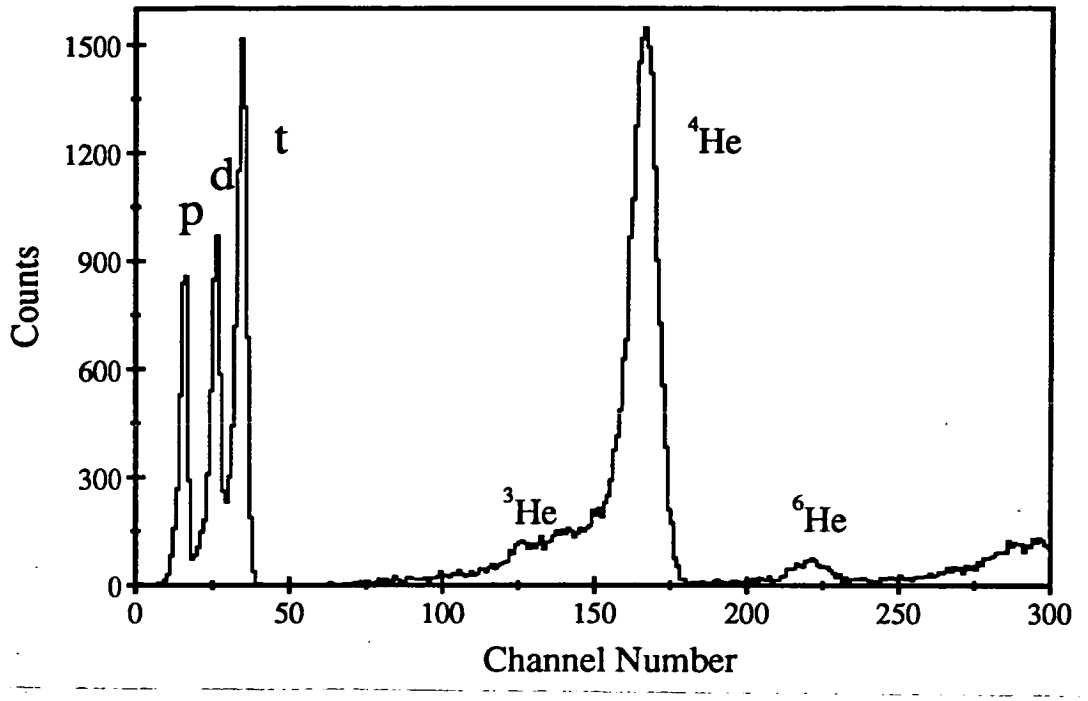

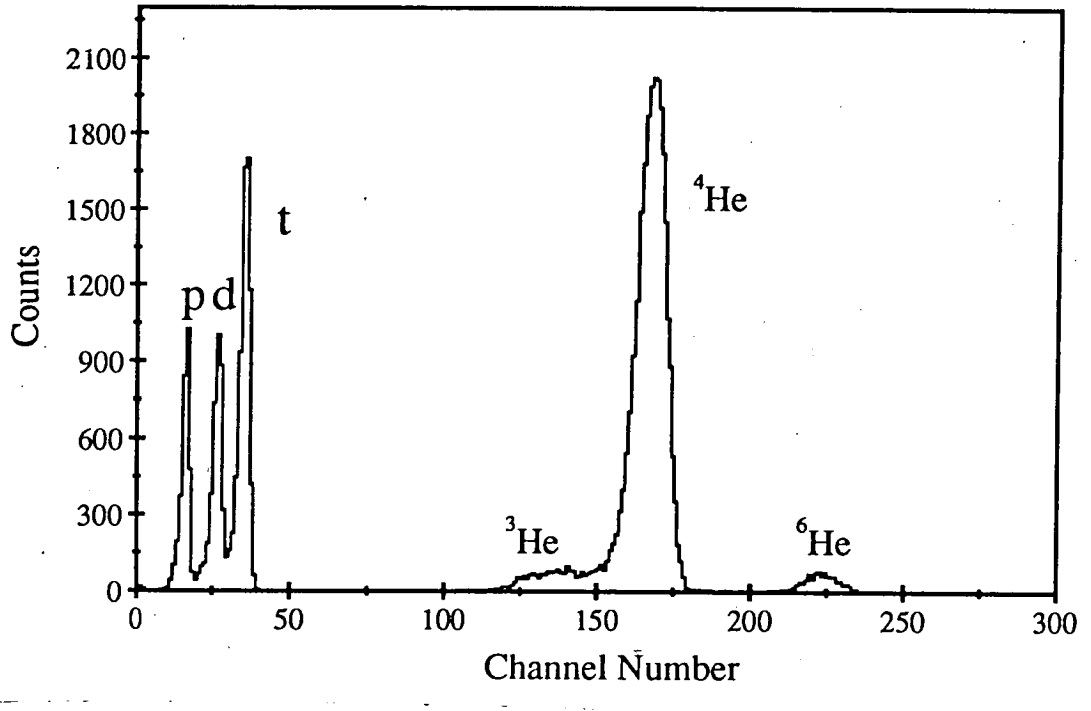

Figure 3.12: *The top PI spectrum is for the telescope containing the Enertec Si(Li), the bottom one is for a telescope containing a Berkeley Si(Li).*

peaks appeared in the same channel. This problem was not encountered for d, α coincidences where the range of the ds was less than the range of the ts in α, t coincidences, which suggests that the effective thickness of the Si(Li)s was not as great as previous tests with electrons had implied. It is possible that in the period intervening between the tests and the experiment the Li had begun to drift out. This would result in the most penetrating t particles registering an energy lower than their actual energy. The discrepancy though was very small, a maximum of less than 0.4 MeV. This problem did not have any affect on the results because it was possible to line up the sequential peaks for one of the particles and use these spectra to obtain the analysing powers.

3.7 Polarimeter

Beam polarization is determined by using a polarimeter. The one used was positioned at 0° as shown in figure 3.8. It acted both as a detection system and as a Faraday cup. The detection system consisted of a H impregnated Ti target and a single detector at 0°. A Ta beam stop placed between the two, stopped the beam. A negative suppression voltage of −300V was applied to prevent the escape of electrons. The charge incident on the collimator and the beam stop was summed and fed into a Brookhaven Current Integrator (BCI). The reaction that takes place and the determination of the beam polarization are described in section 5.1.

3.8 Data Acquisition Hardware

3.8.1 Electronics

The electronics used in the data acquisition basically consisted of three independent sections. One for the polarimeter and one each for the telescope pairs. Simplified circuit diagrams are shown in figures 3.13, 3.14 and 3.15. In figure 3.13 dashed connections represent connections that were only used whilst setting up

the timing in the circuit. All the abbreviations denoting particular electronic units are given below except for INV which represents an EC683 unit which inverts a positive input, PS which represents a prescaling unit and G&D which represents a gate and delay generator unit.

Each telescope circuit provided logic signals for telescope events and for coincidences between the two telescopes on each arm. A telescope event consisted of the presence of signals from the ΔE and E detectors and the absence of signals from the veto detector and the pile up circuit. The pile up circuit produced a signal if the ΔE detector produced two outputs within a specified length of time (4μs).

All the signals from the detectors were fed into Cooknell charge sensitive preamplifiers. These also served as vehicles through which bias was applied to the Si(Li) detectors, the strip detectors had bias applied through a voltage divider box. Both the fast timing and the energy outputs of the preamplifiers were used. In figure 3.13 the Cooknell preamplifiers to which the ΔE detectors were connected are represented by a dashed box containing preamp symbols labeled FPA and PA. The purpose of this is to illustrate the use of both the energy and fast timing outputs of these units they were in no way different to the other preamplifiers used. The following considers the circuit for one telescope between its preamplifiers and the relevant coincidence unit (COINC).

The energy output of the ΔE preamplifier was fed into a timing filter amplifier (TFA) and an amplifier (AMP). The TFA output was converted into a fast timing signal by using a leading edge discriminator (LED) and fed into a pile up inspect unit (PUI) with a 4μs inspect time and an 8μs inhibit time. The amplifier produces bipolar and unipolar output signals. The unipolar outputs for the ΔE and the E were fed into analogue to digital converters (ADC). The bipolar outputs for all the detectors in the telescope were converted into logic pulses by timing single channel analysers (TSCA). All these logic pulses plus the inhibit signal from the pile up circuit were fed into a coincidence unit. An output from this unit was produced if the ΔE and E signals were the only ones present. This output served

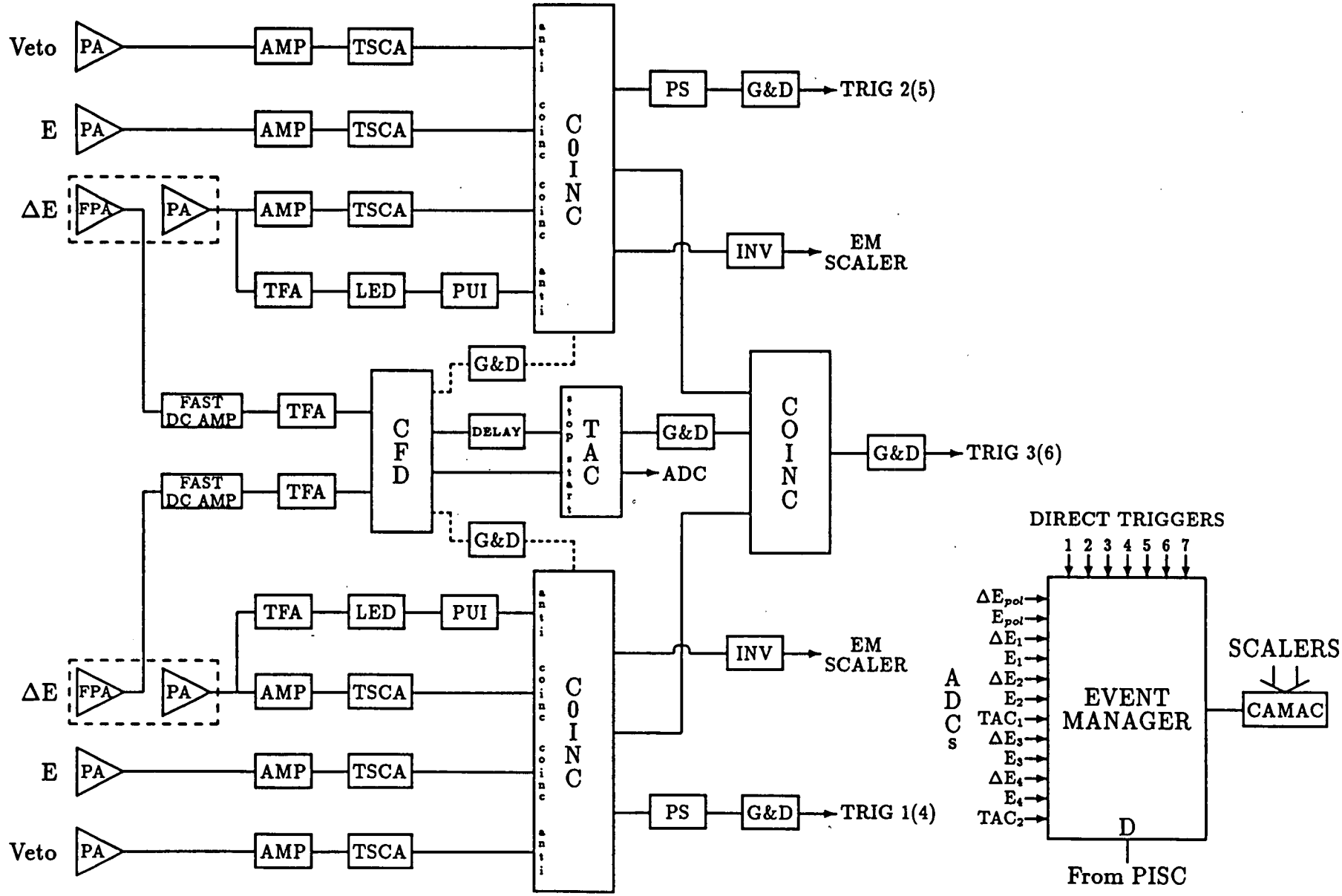

Figure 3.13: Diagram showing the circuit used for one telescope pair and the inputs to the Event Manager. Identical set ups were used for both telescope pairs.

three purposes, it was a condition for a coincidence between two telescopes on one arm, an input to an event manager scaler and an event manager trigger.

The fast timing outputs of the preamplifiers for the ΔEs were fed into fixed gain Cooknell DC amplifiers in the experimental area. The $\times 10$ outputs of these units were then sent to the control room via timing cables which minimized degradation of the signal rise time. The signals were amplified by TFAs and constant fraction discriminators (CFD) were used to provide appropriate signals for use as stop and start inputs for a time to amplitude converter (TAC). The purpose of the TAC was to determine fast coincidences and hence allow differentiation between real and random coincidences. In real coincidences the breakup particles arrive at the detectors simultaneously. The analogue output of the TAC was sent to an ADC and the logical output was used as a condition for a coincidence between the two telescopes.

The inputs to the coincidence unit that defined a coincidence between the two telescopes consisted of the above TAC input and the outputs from the coincidence units that define a telescope event. The output of this unit provided an event manager trigger. The electronics was the same for each telescope pair hence a total of six triggers were produced by this part of the circuit, four singles and two coincidence ones. A seventh trigger was provided by the polarimeter section. Only one detector was used in the polarimeter and the simple circuit used is shown in figure 3.14.

During this experiment the polarization of the beam was continually changed by switching between the phases A and B. This changing of phase was controlled by a unit built at Daresbury known as the Polarized Ion Source Controller (PISC). The configuration in which the PISC was used is shown in figure 3.15. This unit caused the ion source to switch phase every few seconds after a fixed amount of charge was recorded by the Brookhaven Current Integrator (BCI). Three signals were sent to the ion source. Two were used as a binary signal to indicate the phase and the third, labeled "Dead" in figure 3.15, told the source when the PISC was inhibiting the Event Manager to allow time for the source to change phase.

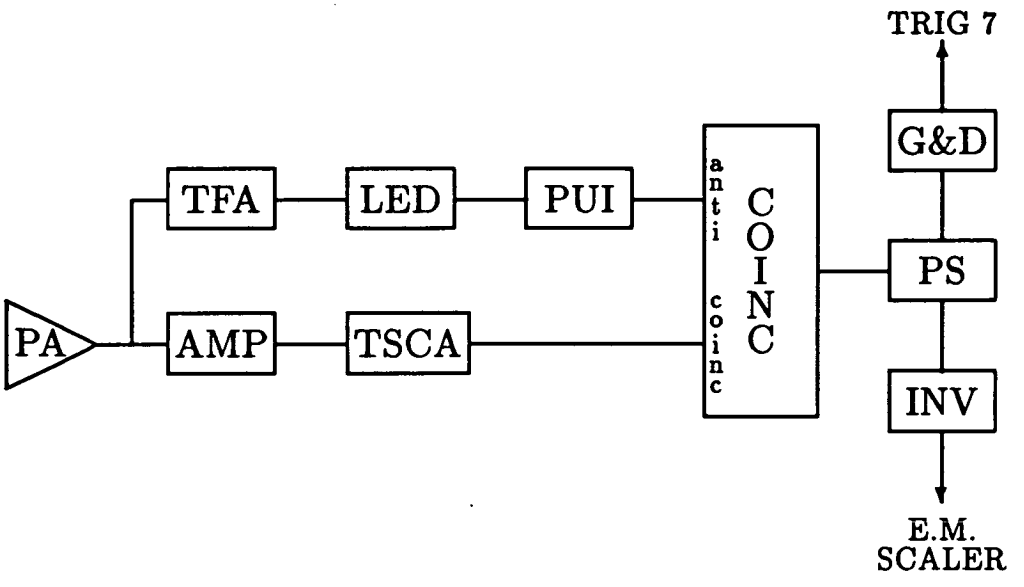

Figure 3.14: *Diagram of circuit used for polarimeter.*

The BCI gives out a pulse every time a certain specified charge is reached. This is done so that if for any reason the overall efficiency of the source should alter it is likely to be the same in both phases and would not therefore cause any errors. This unit also performed three other functions. The first of these was to send signals to the interrupt register which caused bits that specified the phase to be added to the digital outputs of the ADC's, thus enabling the identification of the beam phase for each recorded event. The second was to generate a signal that was used to inhibit the event manager. This signal was present whilst the PISC was instituting a change of phase and while it was halted. The third function of the PISC was to generate levels whilst in a particular phase. These levels were used to gate Camac scalers counting BCI counts and thus the number of BCIs per phase were recorded. Any malfunction of the PISC could thus easily be spotted online. The Camac scalers also recorded the total number of BCI counts and the number of pile up and prescaled telescope events per telescope.

In order to enable the calculation of dead times pulser events were generated. The BCI pulses were prescaled and used to trigger a pulser which injected a pulse into all the ΔE and E preamplifiers simultaneously. This simulated a coincidence

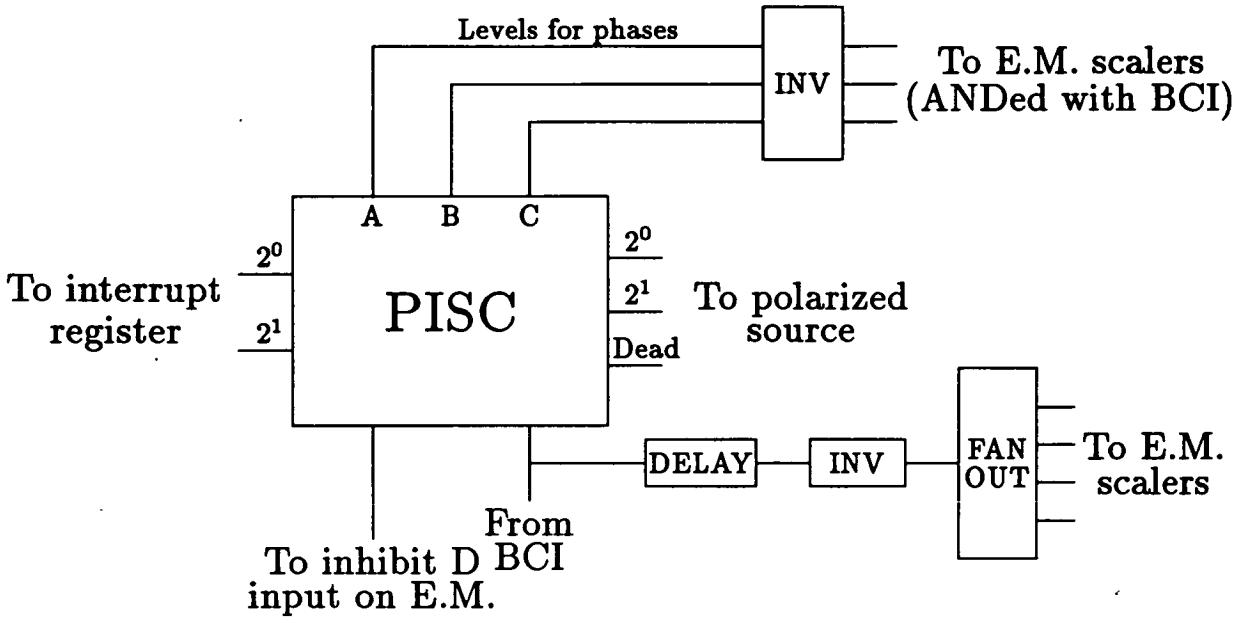

Figure 3.15: *Circuit diagram showing the configuration in which the PISC was used.*

event and hence the dead time for coincidences could be calculated.

3.8.2 The Event Manager

The Event Manager (EM) is the interface between the electronics and the computers. It can be programmed using software to respond in a predetermined way upon the receipt of triggers. In this experiment seven direct triggers were used. Receipt of one of these triggers directed the EM to read particular ADCs. Receipt of a trigger that indicated a coincidence between two telescopes would veto the triggers that indicated relevant telescope events to prevent attempts to read ADCs twice.

3.8.3 Computers

There are three GEC 4000 computers that are used to run any experiment at the NSF at Daresbury. These are known as the A (accumulation) R (resources)

and C (control) machines. A diagram illustrating their connections is shown in figure 3.16. The A machine interacts directly with the Event Manager and the data collection program supplied by the user is run on this computer. This code initially sets up the EM i.e. defines the ADCs associated with particular triggers and defines the online spectra. When the EM multiparameter buffer is full the event by event data is read by the A machine. This data is used to increment the online spectra and is sent to the R machine which writes it to magnetic tape. The C machine is the one with which the user directly interacts. It controls the graphics that display the online spectra.

3.8.4 Software

In order to set up the Event Manager and monitor the data on line a Data Collection Program (DCP) was required. This program was written in the GEC version of FORTRAN66. The data collection subroutines provided by the NSF data acquisition system were used.

The DCP consisted of two main sections, a setting up section and an analysis section. Various "entry points" exist in the code. The parts of the code accessed via these entry points may be entered as required. The entry points comprising the setting up section are usually entered only once whereas the analysis section is entered every time an event is recorded.

In the setting up section the triggers and the ADCs with which they are associated were defined. In this experiment as mentioned in section 3.8.2 direct triggers were used. The size and type of spectra were defined here and space was allocated for them. A separate entry point was used to allow the assignment of values to constants such as gains, offsets, mass gates, energy gates etc. the constants were read from a data base external to the DCP enabling their easy alteration.

In order to allow faster processing of the data online the analysis section of the code was a shorter version of the code finally used to analyse the data. The complete version will be outlined here. The first task of this section was to identify

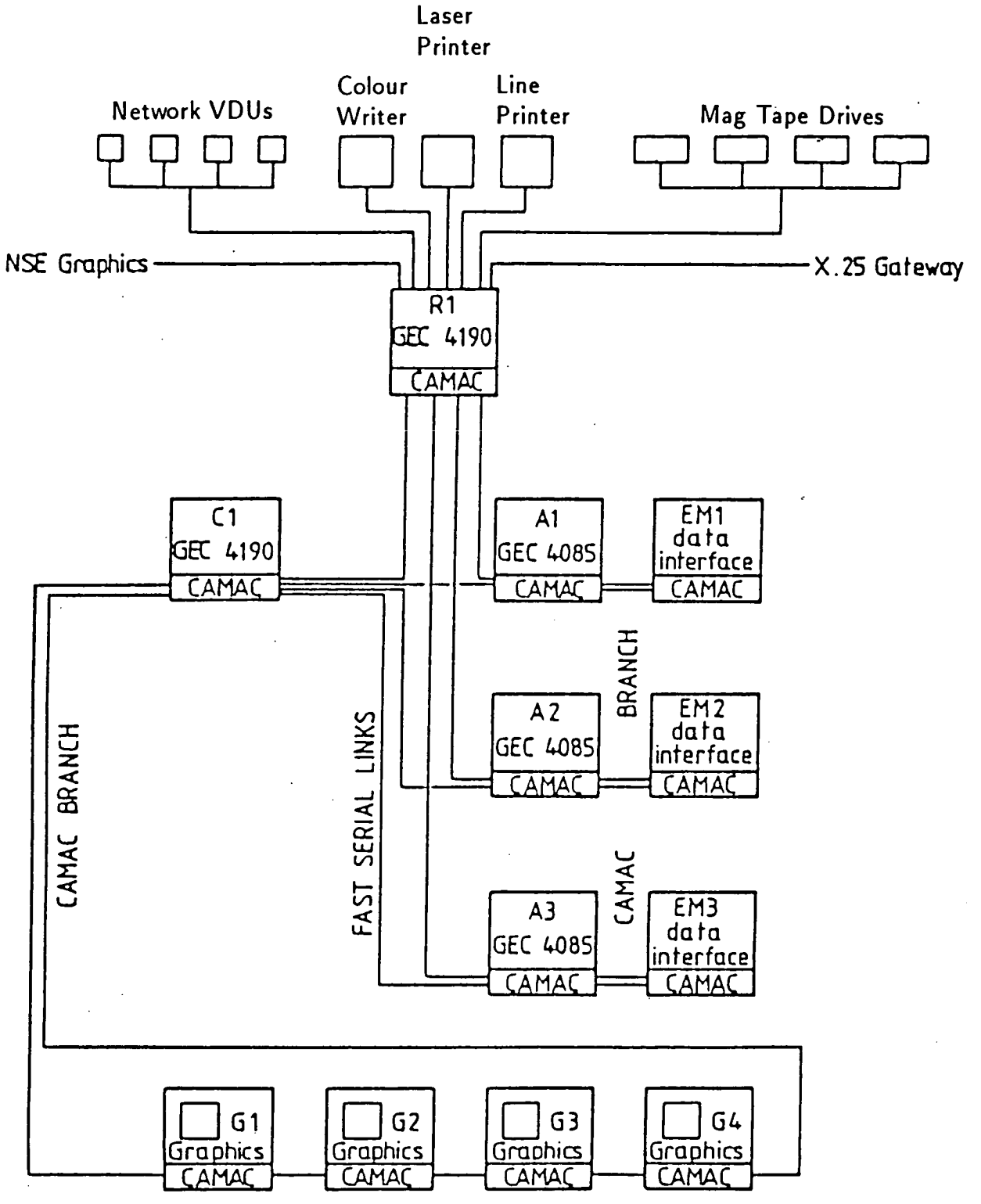

Figure 3.16: *Diagram illustrating the connections between the various computers at the NSF.*

the phase of the beam which was encoded in bits 11 and 12 of the ADC output. In spectra where a knowledge of the phase was required the data were all displayed in the same spectrum, but the spectrum was divided up into three sections. The first 1024 channels containing phase A data the second containing phase B data and the third containing unpolarized data. This last section was only used when the beam was run in three phase.

The analysis section consisted of several subroutines, the particular subroutine accessed depended upon the type of event recorded i.e. a single telescope event or a coincidence event. For singles events only particle identification (PI) spectra and total energy spectra for particular particles were created. The standard mass algorithm [En] was used to create all PI spectra.

$$P.I. \propto TZ^2M \propto (\Delta E + E)^n - E^n \tag{3.6}$$

T target mass

Z proton number

M mass

ΔE energy in ΔE detector

E energy in E detector

n 1.69 in this case

n is a number between about 1.6 and 1.8 which is experimentally determined. It was optimized by creating 2D PI verses energy spectra and chōosing n such that a line parallel to the energy axis appeared on the plot.

If a coincidence trigger was fired then an α, t coincidence was checked for online. Offline α, d and α, α coincidence events were also examined. A real α t event had to satisfy three conditions in the form of gates. Gates on PI spectra selected the desired particles. Both possible permutations e.g. t in top telescope α in bottom or vice versa were checked for. A window on a TAC spectrum ensured that the coincidence was real and not random i.e. that both particles arrived at the detectors at the same time to within the TAC window set. The TAC window was

only properly set offline. Projected energy spectra for both particles, for particular final states of the recoil, were created by placing gates on a spectrum that was the sum of the energies of the particles involved in the coincidence. Offline, relative energy spectra using equation 2.44 were also created.

Dead times were calculated by determining the number of pulser events observed compared to the number known to have been generated by the pulser (see section 3.8.1). The pulse heights were set so as to fall in a convenient place in the P.I. spectra created in the coincidence section. In offline analysis the number of pulses per phase were counted while sorting to ensure that the interrupt register had not become stuck in a particular phase. This problem was encountered during the September run. The offline sorting took place in Edinburgh on a GEC4180 machine.

Chapter 4

The Monte Carlo code

4.1 Introduction

The reactions considered in this thesis result in three body final states. This means that the properties of any detection system which will provide a kinematically complete description of the system are not simply calculable. The reaction can however be simulated by using a Monte Carlo code. The code used was written by Dr. E. Macdonald in C and was run on a Sun Sparc station.

4.2 Description of monte_7Li.c

The reactions simulated by the Monte Carlo code are of the form $^{120}Sn(^{7}Li, Y^{*} \rightarrow \alpha + x)$ where Y is the intermediate nucleus and x is a fragment. The reaction is treated as a two step process.

$$\text{Step 1} \quad {}^{120}Sn + {}^{7}Li \longrightarrow {}^{A}_{Z}Y^{*} + {}^{127-A}_{53-Z}R$$

$$\text{Step 2} \quad {}^{A}_{Z}Y^{*} \longrightarrow \alpha + {}^{A-4}_{Z-2}x$$

Both sequential and direct reactions can be treated as occuring via the above two stage process. For sequential breakup the states of Y^{*} are simulated by assuming they have lorentzian line shapes. In a direct breakup process Y does not exist, but it is kinematically convenient to treat the reaction as a two stage process.

The effective excitation of Y can be found by using the Coulomb calculation described in section 2.7 to determine $d\sigma(\theta,\varepsilon)/d\Omega d\varepsilon$. This distribution can then be used in the Monte Carlo code to weight the random selection of a relative energy in the breakup simulation. Figure 4.1 shows the functions that were used in the simulations.

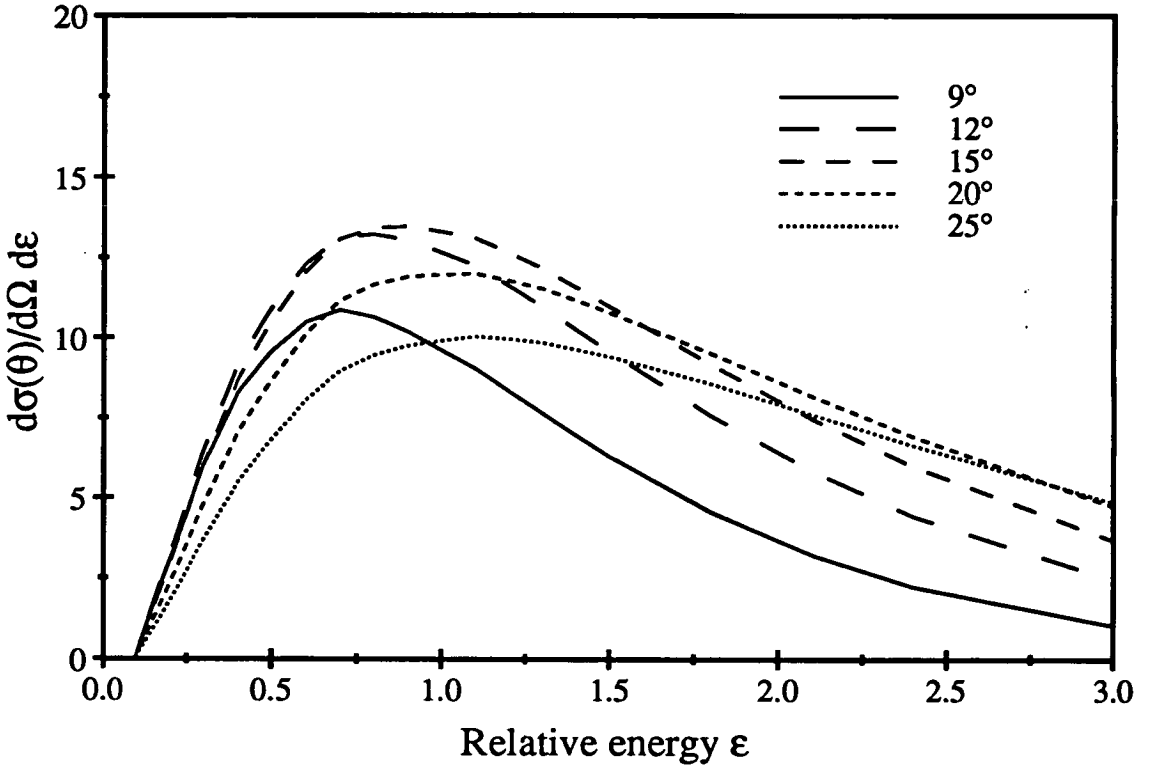

Figure 4.1: *A plot of the population functions used to simulate direct breakup in the Monte Carlo code monte_7Li.c.*

The Monte Carlo code consists of four main operations. The first operation is the excitation of the ejectile Y. Y is then thrown isotropically in the centre of mass system. The actual solid angle into which Y is thrown is not 4π, but a smaller angle whose limits are just larger than the maximum θ and ϕ coordinates that results in fragment detection. This is done to reduce running time. After this the ejectile is broken up, a random direction being selected in the rest frame of the ejectile. Finally the simultaneous detection of the fragments is checked for.

A brief outline of the code is given below. The code consists of three sections, a setting up section, the Monte Carlo loop in which the reaction is simulated and an output section which creates the relevant spectra and gives the number of detected particles.

Setting Up

- The following variables are specified:-
  - Relevant masses, beam energy and relevant Q values.
  - Detection system parameters.
  - Number of tries of reaction.
  - Solid angle into which ejectile thrown.
- Excitation function of ejectile selected.
- Spectra cleared.
- Counting variables zeroed.

Monte Carlo Loop

- Ejectile excited (step 1).
- Ejectile velocity determined.
- Ejectile isotropically thrown in centre of mass.
- Ejectile broken up (step 2).
- Velocities of fragments in ejectile rest frame determined.
- Laboratory velocities and energies of fragments determined.
- Fragment detection ascertained.
- Maximum and minimum angles of ejectile for detected events determined.

Output

- Excitation energy, summed energy and projected energy spectra created.
- Number of detected events.
- Maximum and minimum detection angles.

4.3 Applications of the Monte Carlo code

This code was used in the design of the detection system used in the experiment which forms the subject of this thesis. Data was required at the minimum practicable angle. The physical constraints of the detector mounts meant that the angle chosen also dictated the distance at which the detectors had to be placed from the target. The code was used to determine the expected count rates at various distances enabling the selection of the best distance at which to place detectors to obtain data at small angles and reasonable count rates.

The code was also used to determine all the solid angles used to calculate the cross sections in chapter 5. A valuable method of determining the origin of data is to model a reaction using a Monte Carlo code and compare the resulting spectra with the detected ones. This code was used in just such a manner and the spectra so determined are shown in chapter 5. All the simulations shown in that chapter were produced by this code.

Chapter 5

Data Analysis and Results

The data obtained from the breakup of polarized ^7Li on ^{120}Sn is discussed in this chapter. The first two sections deal with the determination of the polarization of the ^7Li beam using the polarimeter described in chapter 3. The results of the preliminary run performed in November '88 are presented in section two. This run established that a high degree of polarization was obtainable and that the orientation of the polarization axis at the target had been correctly predicted. The next three sections in conjunction with section 3.8.4 deal with the analysis procedure followed. The final part of the chapter discusses the data obtained on the various breakup reactions that occured.

5.1 Determination of Beam Polarization

The polarimeter is described in section 3.7. In order to determine the polarization of the beam the yield of a reaction, the analysing powers of which are known, must be measured. The reaction used in this experiment was $^1H(^7Li, \alpha)$. An example of a polarimeter spectrum obtained during the final data collection run is shown in figure 5.1. As described in section 3.7 the detection system was at 0° giving it both rotational symmetry about the z axis and reflection symmetry in any plane containing the z axis. As the relevant reaction is a parity conserving one these symmetries mean that some T_{KQ} are zero.

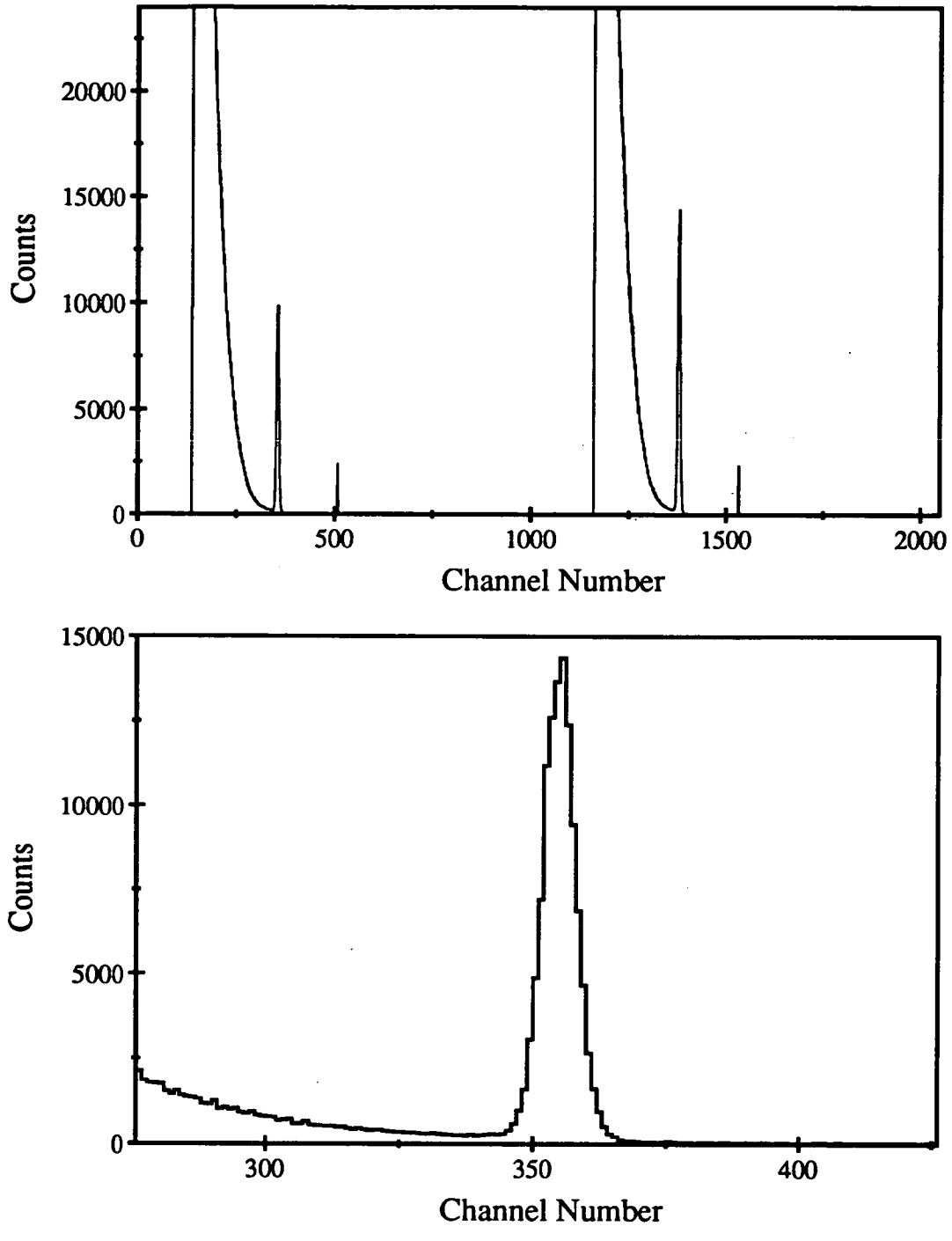

Figure 5.1: *The top figure shows a polarimeter energy spectrum. (Polarization symmetry axis in the y direction in the helicity frame.) The α peak of interest is clearly distinguished from the background and the yield is obviously different in the two phases. The magnitude of the background relative to the α peak can be more clearly seen in the lower figure which is merely a blow up of one of the peaks in the top figure. The small peak in the top spectrum is just a pulser peak.*

$$\begin{aligned} T_{K0} &= 0 \qquad \text{odd } K \quad \text{(reflection)} \\ T_{KQ} &= 0 \qquad Q \neq 0 \quad \text{(rotation)} \end{aligned} \tag{5.1}$$

In this case therefore the only non-zero analysing power is T_{20}.

The fact that the detector is at 0° also results in only the $m = \pm\frac{1}{2}$ magnetic substates being able to participate in the reaction. This constraint is a result of angular momentum conservation and is independent of energy. If these values of the magnetic substates are substituted into equation 2.18 then T_{20} is found to be -1 [Zu79].

The yield in the two polarized phases of the beam is therefore given by

$$Y_{\pm} = Y_0(1 \mp t'_{20}) \tag{5.2}$$

where t_{20} is the polarization and Y_0 is the unpolarized yield.

The polarization of the separate phases can therefore be determined if the yields Y_+, Y_- and Y_0 are known. The determination of all these yields requires the beam to be run in a three phase mode i.e. two polarized phases and one unpolarized one. The polarizations of the two polarized phases though should have equal absolute magnitudes. When this is so the beam polarization can be determined if the beam is run in two phase where both phases are polarized. The polarization that was achieved in the main data collection run is shown in figure 5.2. During the experiment the polarization axis was in the y direction in the helicity frame. This orientation of the polarization axis relative to the polarimeter detection system means that the maximum possible measurable polarization is 0.25 (see section 2.3). It can be seen from figure 5.2 that throughout the run the polarizations remained at about 80% of the theoretical maximum.

The advantage of this mode of running over three phase running is the greater number of relevant counts that can be accumulated over a given time. The disadvantage is that if a fault occurs involving the rf transitions in the source the particular phase at fault is not immediately known. A fault would manifest itself as a reduction in the polarization measured. This was one of the reasons that the

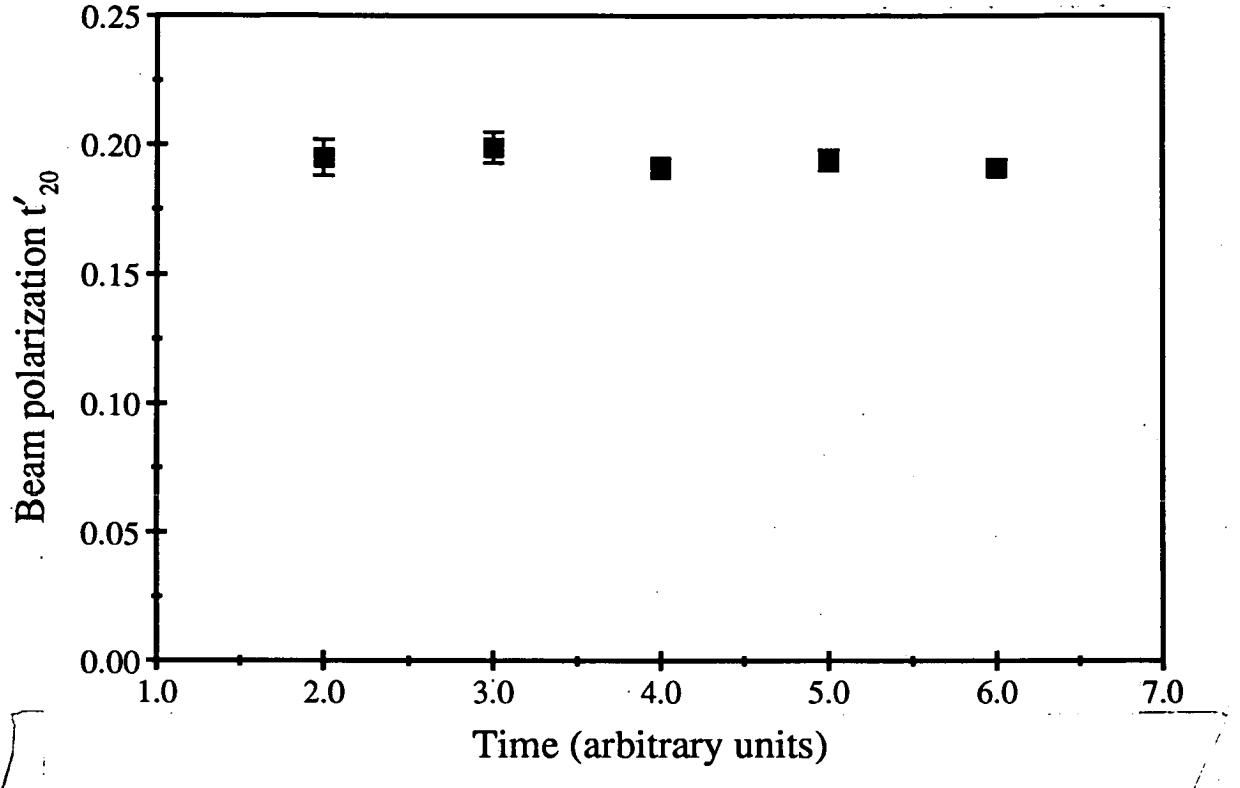

Figure 5.2: *Beam polarization measured by the polarimeter at 0°. The polarization symmetry axis lay in the y direction in the helicity frame. (The error bars on the 15°, 20° and 25° data points lie within the symbols.)*

beam polarization was constantly monitored throughout the run. In the preliminary run described in the next section the beam was run in three phase. Faults in the rf transitions were encountered during this run. For the main data collection run the beam was run in two phase and no rf transition faults occured.

The detector in the polarimeter obviously subtends a finite solid angle at the target so that the whole of its surface is not exactly at zero degrees. The constraint on the magnetic substate population is therefore not rigidly true over the whole surface. The analysing power though is not expected to vary dramatically over this very small angular range ($-1.6°$ to $1.6°$) and the error introduced should be negligible. No calculations or data presently exist on the variation of t_{KQ} about

zero, but a recent run at the NSF at Daresbury used a psd in the polarimeter. The results of the run are not yet available however.

5.2 The Wien Filter Curve

In November '88 a preliminary run for the experiment discussed in this thesis took place. This run was the first use of a polarized ^7Li beam at the NSF at the S.E.R.C.'s Daresbury Laboratory. The primary purpose of this run was to ensure that the polarized source was functioning properly and that the orientation of the polarization axis on target was as predicted.

The orientation of the polarization symmetry axis in the source can be altered using the Wien filter. On its way to the target the axis passes through various magnetic fields and undergoes precession. This precession is calculable and hence a particular Wien filter setting should result in a known orientation of the polarization axis on target. In order to check that this was so, data was taken at various Wien filter settings and the Helicity frame polarization determined. The beam was run in a three phase mode which allowed the independent determination of the polarization in the two polarized phases. This was done to ensure that they had the same magnitudes.

The polarizations are calculated using the relation given in equation 5.2. The values of the t_{20} determined at the various polarization symmetry axis orientations should be given by

$$t'_{20} = D^{(2)}_{00}(\alpha, \beta, \gamma) t_{20} \tag{5.3}$$

where t_{20} is the polarization when the polarization symmetry axis lies along the z axis.

The detection system is symmetric about the z axis therefore α and γ rotations have no affect and can be set to zero. The resulting $d^{(2)}_{00}$ rotation function has the form

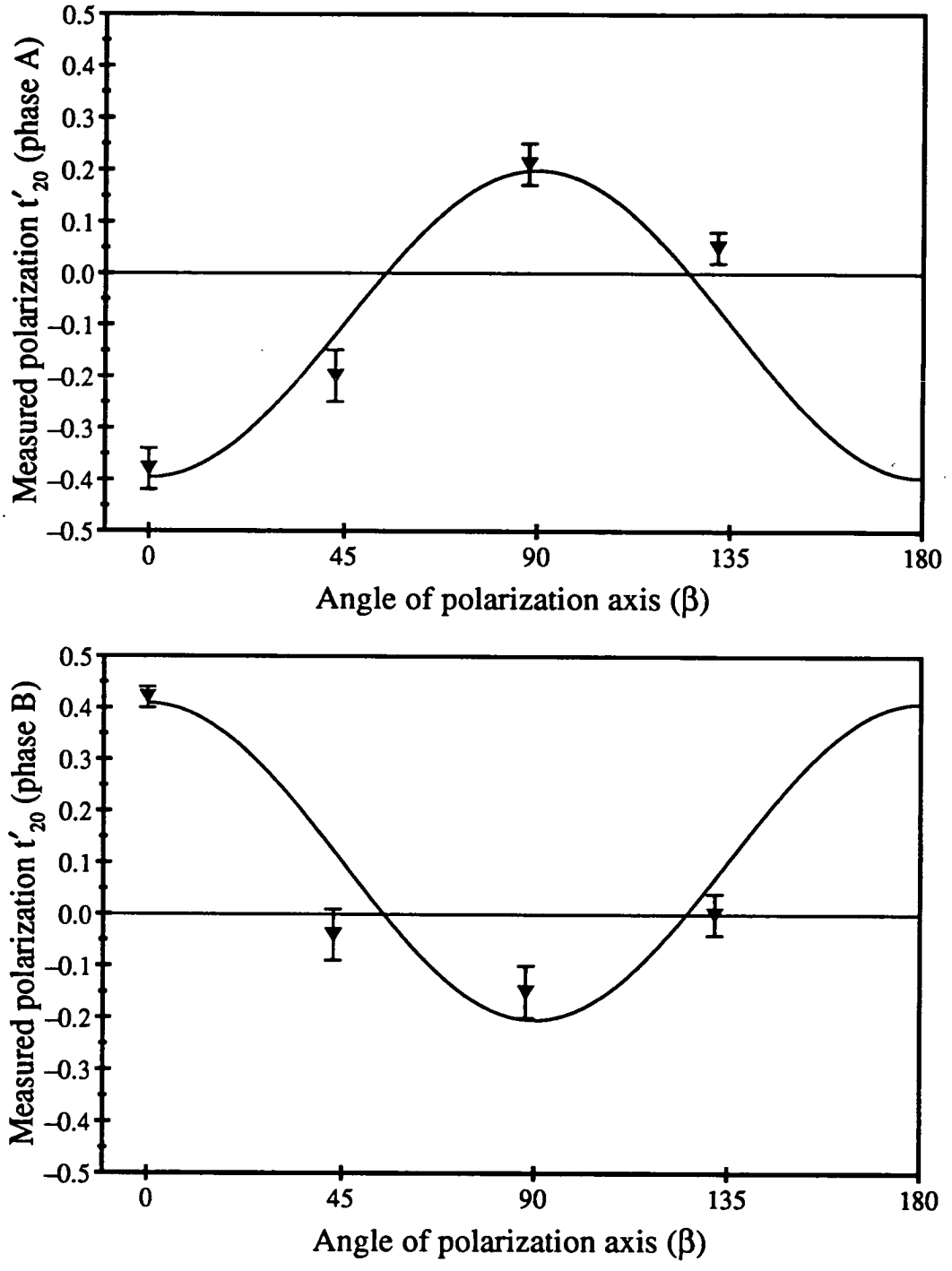

Figure 5.3: *Measured polarizations for various orientations of the polarization symmetry axis to the beam axis for the two polarized phases of the source*

$$d_{00}^{(2)}(\beta) = \frac{1}{2}(3\cos^2\beta - 1) \tag{5.4}$$

The values of t'_{20} measured should fit this curve. The data points were found to fit this curve well. The plots in figure 5.3 show the curves fitted to the data points using a weighted least squares fit. The maximum values measured were, $t_{20} = -0.38 \pm 0.04$ and $t_{20} = 0.42 \pm 0.02$. These values show that the source was operating at about 80% efficiency. For this run a detector telescope was used in the polarimeter. It was found that the relevant peak was well resolved and had a negligible background without any mass identification. For the main run therefore, which took place in September '89, only one detector was used.

5.3 Analysis Procedure

The sortcode used to analyse the data has already been described in section 3.8.4. A brief outline of the analysis method will therefore be given here along with a description of the final extraction of the data.

The identification of a coincidence event involves the imposition of various conditions until the required event is unambiguously identified. The particle identification gate selects coincidences between the desired particles. This is followed by a TAC gate which only allows real events through i.e. ones where the difference in time between the detection of the particles in question is within a particular time window. The next gate selects a particular excited state in the residual nucleus by setting a gate on the summed energy of the particles in coincidence. Once all these conditions are satisfied the event has been identified and projected energy and relative energy spectra are created.

The required yields can be obtained from either the projected energy spectra or the relative energy spectra though an average θ_{1-2} (see equation 2.43) must be used in the latter case. The relative energy spectrum has certain advantages when considering α, t coincidence data. The determination of yields for the sequential process requires a background subtraction of direct events. It was found to be

easier to fit backgrounds in relative energy spectra because of the larger number of direct counts under the single sequential peak and the smooth background that they form. In projected energy spectra two sequential peaks exist and the direct counts lie in two broad bumps which make fitting a background with the available routines much more difficult. A comparison of the spectra in figures 5.8 and 5.10 illustrates these points. The determination of differential cross sections requires differentiation between direct and sequential events and this was found to be easier when considering relative energy, rather than projected energy spectra. No significant yield of direct events was found for α, d and α, α coincidences therefore relative energy and projected energy spectra could equally well be used to determine the analysing powers and differential cross sections. Relative energy spectra do have one advantage when determining analysing powers in that one is sure that one has not inadvertently used different peak widths on the two solutions in projected energy spectra.

5.4 Analysing Power Determination and Errors

The ${}^{T}T_{20}$ analysing powers were determined using the relation (see section 2.4).

$$ {}^{T}T_{20} = \left(\frac{Y_B - Y_A}{Y_B + Y_A}\right) \frac{1}{|t_{20}|} \tag{5.5} $$

Y_A and Y_B are the total yields in phases A and B and $|t_{20}|$ is twice the magnitude of the measured beam polarization i.e. the beam polarization that would be measured if the polarization symmetry axis were in the z direction in the Helicity frame (see section 2.4).

All errors quoted in this thesis are statistical. This is by far the most important error for analysing powers as most systematic errors cancel out. The only other error that could affect these numbers is a shift of the beam away from the centre of the target. A beam shift in the horizontal plane results in the angles at which the telescope pairs are set being different from one another. This though is largely overcome as, for smoothly varying analysing powers, a reduction in count rate in

one telescope pair will lead to an increase in the other and the determination of ${}^{T}T_{20}$ requires the data on both sides in each phase to be summed. Any vertical offset of the beam would result in different effective solid angles for the two possible permutations of particle detection i.e. particle 1 in the top and particle 2 in the bottom telescopes and vice versa. The effect was investigated by using a Monte Carlo code where the detectors were offset from their central position. Moving the beam by 2mm only caused a difference in effective solid angle for the two cases of about 1%. Any error due to such a drift is therefore likely to be negligible.

The statistical error for ${}^{T}T_{20}$ was calculated from

$$(\Delta {}^{T}T_{20})^2 = \left(\frac{\partial {}^{T}T_{20}}{\partial Y_A}\right)^2 (\delta Y_A)^2 + \left(\frac{\partial {}^{T}T_{20}}{\partial Y_B}\right)^2 (\delta Y_B)^2 + \left(\frac{\partial {}^{T}T_{20}}{\partial t_{20}}\right)^2 (\delta t_{20})^2 \quad (5.6)$$

where δX is the statistical error in X. At all angles the dead times measured in each phase and in each pair of detectors differed by a maximum of 2% therefore for the purposes of error calculations an average dead time for all yields was used. Equations 5.5 and 5.6 then give

$$(\Delta {}^{T}T_{20})^2 = \frac{4C}{t_{20}^2} \frac{Y_A Y_B}{(Y_A + Y_B)^3} + \frac{1}{t_{20}^4} \left(\frac{Y_B - Y_A}{Y_B + Y_A}\right)^2 (\delta t_{20})^2 \quad (5.7)$$

where $C = 1/(\text{average live time})$ Y_A and Y_B are the yields in phases A and B corrected for dead times and $\delta Y_x = C\sqrt{Y_x}$. The error in t_{20} is very small compared to the errors in the yields and in most cases the second term in equation 5.7 is negligible.

When extracting the analysing powers for sequential data when a significant amount of direct data occurs at the same energy the two types of data must be separated. If this "background" exists then additional terms are required and the equation becomes

$$(\Delta {}^{T}T_{20})^2 = \frac{4C}{t_{20}^2} \frac{Y_A Y_B}{(Y_A + Y_B)^3} + \frac{1}{t_{20}^4} \left(\frac{Y_B - Y_A}{Y_B + Y_A}\right)^2 (\delta t_{20})^2$$

$$+ \frac{4C}{t_{20}^2}\left(\frac{C(Y_B^2(\delta b_A)^2 + Y_A^2(\delta b_B)^2)}{(Y_B+Y_A)^4} + \frac{Y_A^2 b_B + Y_B^2 b_A}{(Y_B+Y_A)^4}\right) \quad (5.8)$$

The yields in the equation are now the total yields minus the backgrounds all corrected for dead times. b_A and b_B are the backgrounds corrected for dead times and δb_A and δb_B are the errors in the backgrounds excluding any corrections due to dead times. These errors were estimated by considering the range of fits to the background that appeared plausible. The data that corresponds to the sequential breakup of ^7Li into an α and a t is the only data that possesses a significant background. The increase in the error due to the extra terms in the above equation is of the order of 10%.

5.5 Differential Cross section Determination

From equation 2.15 it can be seen that the sum of all the data from both telescope pairs gives the yield that would have resulted had the beam been unpolarized i.e.

$$Y_A + Y_B = 2Y_0 \quad (5.9)$$

where Y_0 is the unpolarized yield in one telescope pair that would have been obtained had the experiment been run for the same total time using an unpolarized beam. It is therefore possible to use this data to obtain differential cross sections as well as analysing powers.

The differential cross section is determined from the relation

$$\frac{d\sigma}{d\Omega} = \frac{N_c}{N_B}\frac{1}{\rho x}\frac{1}{\Delta\Omega} \quad (5.10)$$

N_c Number of coincidences detected per unit time.

N_B Number of beam particles passing through the target per unit time.

ρx Number of particles in the target per unit area.

$\Delta\Omega$ Solid angle.

Using appropriate units the equation becomes

$$\frac{d\sigma}{d\Omega} = \frac{2.66 \times 10^{-7} NZA}{I \Delta\Omega_{eff} f T} \qquad (mb/sr) \qquad (5.11)$$

N Number of coincidences per angular setting.

Z Average beam charge entering Faraday cup ($Z = 3$).

A Atomic mass number of target ($A = 120$).

I Total charge detected in Faraday cup per angular setting (μC).

$\Delta\Omega_{eff}$ The effective solid angle of the system (sr).

f Fractional live time of system.

T Target thickness (mg/cm^2).

The differential cross section errors quoted are all statistical, but differential cross sections are more subject to systematic errors than analysing powers because an absolute number is required rather than a ratio. The fractional live time is determined as described in section 3.8.4. The effective solid angles used in the determination of the differential cross sections were calculated using a Monte Carlo code described in chapter 4. The error in the effective solid angles for sequential breakup is estimated to be $\sim$ 3% from target detector distance errors, but the error in the effective solid angle for direct breakup is greater than this because of the error in the population of the α, t continuum as a function of relative energy which was used in the Monte Carlo code to determine the effective solid angles. The greatest source of systematic error is in the target thickness. For all differential cross sections measured in the experiment described in this thesis the trend was found to be similar to that in previous work by Davinson [Da87], but a constant difference in absolute magnitude was observed of about 25%. A further source of error is in the differentiation between direct and sequential events in α, t coincidences when choosing integral limits.

5.6 Discussion of Data

The coincidence data are presented in this section. These data are from the breakup reactions of polarized ^7Li at an energy of 70MeV on a ^{120}Sn target. The experimental beam polarization is given in section 5.1. Inclusive data produced by this reaction have been extensively discussed in [Da87] and [Yo89]. Examples of the broad featureless beam velocity bumps produced are shown in figure 5.5.

5.6.1 α t Coincidence Data

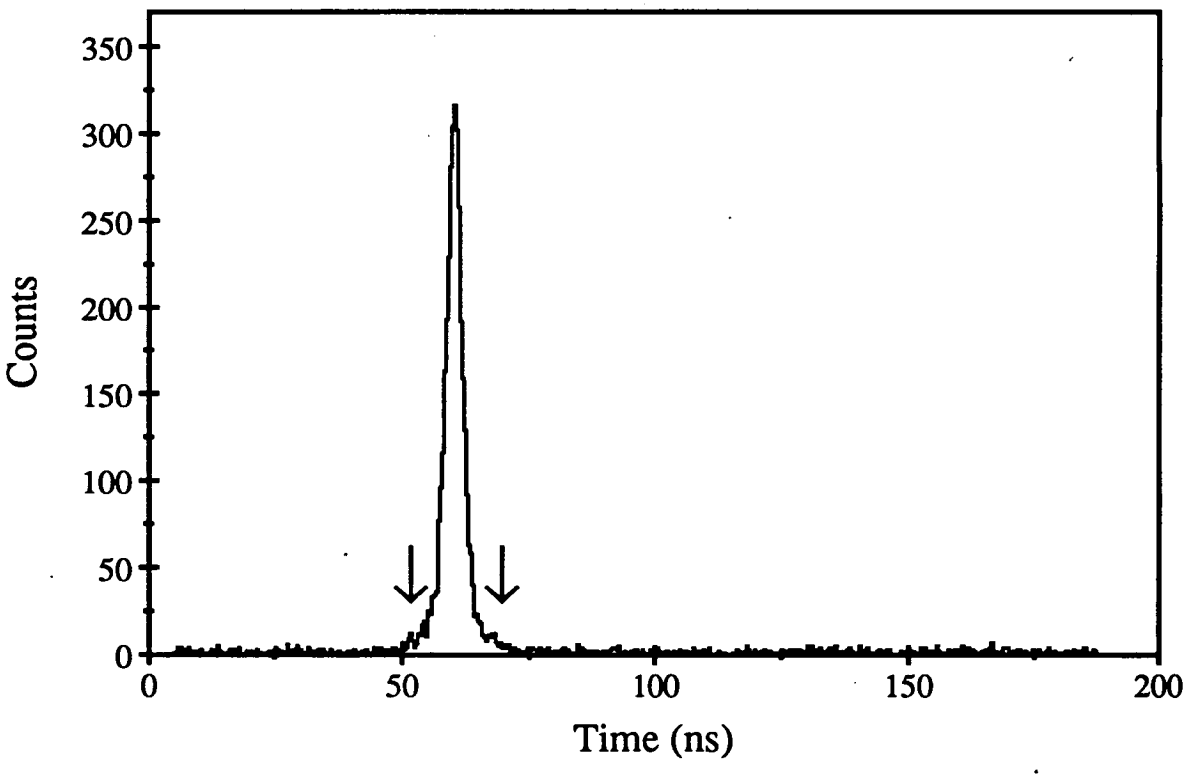

Figure 5.4: *An example of a TAC spectrum produced after the identification of an α, α coincidence. The arrows indicate the 18ns wide gate set on real events.*

These data were obtained by imposing the condition that α and t particles were "simultaneously" detected in one pair of detector telescopes. A description of the detectors and the experimental setup is given in chapter 3. The simultaneous condition is that both particles should arrive within the TAC window imposed.

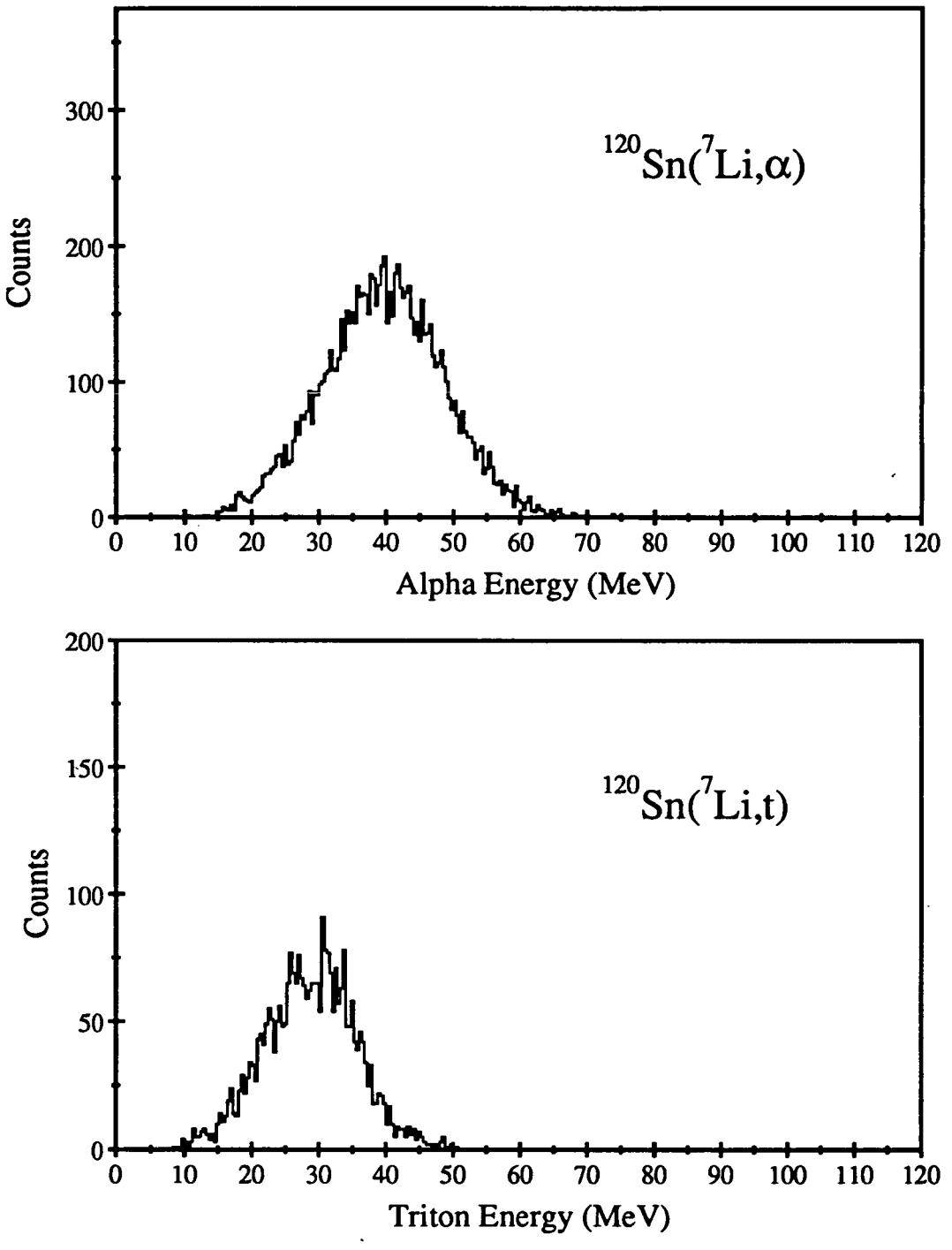

Figure 5.5: *Examples of inclusive spectra produced by the reaction* $^{120}Sn(^{7}Li, X)$ *for a 70MeV beam. The distributions can be seen to be centred at the beam velocity.*

An example of a TAC spectrum produced after particle identification is shown in figure 5.4. No coincidence condition is imposed between the pairs of detector telescopes on either side of the beam. In the following discussion of the data the general properties of the data described refer to effectively unpolarized data obtained by summing all the data as described in section 5.5.

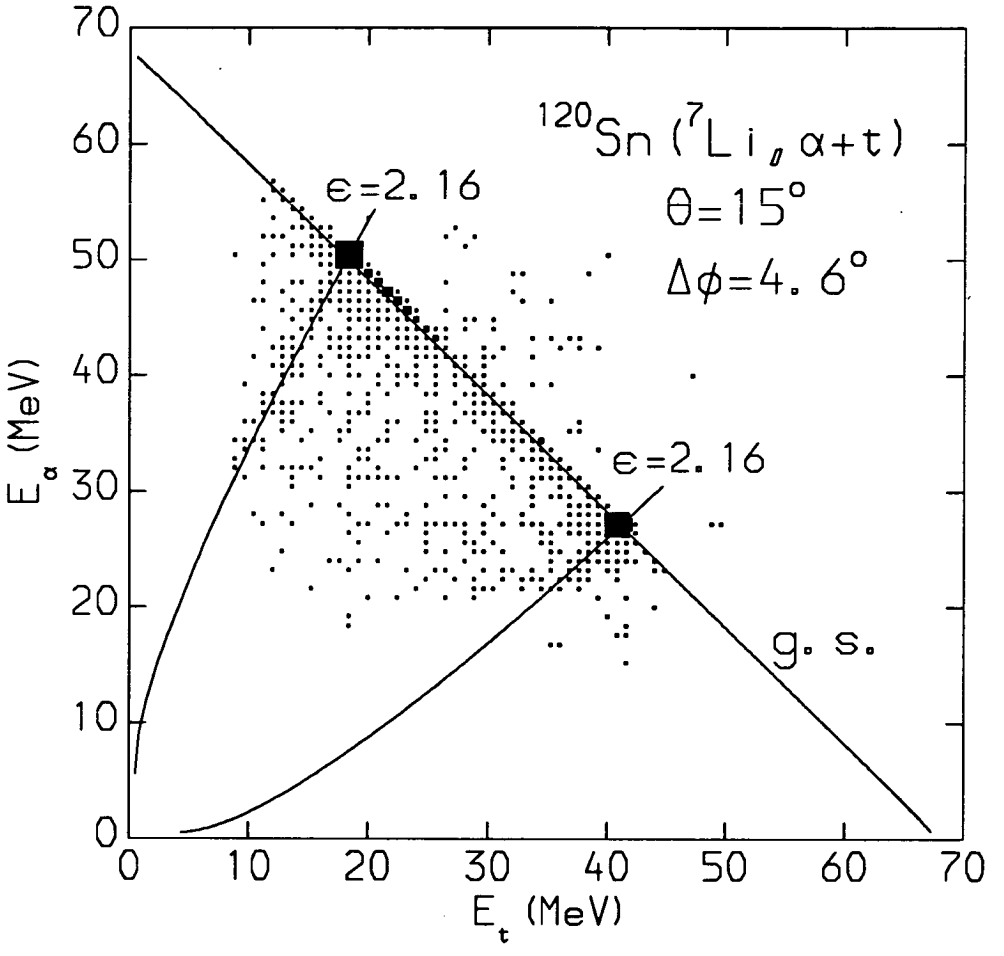

Figure 5.6: *α energy verses t energy for the reaction $^{120}Sn(^7Li, \alpha + t)$, no energy gates were imposed to obtain this spectrum. (The size of the squares is dependent upon the number of counts.)*

A two dimentional plot of the energy of the α particle, E_α verses the energy of the t, E_t is shown in figure 5.6. Also plotted on the figure is the kinematic locus (see equation 2.43) which corresponds to leaving the ^{120}Sn target in its ground state. Most of the data are seen to lie along this curve. The 1D summed energy

spectrum ($E_\alpha + E_t$) in figure 5.7 clearly shows that most of the data corresponds to the ground state of ^{120}Sn. This shows that the α t breakup channel is predominantly elastic. The total energy gate used in sorting the data, as discussed in section 5.3, is shown in this figure.

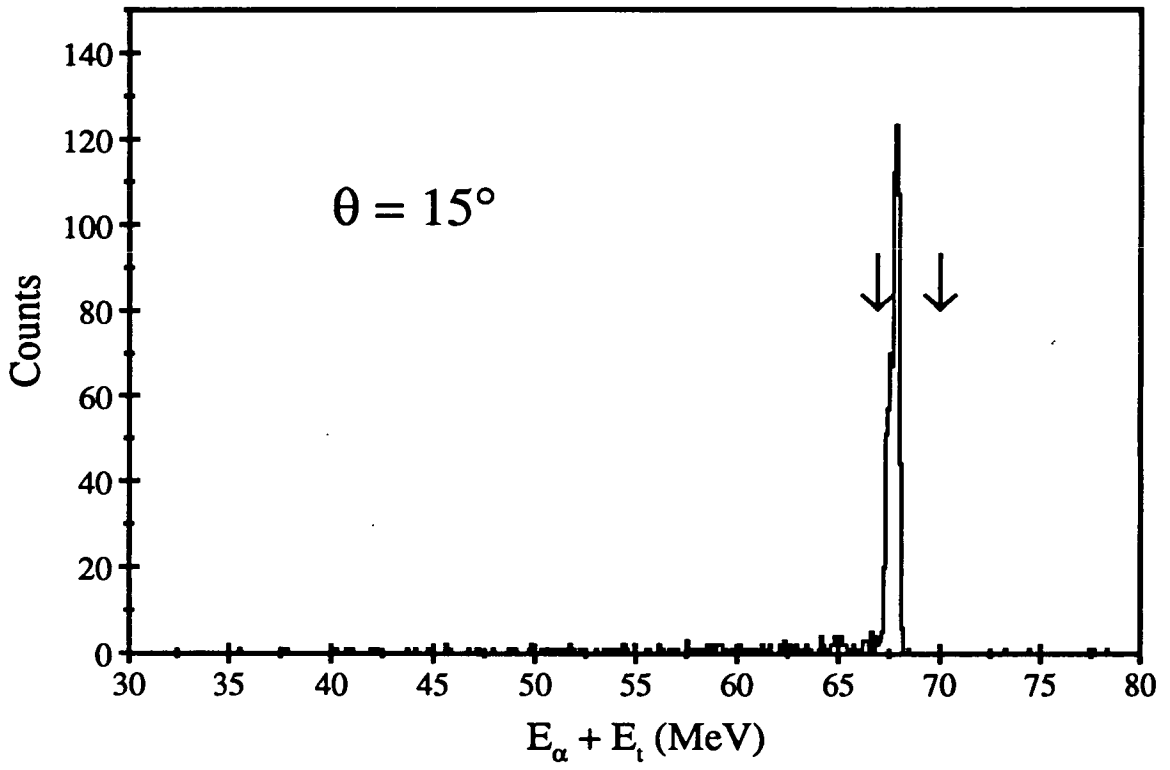

Figure 5.7: *Sum of the α and t energies from the reaction $^{120}Sn(^7Li, \alpha + t)$, for a beam energy of 70MeV. The single peak corresponds to the recoil ^{120}Sn being in its ground state. The arrows around the ground state peak indicated the position of the total energy gate used in subsequent analysis.*

Also plotted in figure 5.6 are the loci corresponding to the relative energy that the α and t would have if they came from the sequential breakup of ^7Li via its 4.63MeV excited state. Enhancements can clearly be seen at the intersections of the kinematic and relative energy loci. There is also though a substantial amount of data that does not correspond to these kinematic solutions. These data do not correspond to sequential breakup via any excited states of ^7Li and are termed direct breakup events. If the data are projected onto either energy axis then a 1D

spectrum is obtained which clearly shows sequential and direct events (see figures 5.8 and 5.9). Comparison of this spectrum with a Monte Carlo simulation of sequential breakup also demonstrates that the events observed between the peaks are not accessible by sequential breakup via the 4.63MeV state of ^7Li. Figure 5.9 shows a Monte Carlo simulation of the direct breakup of ^7Li. A comparison of the data with the Monte Carlo simulation shows that it reproduces the data very well.

In previous work on this reaction using unpolarized beams, [Da87, Sh84], it was found that direct breakup dominated at forward angles and at the furthest forward angle measured, 11.5°, the data was almost entirely direct. This trend was also observed in the present data, but at the furthest forward angle measured here i.e. 9° the sequential peaks were found to reappear in the projected energy spectrum (see figure 5.8). This type of oscillatory behaviour is predicted by the DWBA, adiabatic and CDCC models described in chapter 1.

A further interesting feature revealed by figure 5.8 is the asymmetry of the direct breakup data about the minimum relative energy. This asymmetry was first observed by Shotter et al. [Sh81], in their work on the breakup of ^7Li on a ^{208}Pb target, where they suggested that it may be due to the fragments undergoing final state Coulomb interactions with the target. In such final state interactions the magnitude of the deviation will depend on the charge to mass ratio, Z/M, and the velocity of the particle in question. Particles with low velocities and high charge to mass ratios will suffer the greatest deviation. This simple picture would lead one to expect low energy α particles to suffer most. This would lead to an enhancement of the yield of a coincidence consisting of a high energy α and a low energy t over one consisting of a low energy α and a high energy t. This is clearly observable in figure 5.8 for 15°, 20° and 25°, but the 9° data appears to show the opposite enhancement. The smallest angle at which Shotter et al. obtained data was 13° and for all angles at which they acquired data the asymmetry observed was in the same sense. The data obtained at 9° here however shows a reversal of this asymmetry. This appears to indicate that the distortion cannot simply be

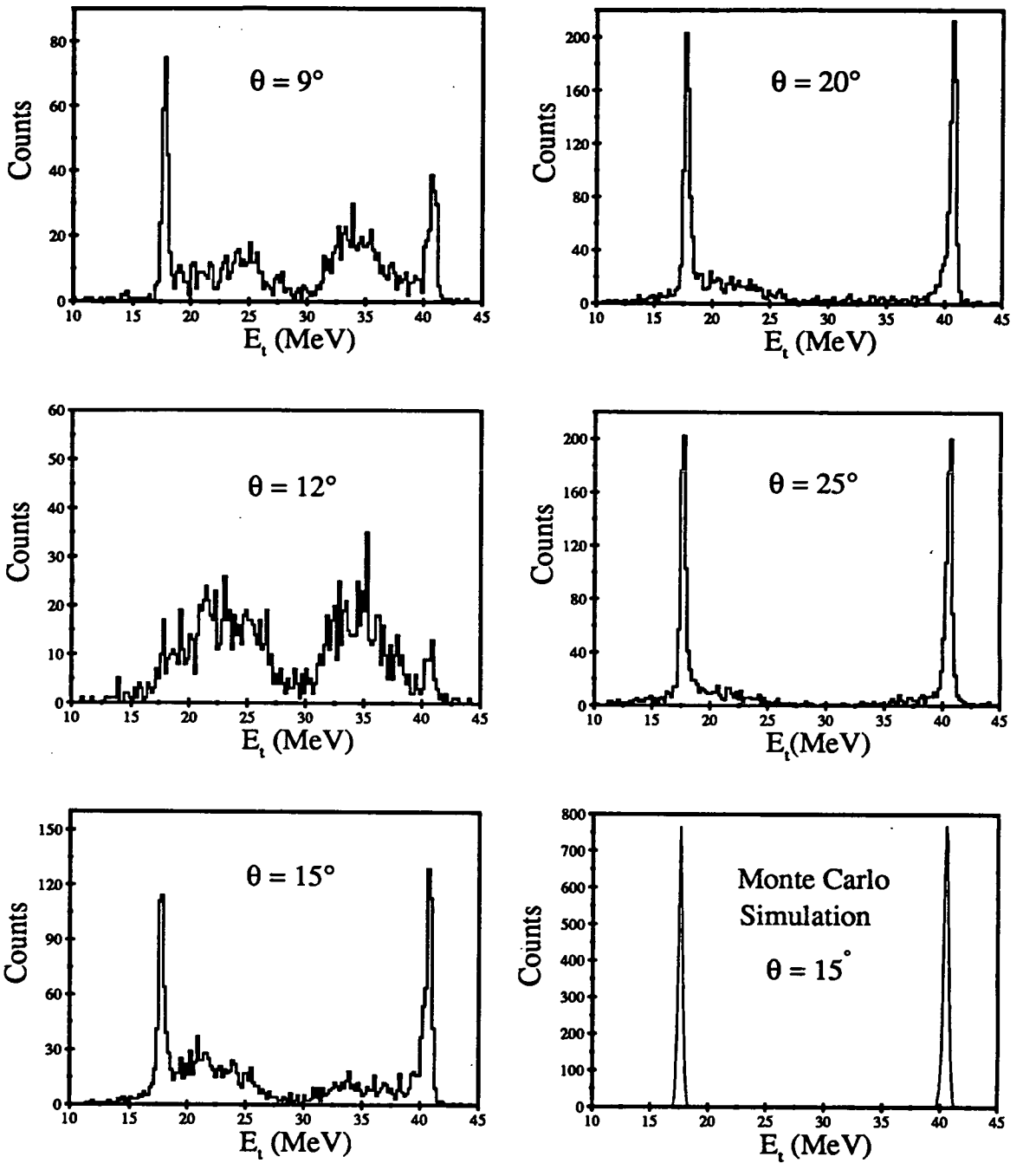

Figure 5.8: *t projected energy spectra for the reaction* $^{120}Sn(^{7}Li, \alpha + t)^{120}Sn_{g.s.}$. *These spectra clearly show the increasing importance of direct breakup at forward angles. The Monte Carlo simulation is for the sequential reaction only. Comparison of this with the t energy spectra clearly illustrates the presents of non-sequential events.*

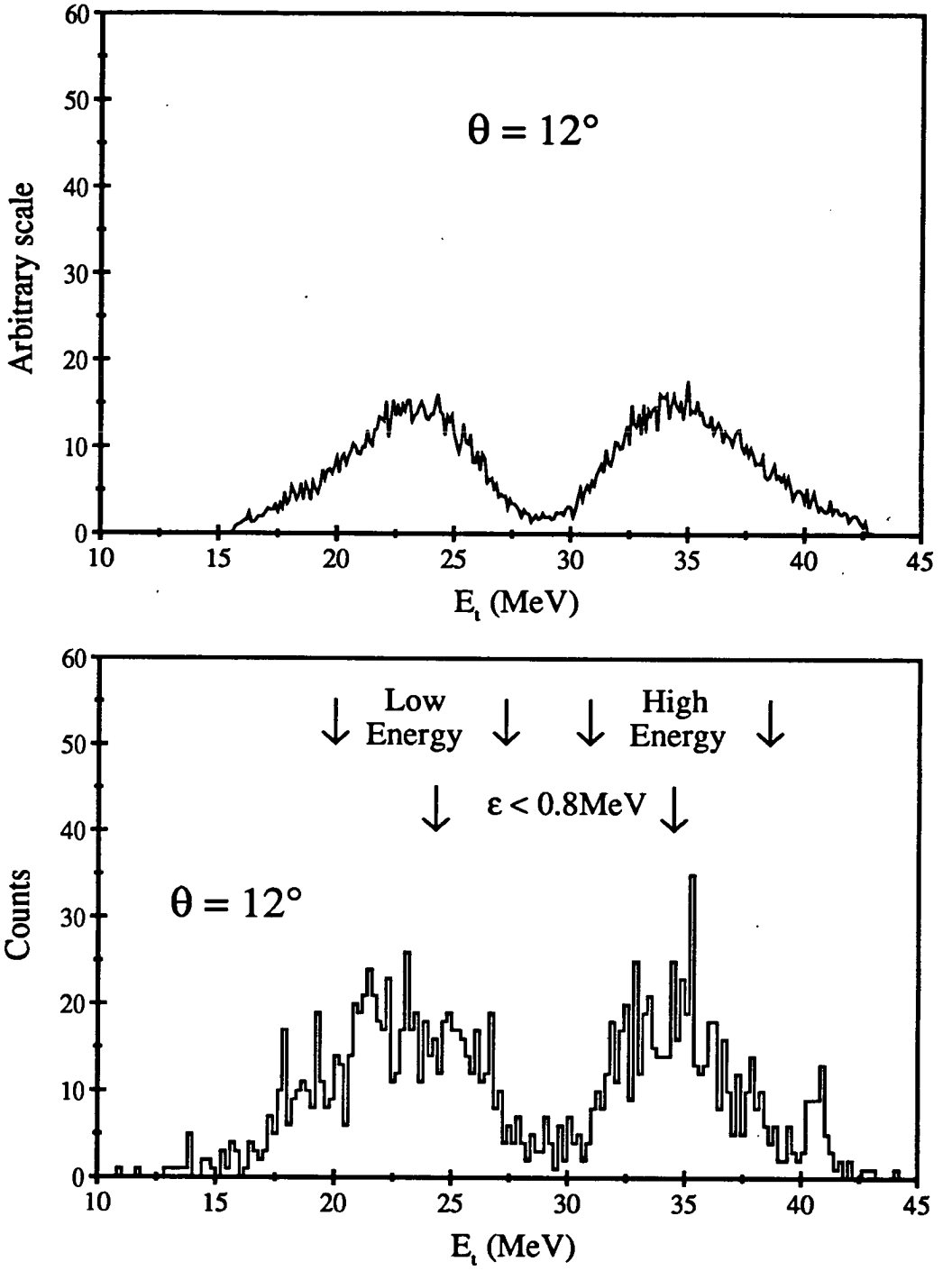

Figure 5.9: *The top figure shows a Monte Carlo simulation of a t projected energy spectrum for the direct breakup element of the reaction* $^{120}Sn(^{7}Li, \alpha + t)^{120}Sn_{g.s.}$. *The lower figure shows an experimental t energy spectrum and shows the gates used in analysis.*

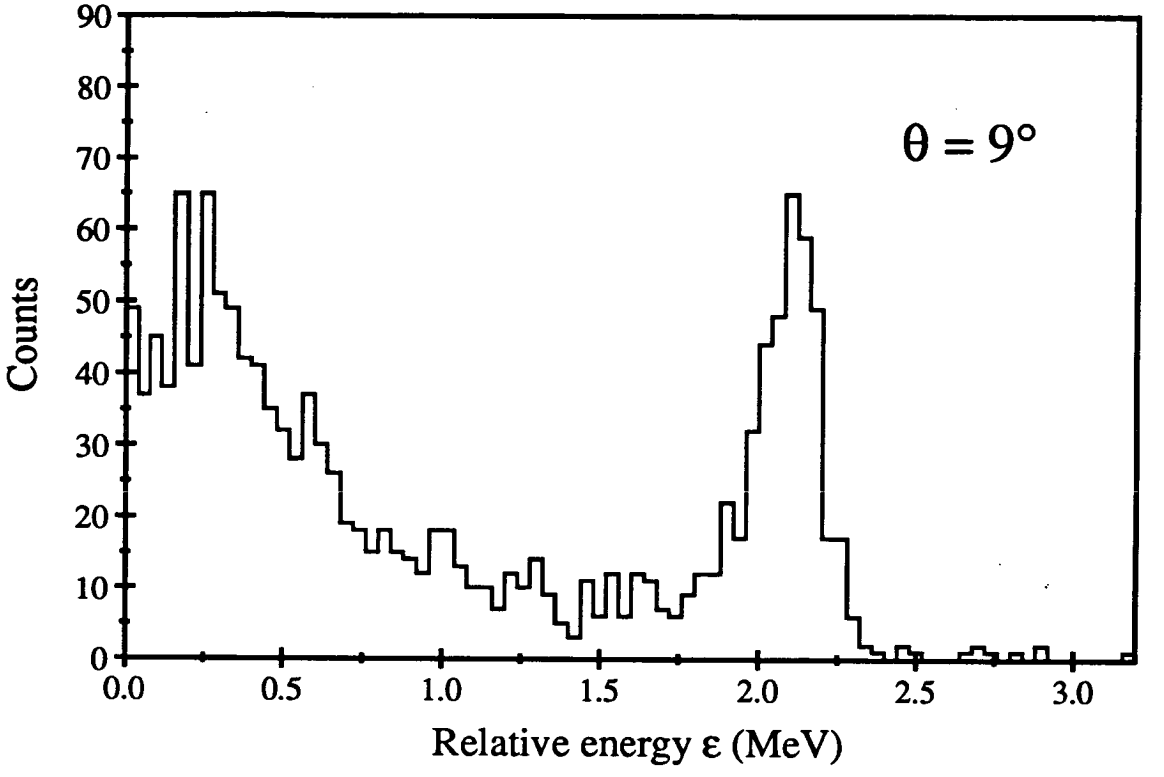

Figure 5.10: *Relative energy spectrum for the reaction* $^{120}Sn(^{7}Li, \alpha + t)^{120}Sn_{g.s}$

explained in terms of Coulomb final state interactions. A Coulomb interaction causing distortion of the momentum distribution in such a way that the yield for the coincidence consisting of a high energy α particle and a low energy t is enhanced, would be expected to have the same consequences at all angles where the Coulomb interaction dominated. A possible reason for this reversal of enhancement is the presence of a nuclear element in the interaction which interferes with the Coulomb part. This interesting feature of the data cannot be accommodated by any of the existing calculations on the direct breakup of ^{7}Li.

Analysing Powers

Previous work [Sh81, Sh84, Da87] which measured differential cross sections has strongly suggested that direct breakup at forward angles is due to the Coulomb interaction. Analysing powers however, possess considerable advantages over differential cross sections. Analysing powers are measurable quantities which are

more sensitive than differential cross sections and can often lead to dramatically different results in cases where the cross sections are similar (see section 2.6). The experiment which forms the subject of this thesis was performed to exploit this property of analysing powers to produce greater insight into the mechanism of the breakup of ^7Li.

In any experiment using polarized beams it is possible to measure several different analysing powers merely by altering the direction of the polarization symmetry axis. Unfortunately however lack of time restricted the measurement to only one analysing power namely $^TT_{20}$. This analysing power was chosen because the semi-classical calculation in section 2.5 predicts a large value which makes a positive identification of non-zero values easier. It also predicts that there should not be any variation of analysing power with relative energy. If such a variation did occur the analysis of the data would require that it be binned with respect to relative energy. The amount of data required to do this successfully is more than it was expected would be obtained in the time available. The analysing powers were determined for both sequential and direct data. The direct breakup analysing powers will be discussed first.

All the direct $^TT_{20}$ were determined from the projected energy spectra. The gates used were always well away from the data originating from the sequential process to ensure its complete exclusion. The data was integrated between limits corresponding to a relative energy of 1.7MeV. This is not possible when determining differential cross sections as the absolute number of counts detected is what is required. The analysing powers were calculated as described in section 5.4 and are shown in figure 5.11. The analysing powers for 9°, 12° and 15° are seen to agree with the calculation discussed in chapter 2 whereas those at 20° and 25° do not. The latter angles lie near or beyond the grazing angle of 21.3° and hence nuclear interactions are expected to be important. The agreement between the theory and the data at the three forward angles indicates that the direct breakup of ^7Li is dominated by processes for which $\lambda = 1$. As discussed in section 2.5 a predominantly $\lambda = 1$ process for the reaction $^{120}Sn(^7Li, \alpha + t)^{120}Sn_{g.s.}$ implies a

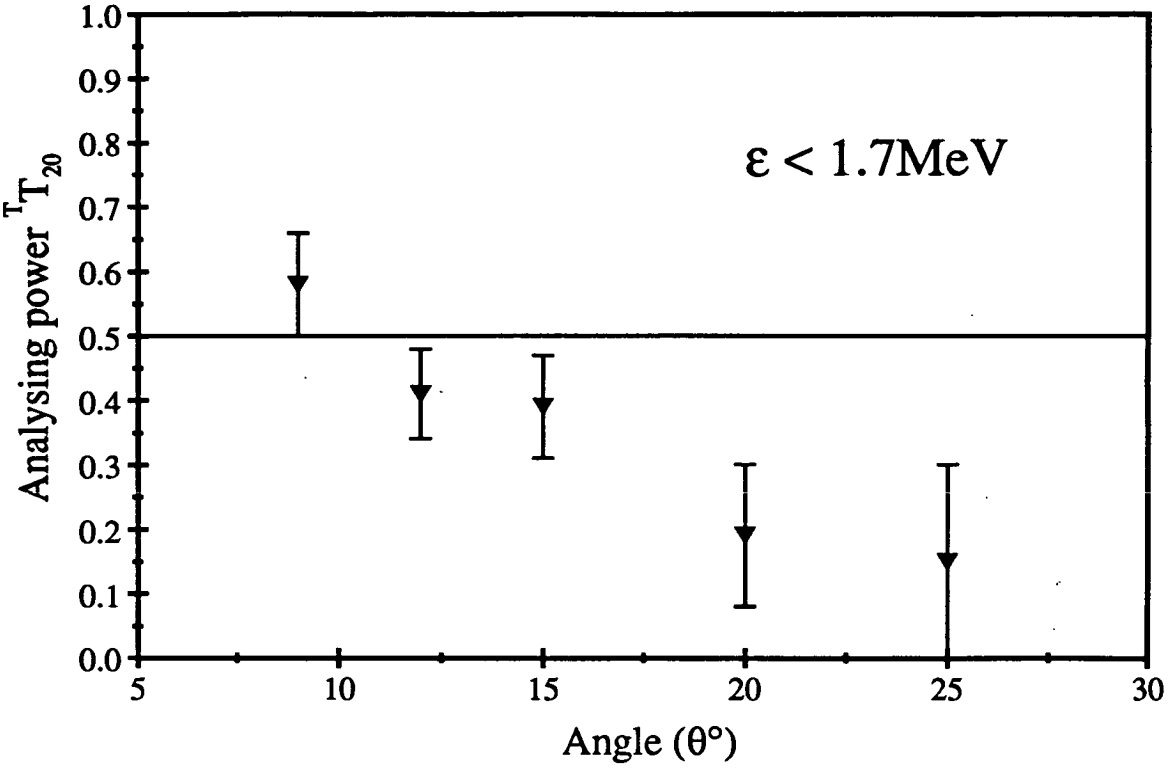

Figure 5.11: *The analysing power $^{T}T_{20}$ for the direct breakup data from the reaction $^{120}Sn(^{7}Li, \alpha + t)^{120}Sn_{g.s.}$. The error bars are statistical. The solid line is the semi-classical prediction for $^{T}T_{20}$ from section 2.5.*

mainly Coulomb interaction[1]. This data therefore supports the thesis that the direct breakup of ^{7}Li at forward angles is mainly driven by the Coulomb interaction. The disagreement between the theory and the data at 20° and 25° provides evidence for the supposition that the nuclear interaction does not favour $\lambda = 1$ and therefore supports the assumption that breakup where $\lambda = 1$ is mainly Coulomb.

The calculation in section 2.5 shows that for this particular breakup reaction no relative energy dependence of $^{T}T_{20}$ is expected for $\lambda = 1$ processes. Determining $^{T}T_{20}$ for various relative energy bins therefore also provides a test of the theory and an absence of any variation of $^{T}T_{20}$ with relative energy would provide additional evidence for its validity. The division of the data into many small relative energy bins would provide a more stringent test, but lack of data makes this impracticable. This limitation caused the number of bins to be restricted to two. The gates used are shown in figure 5.9, one is for data with a relative energy between the minimum

[1] see footnote on page 36 and the DWBA calculation of Bertualani et al. [Be91]

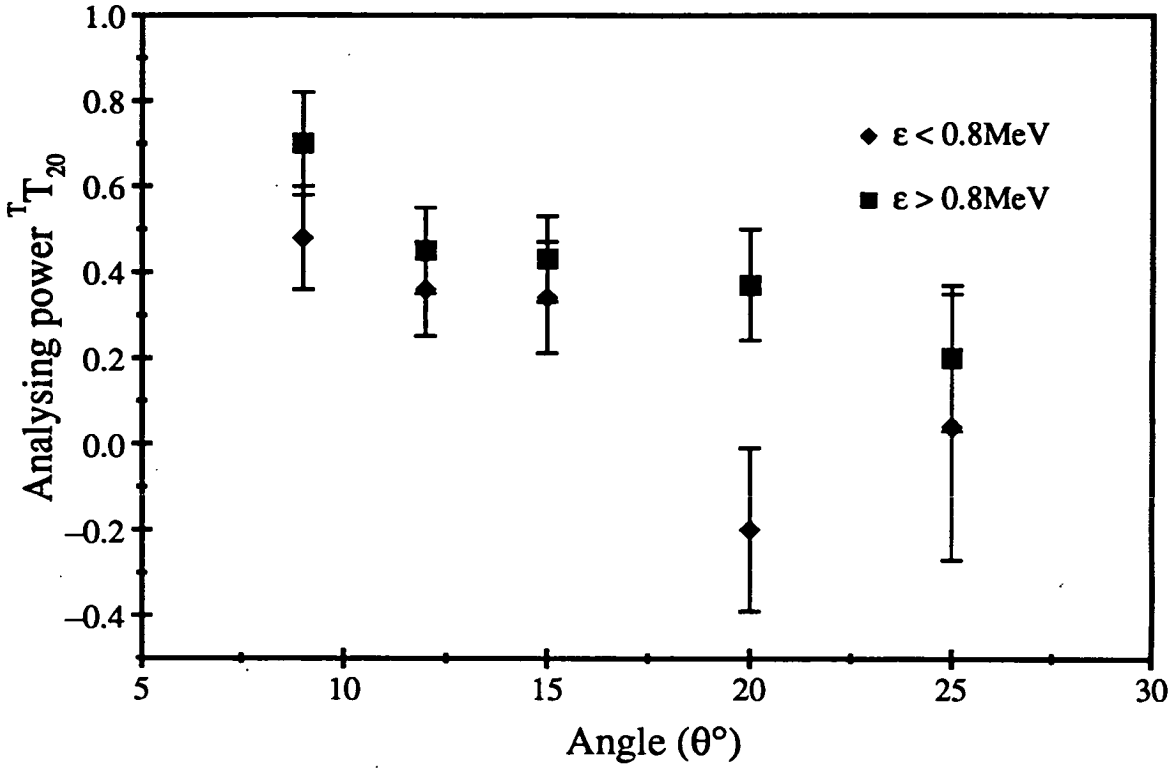

Figure 5.12: *The analysing power $^{T}T_{20}$ for the direct breakup data from the reaction $^{120}Sn(^{7}Li, \alpha + t)^{120}Sn_{g.s}$ for two relative energy gates.*

detectable, 0.03MeV, and 0.8MeV and the other is for data were the relative energy is greater than 0.8MeV and less than 1.7MeV. This division was chosen to approximately divide the data into two equal parts at 12°. The calculated analysing powers are shown in figure 5.12. At the angles where the analysing powers calculated using all the data were found to agree with the calculation of section 2.5 no difference between $^{T}T_{20}$ calculated for the two gates is observable to within errors providing further evidence for the validity of the theory. At 20° the analysing powers are seen to be quite different. There is no reason not to expect a relative energy dependence at this angle and the observation of such a dependence supports the use of the lack of observation of such a dependence at 9°, 12° and 15° as evidence for the validity of the theory in question. At 25° the small amount of data at low relative energies results in a very large statistical error for $^{T}T_{20}$ for $\varepsilon > 0.8$MeV making deductions from this data impossible.

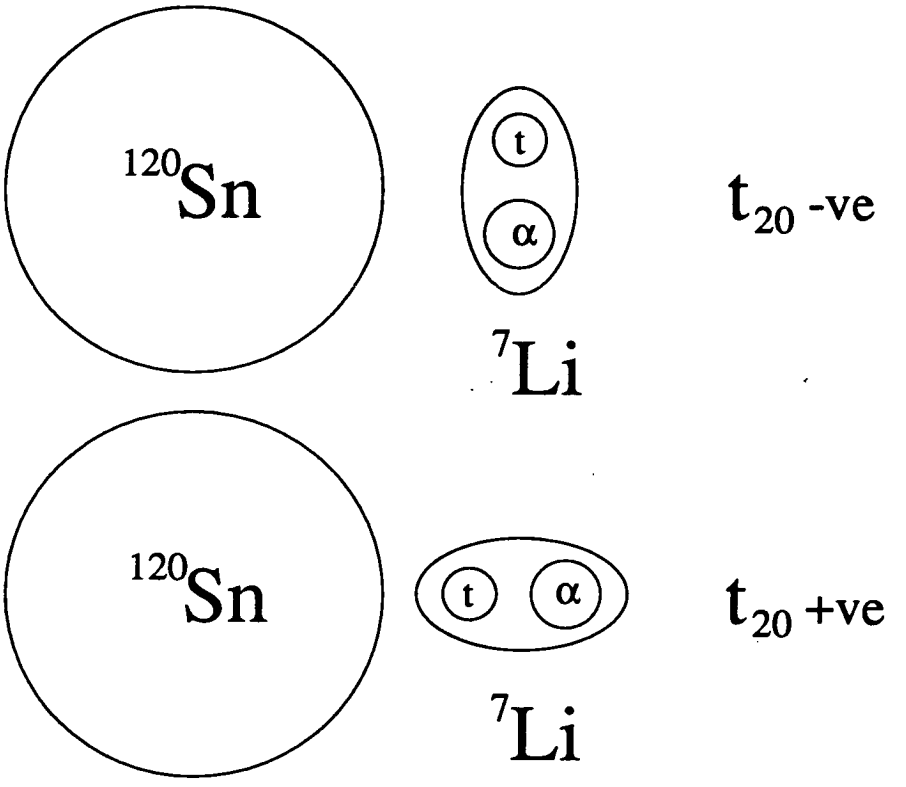

Figure 5.13: *The shapes given to the ^{7}Li in the above diagram result from a superposition of the shape of a ^{7}Li nucleus and the polarization stated. The beam direction (y axis) is into the plane of the paper and in both cases the nucleus appears circular when viewed along the z direction in the transverse frame. The polarized beam thus presents effectively oblate and prolate shapes to the target when the t_{20} polarization is respectively positive and negative. The polarization clearly affects the proximity of the constituent clusters of the projectile to the target.*

As already mentioned the asymmetry in the direct breakup data observed in the projected energy spectra may be due to final state interactions. This causes the fragments to deviate from their original orbits. One possible way of quantifying this phenomenon is to use analysing powers. If the projectile ^7Li can be thought of as an α t cluster then when the beam is polarized the orientation of the projectile at the target should affect the final state interactions. When a polarized beam is used the nuclear spins no longer point randomly in all directions. This means that nuclei will present an effective shape to the target which will depend on the polarization of the beam. In the helicity frame the beam used had nonzero t_{10}, t_{20} and t_{30} polarizations in the source. The only significant polarization here however is t_{20} because the other two do not change sign in the different phases used. Using the diagram for t_{20} polarization in figure 2.3 and noting that ^7Li possesses a negative quadrupole moment, effective shapes for the ^7Li in the two phases used can be deduced. These are shown schematically in figure 2.3. In the two cases illustrated the fragments emerging with the same energies may follow different paths and therefore undergo different final state interactions. Final state interactions should therefore affect any measured analysing powers.

At any particular relative energy there are two kinematically possible solutions that will produce ejectiles in any specfic set of directions. The superposition of the effect of polarizing the beam on the two kinematically possible situations may allow the identification of different final state interactions in each of the cases via analysing powers. Analysing powers were determined for data corresponding to high energy αs and low energy ts and vice versa for the same relative energy range in each case (see figure 5.14). The analysing powers can be seen to be the same to within statistial errors and therefore any final state interaction effects are not identifiable in this case.

Analysing powers were also calculated for the sequential breakup data. The greatest problem here was in the subtraction of the direct breakup background. This is easier if relative energy spectra are used which are determined by using equation 2.44. An example of a relative energy spectrum is shown in figure 5.10.

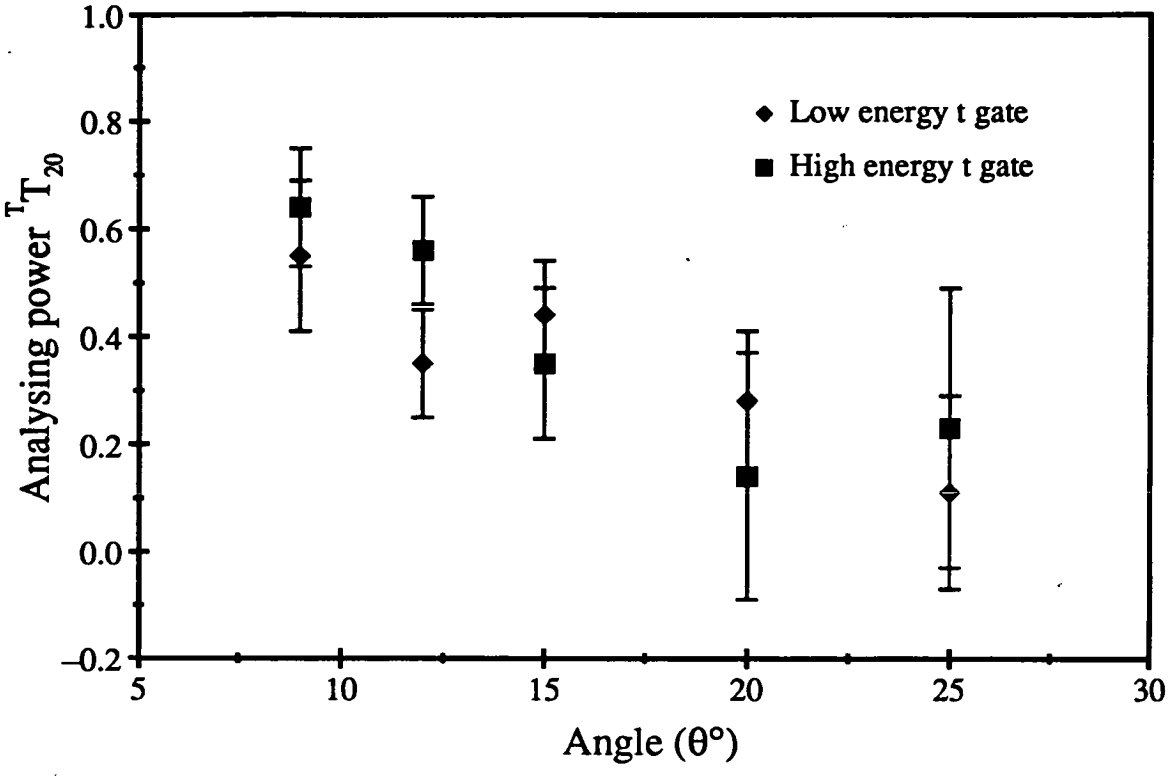

Figure 5.14: *The analysing power $^{T}T_{20}$ for the direct breakup data from the reaction $^{120}Sn(^{7}Li, \alpha + t)^{120}Sn_{g.s}$. The two gates correspond to the cases where, in the α t centre of mass system, the α is forward and the t backward going and vice versa. (see text)*

Analysing powers calculated using these spectra are shown in figure 5.15. The very small differential cross section for the 12° data makes it impossible to calculate an analysing power for this angle. The result of the Coulomb calculation described in section 2.5 is also shown in the figure and all the data are seen to disagree with it. The comparison of sequential differential cross section data with a Coulomb calculation in [Sh89] shows that the theory and the data agree at angles 11.5° and 15°. The analysing power data in figure 5.15 does not confirm that this is a Coulomb dominated interaction over the range examined. The lowest possible multipolarity associated with this transition is a $\lambda = 2$ one. The nuclear contribution might therefore be expected to be more comparable to the Coulomb contribution (see for example the DWBA calculation of Bertualani et al. [Be91]).

The analysing power will be more sensitive to any nuclear contribution than the differential cross section and the disagreement between the measured analysing powers and the calculation may be a reflection of this.

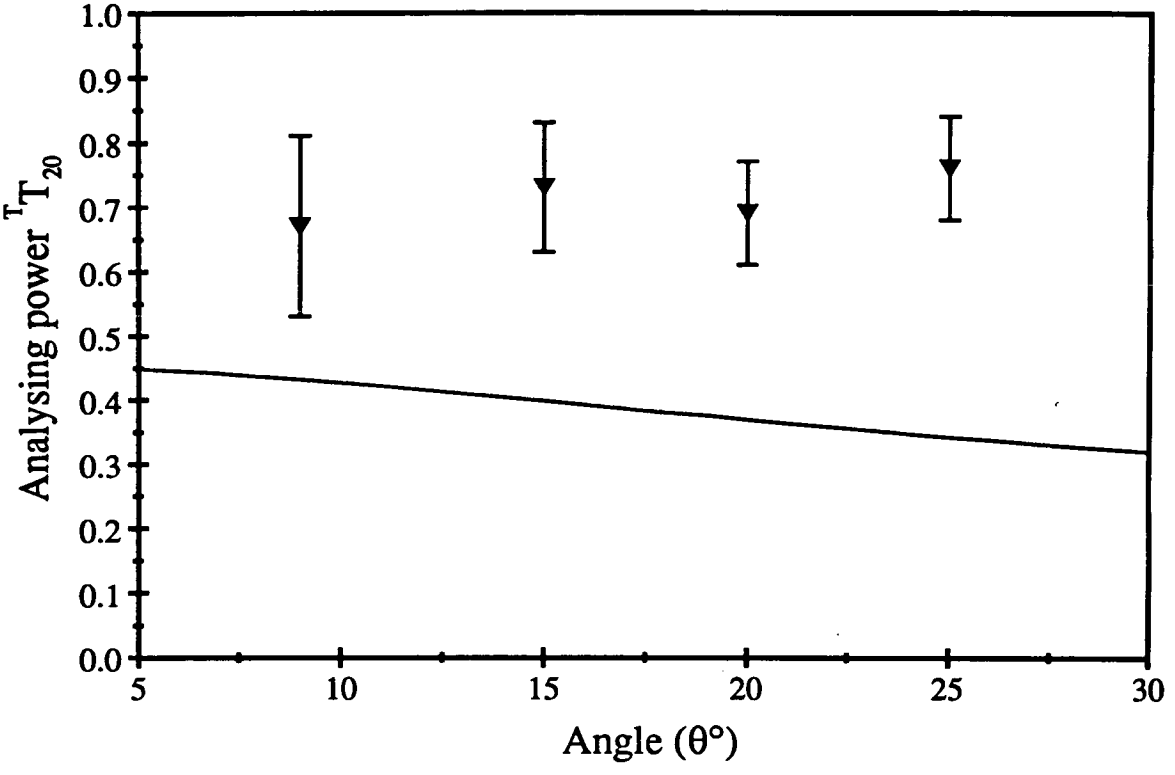

Figure 5.15: *The analysing power $^{T}T_{20}$ for all of the sequential breakup data from the reaction $^{120}Sn(^{7}Li, ^{7}Li_{4.63} \rightarrow \alpha + t)^{120}Sn_{g.s.}$. The solid line is the semi-classical prediction for $^{T}T_{20}$ from section 2.5. (see also figure 2.4)*

Analysing powers can be calculated for the separate sequential peaks. The breakup of the excited ^{7}Li is expected to take place at some distance from the target nucleus, the lifetime of the 4.63MeV state is of the order of 10^{-20}s whereas the time the ^{7}Li takes to travel a distance of the order of a nuclear diameter is $\sim 10^{-22}$s. Final state interactions are therefore not expected. If this is the case the analysing powers for the two peaks should be the same. The values calculated from projected spectra are shown in figure 5.16. All the values are in good agreement except those at 15°. This is unexpected and there is a substantial difference between the two values. A possible source of part of this discrepancy is in the subtraction of the background due to direct breakup. In order to calculate

analysing powers for the separate peaks projected energy spectra must be used. The difficulty of background subtraction in these spectra was commented upon in section 5.3. This however cannot account for the whole discrepancy. It is not explicable in terms of any obvious experimental problems such as a reduction in beam polarization as this would affect both kinematic solutions equally. The lack of any discrepancies occuring in any other 15° data also rules out any fault in one phase of the polarized source being the culprit and appears to indicate that the difference is specific to the sequential α t breakup reaction. At present no satisfactory explanation of the discrepancy at 15° exists.

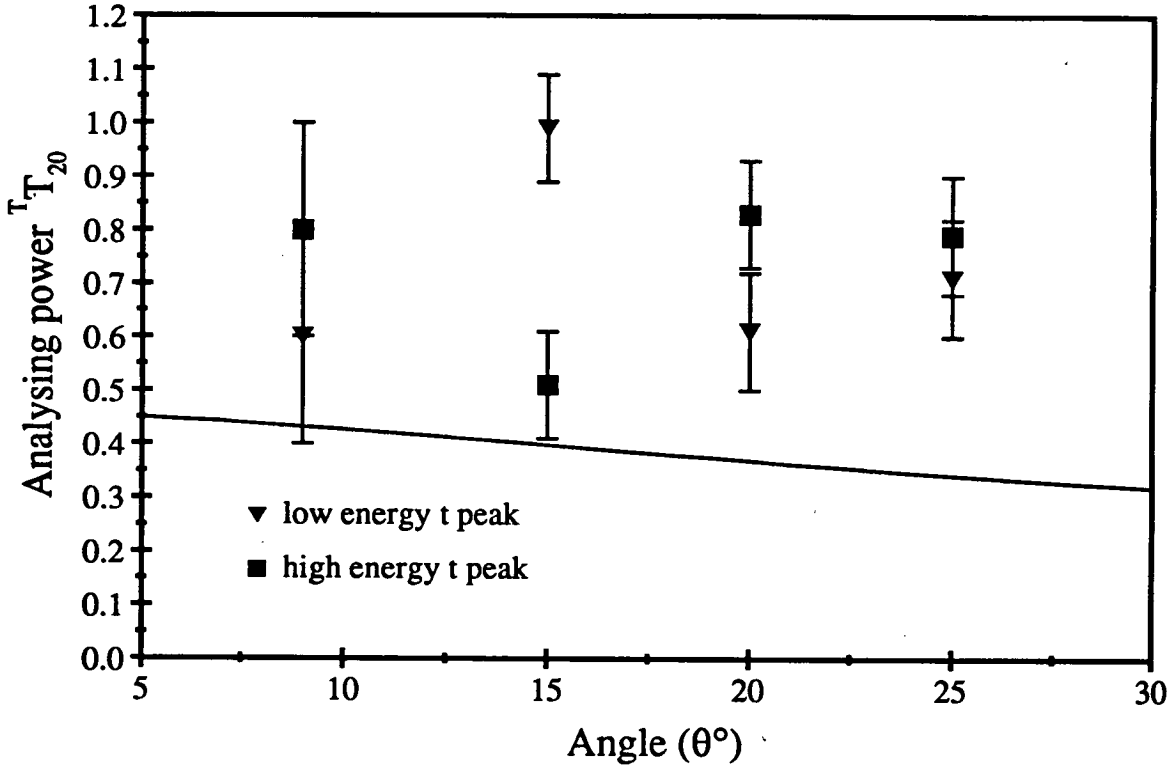

Figure 5.16: *The $^{T}T_{20}$ analysing powers for the two peaks resulting from sequential breakup of ^{7}Li into an α and a t. The solid line is the semi-classical prediction for $^{T}T_{20}$ from section 2.5. (see also figure 2.4)*

Cross sections

As described in section 5.5 the data acquired using a polarized beam can also be used to determine differential cross sections. The proposition that the direct

breakup of ^7Li at forward angles is dominated by the Coulomb interaction originated from a comparison of the data of [Da87] with a semi-classical Coulomb calculation which is described in section 2.7. These data covered an angular range of 11.5° to 45°. The present data cover the range 9° to 25° and hence provides a further datum at small angles.

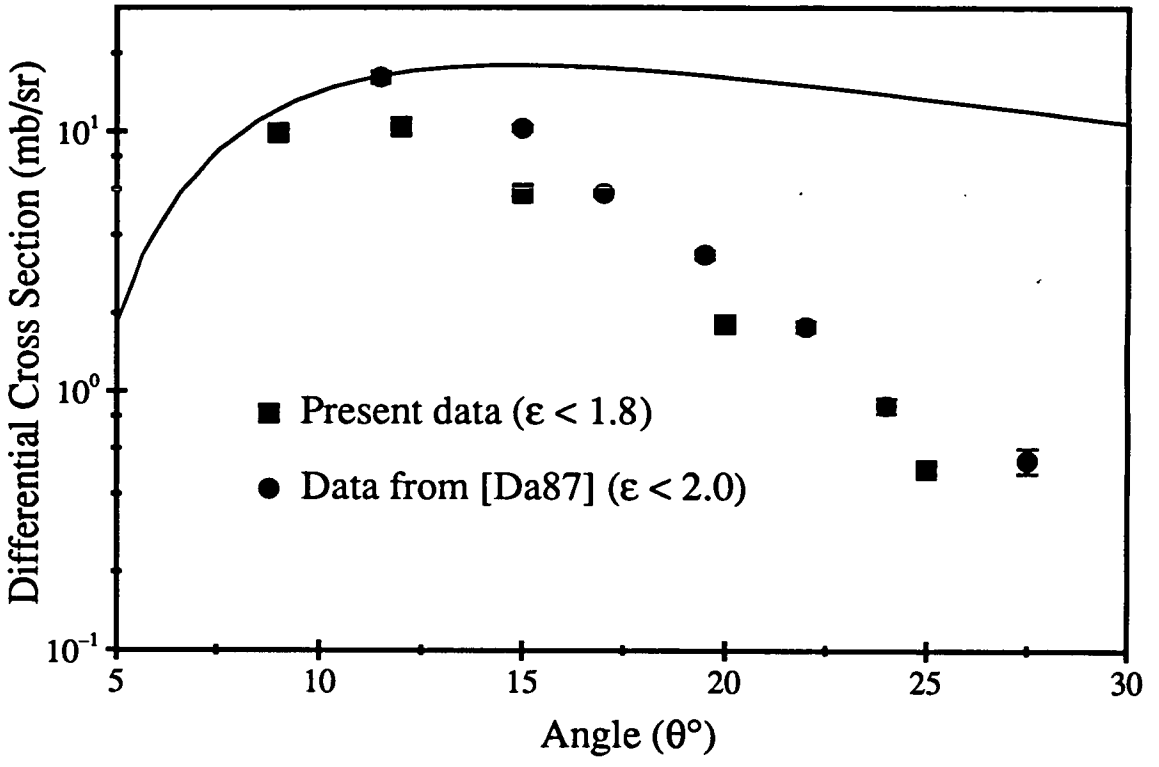

Figure 5.17: *The differential cross section for the direct breakup data from the reaction* $^{120}Sn(^7Li, \alpha + t)^{120}Sn_{g.s.}$. *The calculation corresponds to the present data set. (The angles are laboratory ones.) The solid line is the semi-classical prediction for the differential cross section from section 2.7.*

One of the problems encountered when determining differential cross sections is the differentiation between direct and sequential events. An examination of the data around the sequential peaks in figure 5.8 shows that there is no hard and fast division between the two types of breakup. It is possible to improve the situation by using a relative energy spectrum rather than a projected energy one to separate the data. Presenting the data in this way effectively stretches out the scale around the sequential energy peaks enabling the direct and sequential events

to be more clearly distinguished. This technique is particularly advantageous when considering the data acquired at 12°. The identification of the peak associated with a low energy t, high energy α coincidence using projected energy spectra is almost impossible, a peak is clear though in the relative energy spectrum. The background subtraction from sequential energy peaks, as already mentioned in connection with the determination of analysing powers, is also much easier when using relative energy spectra.

The differential cross sections for the direct breakup data are shown in figure 5.17. The results of the semi-classical Coulomb calculation described in section 2.7 and the data obtained by Davinson [Da87] are also shown in the figure. The data from [Da87] has been reduced by 20% from the values shown in that work. In the course of the present work it was discovered that an error had been made in interpreting the output of the Monte Carlo code used in [Da87] to determine the effective solid angles. The 20% reduction in the magnitudes of the differential cross sections necessitated by this error has been applied to all the data from [Da87]. Though the distributions of the two sets of data are seen to have the same shape they differ in absolute magnitude by about 25%. The difference in relative energy ranges covered only accounts for a small part of this but it does not account for the entire discrepancy for which there are several possible reasons. The Monte Carlo code described in chapter 4 was used to determine the effective solid angles. The $d\sigma(\theta)/d\Omega d\varepsilon$ functions used in this work are shown in figure 4.1. In Davinson's work a single $d\sigma(\theta)/d\Omega d\varepsilon$ was used for all angles. This difference results in slightly different effective solid angles and hence contributes to the magnitude discrepancy between the two sets of data. This however is only a minor source of error. Subsequent sections in this chapter deal with data obtained for α, d and α, α coincidences. The differential cross sections for these reactions have also been found to differ from those of [Da87] by similar magnitudes to the discrepancy in the direct data case. This implies a systematic error, the most obvious of which is an error in the target thickness. The error in the thickness of the target used in the present experiment is estimated to be at least 10%.

Allowing for a similar error in the data of [Da87] this may account for the whole of the discrepancy.

This problem is an illustration of one of the advantages of analysing powers over differential cross sections. A knowledge of effective solid angles is not required for the determination of analysing powers. Experimental fusion data is therefore not needed eliminating the first possible source of error mentioned above. Any systematic errors which are not phase dependent such as errors in target thicknesses are also irrelevant when considering analysing powers. Thus none of the above sources of error which plague differential cross sections affect analysing powers.

The new data point at 9° is very close to the Coulomb calculation and does not follow the upward trend of the data from 25° to 12°. This may indicate the start of a down turn in the differential cross section data following the trend in the Coulomb calculation. As already discussed however there are several possible sources of systematic error. The apparent convergence of the data and the calculation should therefore be treated with caution.

The differential cross sections for the sequential data were determined using relative energy spectra and are shown in figure 5.18. A difference in magnitude between the data of [Da87] and the present data of about 25% is observable, however the trends in the data are clearly the same. The new datum at 9° is particularly interesting as it shows that the differential cross section is higher than the 12° value indicating the start of oscillations in the data typical of *Fresnel* types of scattering. The result of the semi-classical calculation shown in figure 5.18 does not show this oscillation precisely because it is semi-classical and treats the path followed by the projectile during the reaction as a classical one. The calculated differential cross section depends on this through the orbital integrals used. In order to produce oscillations diffraction around the nucleus must be allowed to occur and a nuclear potential is required to produce this effect. The analysing power data indicated that the sequential breakup of ^7Li is not purely Coulomb at forward angles and the differential cross section data supports this conclusion.

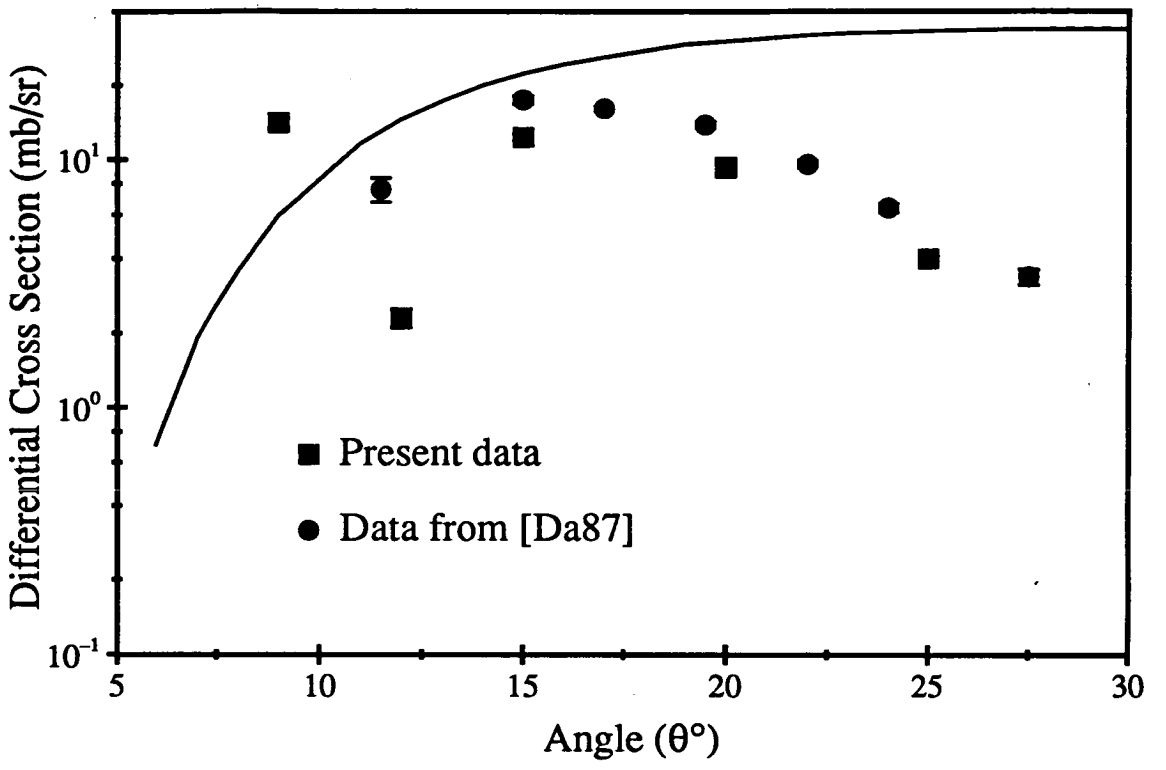

Figure 5.18: *The differential cross section for the sequential data from the reaction* $^{120}Sn(^7Li, ^7Li_{4.63} \rightarrow \alpha + t)^{120}Sn_{g.s.}$. *(Angles in laboratory). The solid line is the semi-classical prediction for the differential cross section from section 2.7.*

5.6.2 α d Coincidence Data

Coincidences between α and d particles were observed. As in the section on α, t coincidences the general properties of the data are discussed with reference to effectively unpolarized data. A 2D spectrum of E_α verses E_d where the only condition imposed was that the α and d be detected simultaneously is shown in figure 5.19. The data are seen to lie mainly along two loci. Also plotted are the kinematic and relative energy loci which correspond to the transfer breakup reaction $^{120}Sn(^7Li, ^6Li^* \rightarrow \alpha + d)^{121}Sn$. The relative energy loci are for the 2.18MeV 3^+ and the 5.65MeV 1^+ states of ^6Li. The kinematic locus is for the ground state of ^{121}Sn. The data is seen to lie mainly along the relative energy locus for the 2.18MeV state, but unlike the α t coincidence data a large amount of data corresponds to inelastic breakup. The summed energy spectrum in figure 5.20 shows

discrete states corresponding to states in ^{121}Sn and a continuum. Of the data associated with discrete states the largest fraction corresponds to elastic breakup.

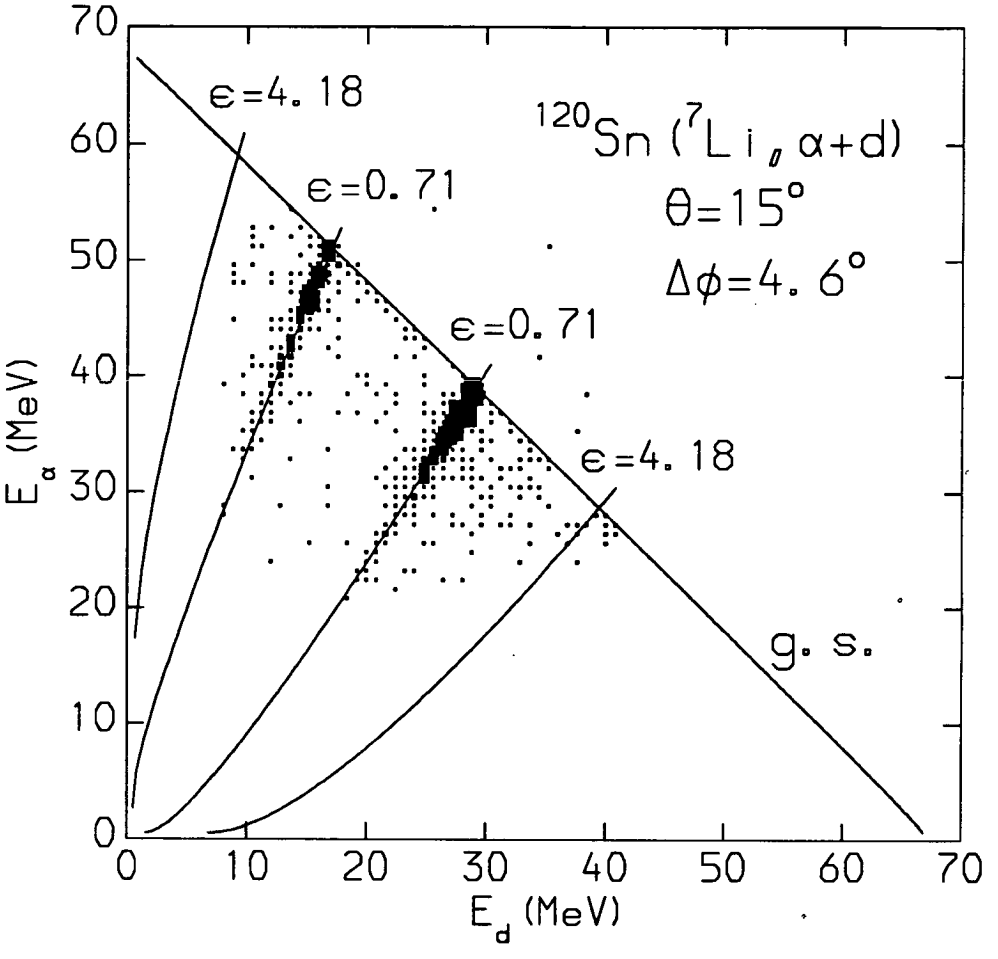

Figure 5.19: *α energy verses d energy from the reaction $^{120}Sn(^7Li, \alpha + d)$, no energy gates were imposed to obtain this spectrum.*

Projected energy spectra for elastic breakup produced by using the total energy gate shown in figure 5.20, look similar at all the angles at which data were taken. Figure 5.21 shows an example of a such a spectrum and a Monte Carlo simulation. The simulation allows the reaction to proceed via the 2.18MeV state of ^6Li. Comparison with the data shows that most of the data correspond to sequential reactions via these two states and there is very little evidence of any direct mechanism. Only one peak which corresponds to breakup via the 5.65MeV state can be seen in the experimental spectrum in figure 5.21. This is a conse-

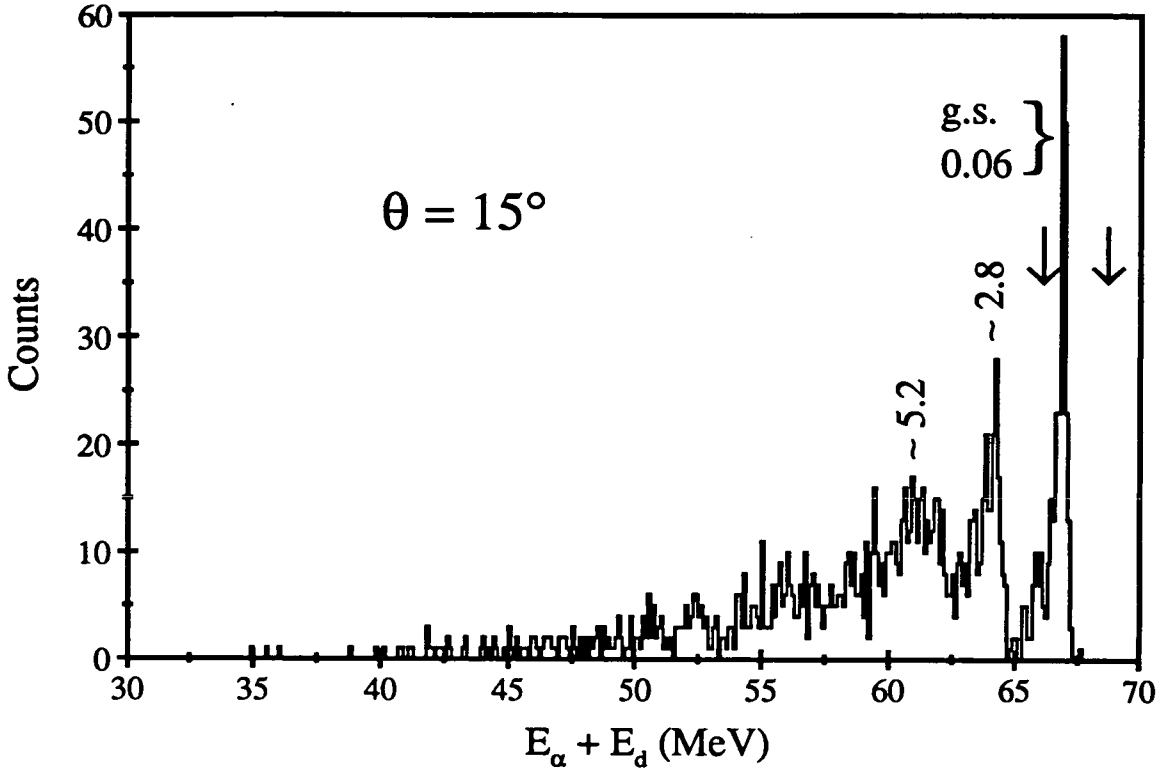

Figure 5.20: *Sum of the α and d energies from the reaction $^{120}Sn(^7Li, \alpha + d)$ for a beam energy of 70MeV. The energies noted on the diagram are the energies of the excited states of the recoil nucleus ^{121}Sn that correspond to the identified peaks. The arrows as before indicate the total energy gate used.*

quence of the thickness of the ΔE detectors used in the telescopes. The low energy deuteron associated with the missing peak would have been stopped by the ΔE resulting in the criteria for a telescope event (i.e. a ΔE, E coincidence) not being met.

Analysing Powers

Analysing powers were determined for the reaction $^{120}Sn(^7Li, ^6Li^*_{2.18} \rightarrow \alpha + d)^{121}Sn_{g.s.,0.06}$ They were determined using the data corresponding to breakup via the 2.18MeV state of ^6Li for the separate sequential peaks and for the sum of the data and are shown in figure 5.22. All the $^TT_{20}$ analysing powers determined were found to be positive. The schematic diagram of the effective shape of ^7Li in figure

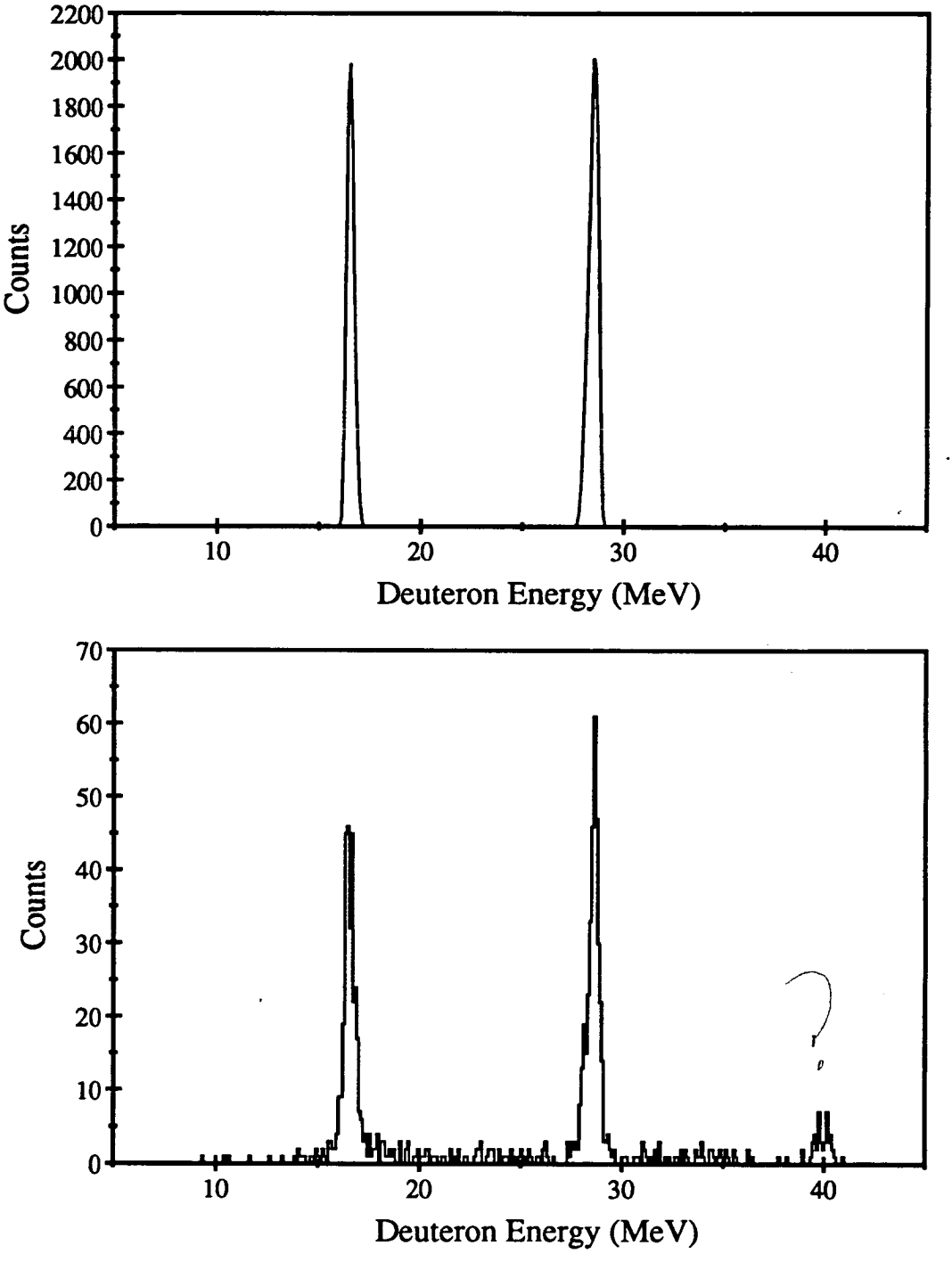

Figure 5.21: *The top figure shows a Monte Carlo simulation of the reaction* $^{120}Sn(^{7}Li, ^{6}Li^{*}_{2.18} \rightarrow \alpha + d)^{120}Sn_{g.s.,0.06}$. *The lower figure shows the data obtained for the reaction* $^{120}Sn(^{7}Li, \alpha + d)^{120}Sn_{g.s.,0.06}$. *It is immediately evident that very little data does not correspond to the sequential reaction.*

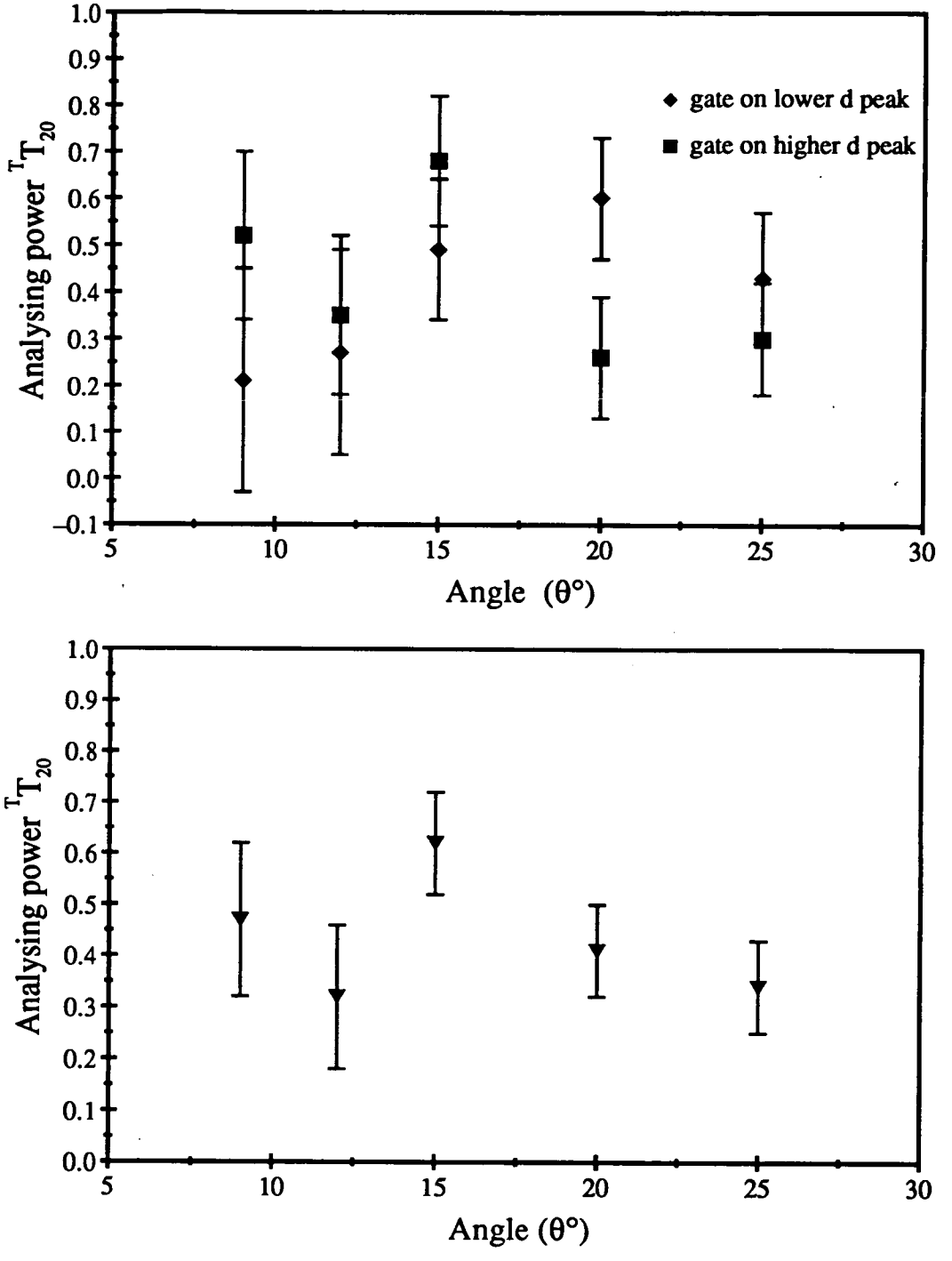

Figure 5.22: *The top figure shows the analysing power* $^{T}T_{20}$ *determined for each of the sequential peaks in the data from the reaction* $^{120}Sn(^{7}Li, ^{6}Li^{*}_{2.18} \rightarrow \alpha + d)^{121}Sn_{g.s.,0.06}$. *The lower figure shows* $^{T}T_{20}$ *determined from all of the data.*

5.13 illustrates the reason for this. The closer together the nuclear surfaces, the easier the transfer of a neutron from ^7Li to the ^{120}Sn target should be. In the two cases illustrated this occurs when t_{20} is positive resulting in a positive value for $^{T}T_{20}$. The analysing powers for the separate peaks agree showing no evidence of final state interactions as expected. The mean lifetime, τ, of the 2.18MeV state of ^6Li is $\sim 10^{-20}$s whereas the transition time is $\sim 10^{-22}$s. When breakup takes place therefore the ^6Li nucleus is at a sufficiently large distance for any interaction to be negligible. There is possibly some structure evident in the analysing powers for all the data however a smooth curve peaking at 15° would also be concordant with the data.

Cross sections

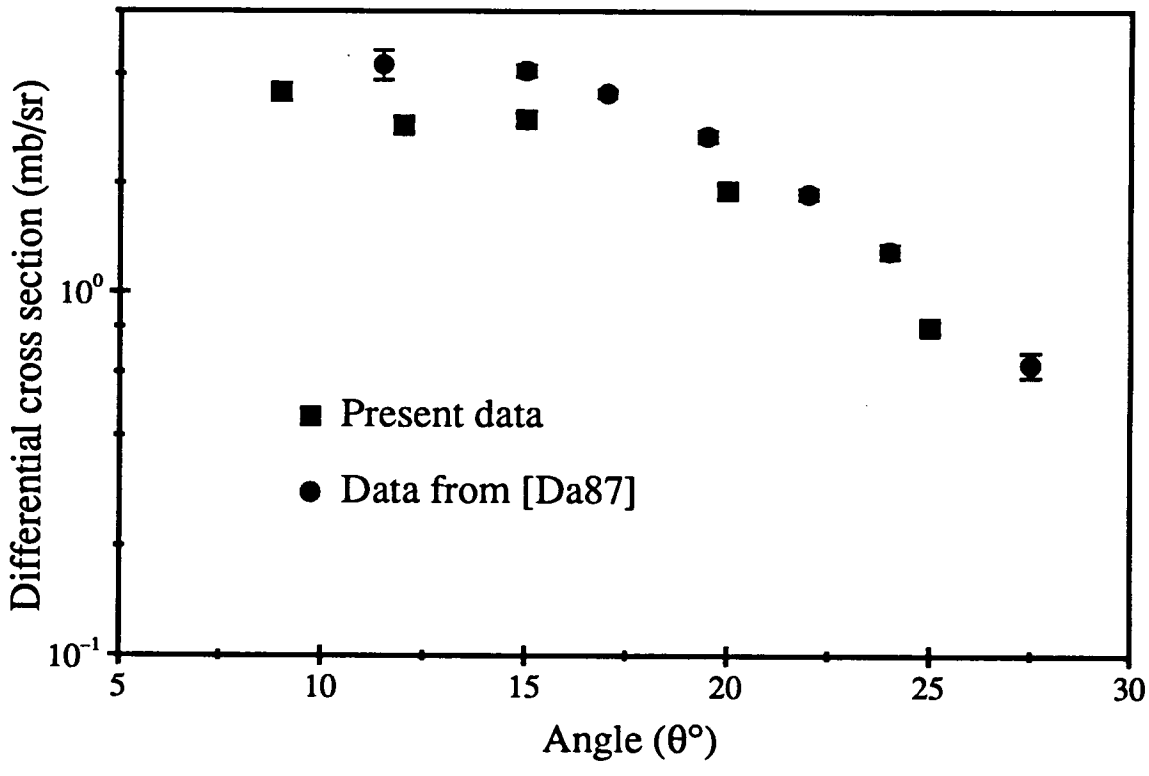

Figure 5.23: *Differential cross section data for the reaction* $^{120}Sn(^7Li, ^6Li^*_{2.18} \rightarrow \alpha + d)^{121}Sn_{g.s.,0.06}$

Differential cross sections were calculated for the reaction $^{120}Sn(^{7}Li, ^{6}Li^{*}_{2.18} \rightarrow \alpha+d)^{121}Sn_{g.s.,0.06}$. Very little data other than those which correspond to sequential breakup are observed in α, d coincidences. The problem encountered for α, t coincidences of differentiating between the two possible types of event i.e. direct and sequential breakup therefore does not arise here. The differential cross sections determined from the data are shown in figure 5.23 along with data from [Da87]. The difference in magnitude of the two sets of data discussed in section 5.6.1 is once again observable. The trends in the data though are seen to be the same and the datum at 9° shows a slightly increasing trend in the differential cross section.

5.6.3 α α Coincidence Data

Coincidences between two α particles were also observed in the experiment under consideration. As in the two previous sections the general properties of the data will be discussed with reference to effectively unpolarized data. A 2D plot of E_{α_1} verses E_{α_2} is shown in figure 5.24. The spectrum is seen to be dominated by a locus at $E_{\alpha_1} \approx E_{\alpha_2}$. This observation suggests that the reaction producing these αs is $^{120}Sn(^{7}Li, ^{8}Be \rightarrow \alpha + \alpha)^{119}In$. Kinematic and relative energy loci for this reaction are also plotted in the figure. The relative energy loci are for the ground, 0^+ and first excited, 3.04MeV 2^+ states of ^{8}Be. The data at $E_{\alpha_1} \approx E_{\alpha_2}$ are seen to correspond to the locus for $^{8}Be_{g.s.}$ ($\varepsilon = 0.092$) and a small amount of data are seen to lie along the loci for $^{8}Be_{3.04}$ ($\varepsilon = 3.13$). A summed energy spectrum is shown in figure 5.25. It consists of a peak corresponding to the unresolved ground and first excited states (0.31MeV $\frac{1}{2}^-$) of the recoil nucleus ^{119}In and a continuum region.

Projected energy spectra were produced by placing a gate on the ground + first excited states in the summed energy spectrum. These spectra look similar at all angles, an example of which is shown in figure 5.26. The spectrum produced by a Monte Carlo simulation, allowing the reaction to proceed via the ground and 3.04MeV states of ^{8}Be, reproduces the data very well. The dominant broad peak being the result of breakup via the ground state of ^{8}Be and the small peaks

to either side of it the result of breakup via $^8Be_{2.94}$. Any data due to breakup transfer reactions would not be confined to the sequential peaks. There is very little evidence for any such reactions confirming that the reaction is predominantly sequential.

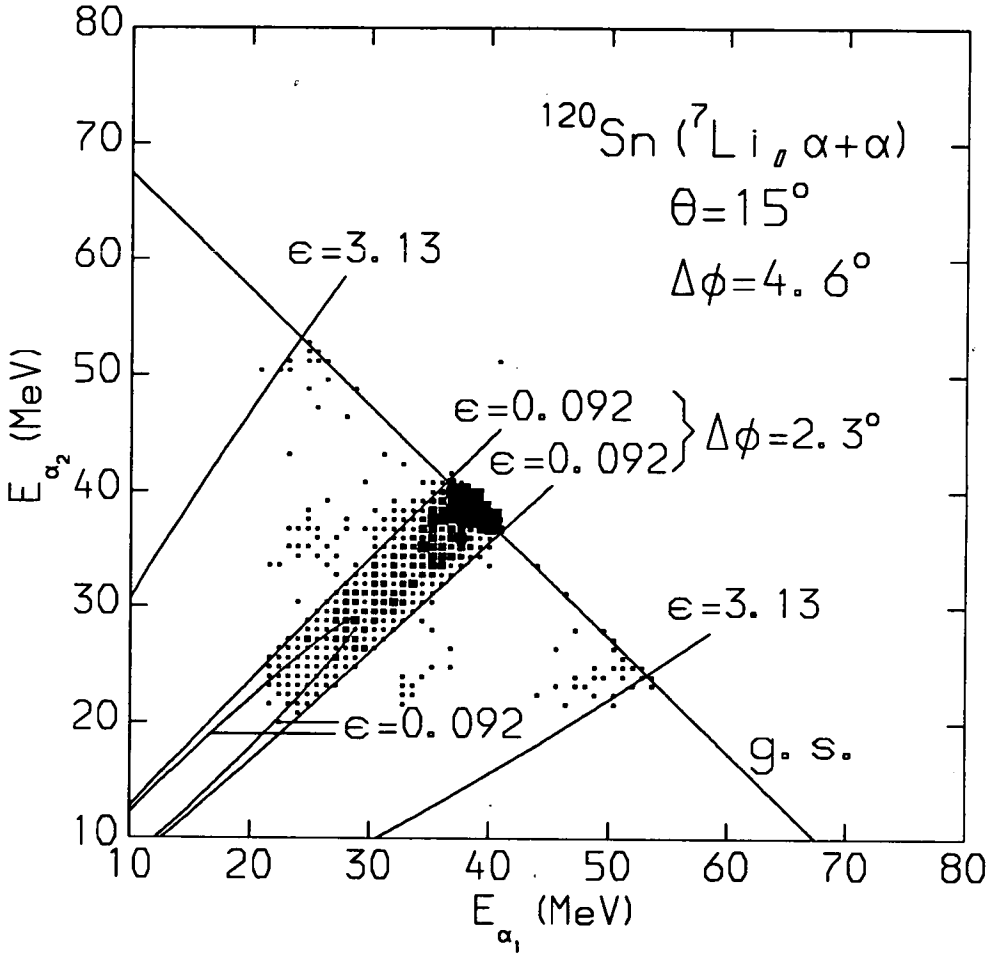

Figure 5.24: *α energy verses α energy from the reaction $^{120}Sn(^7Li, \alpha + \alpha)$, no energy gates were imposed to obtain this spectrum. $\Delta\phi$ = 2.3° and 4.6° are the minimum and average angular separations of the detectors. The two sets of loci for these separations show that the origin of the peak width for the reaction $^{120}Sn(^7Li, ^8Be_{g.s.} \rightarrow \alpha + \alpha)$ is the solid angle subtended by the detection system.*

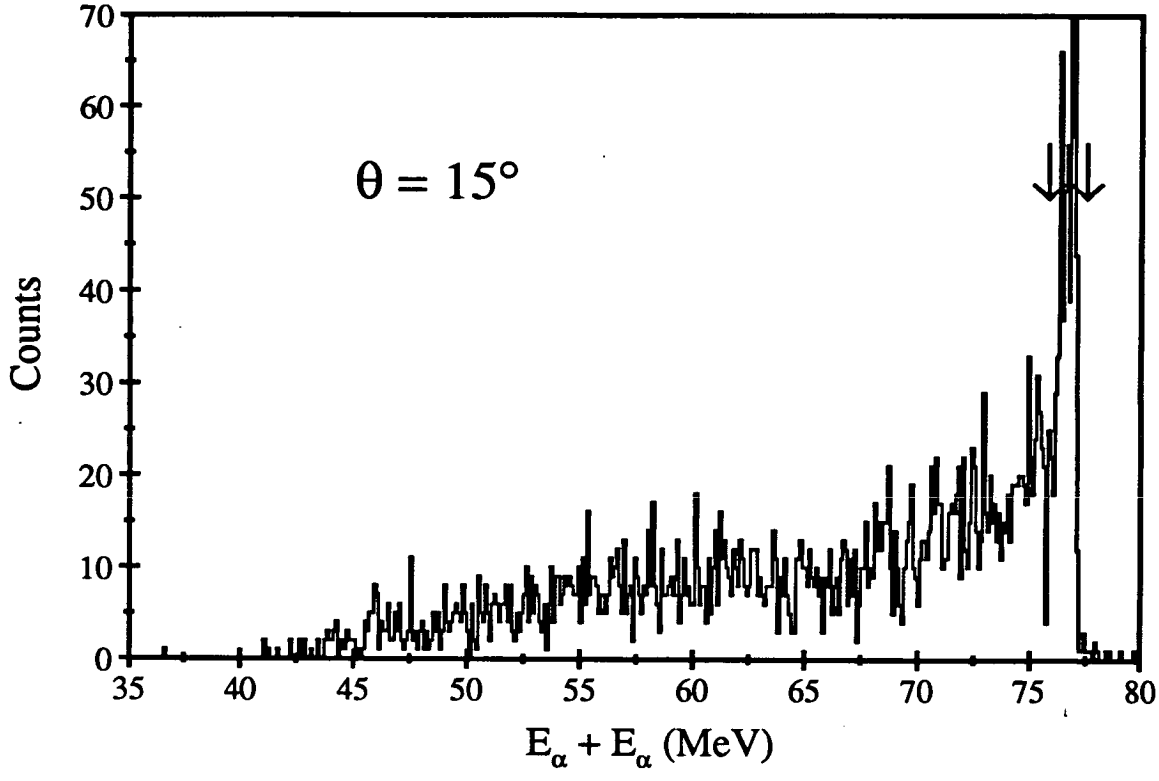

Figure 5.25: *Sum of the α energies from the reaction $^{120}Sn(^7Li, \alpha + \alpha)$, for a beam energy of 70MeV. The arrows enclose the ground and first excited states (0.31MeV) of ^{119}In and indicate the position of the total energy gate used.*

Analysing powers

The analysing powers, $^TT_{20}$ were determined for the reaction $^{120}Sn(^7Li, ^8Be_{g.s.} \rightarrow \alpha + \alpha)^{119}In_{g.s.,0.31}$. Large positive analysing powers were found at all angles measured (see figure 5.27). The analysing powers appear to lie on a smooth curve with a maximum at about 18°.

The reason for the occurence of positive analysing powers is the same as in the case of α d coincidences. The greater proximity of the nuclear surfaces for a positive value of t_{20} facilitates the transfer of a proton from the ^{120}Sn target to the ^7Li resulting in a positive $^TT_{20}$. The increase in $^TT_{20}$ to $\sim 18°$ may be a reflection of the decrease in impact parameter causing the difference in the proximity of the nuclear surfaces in the two phases to become a larger fraction of the total distance.

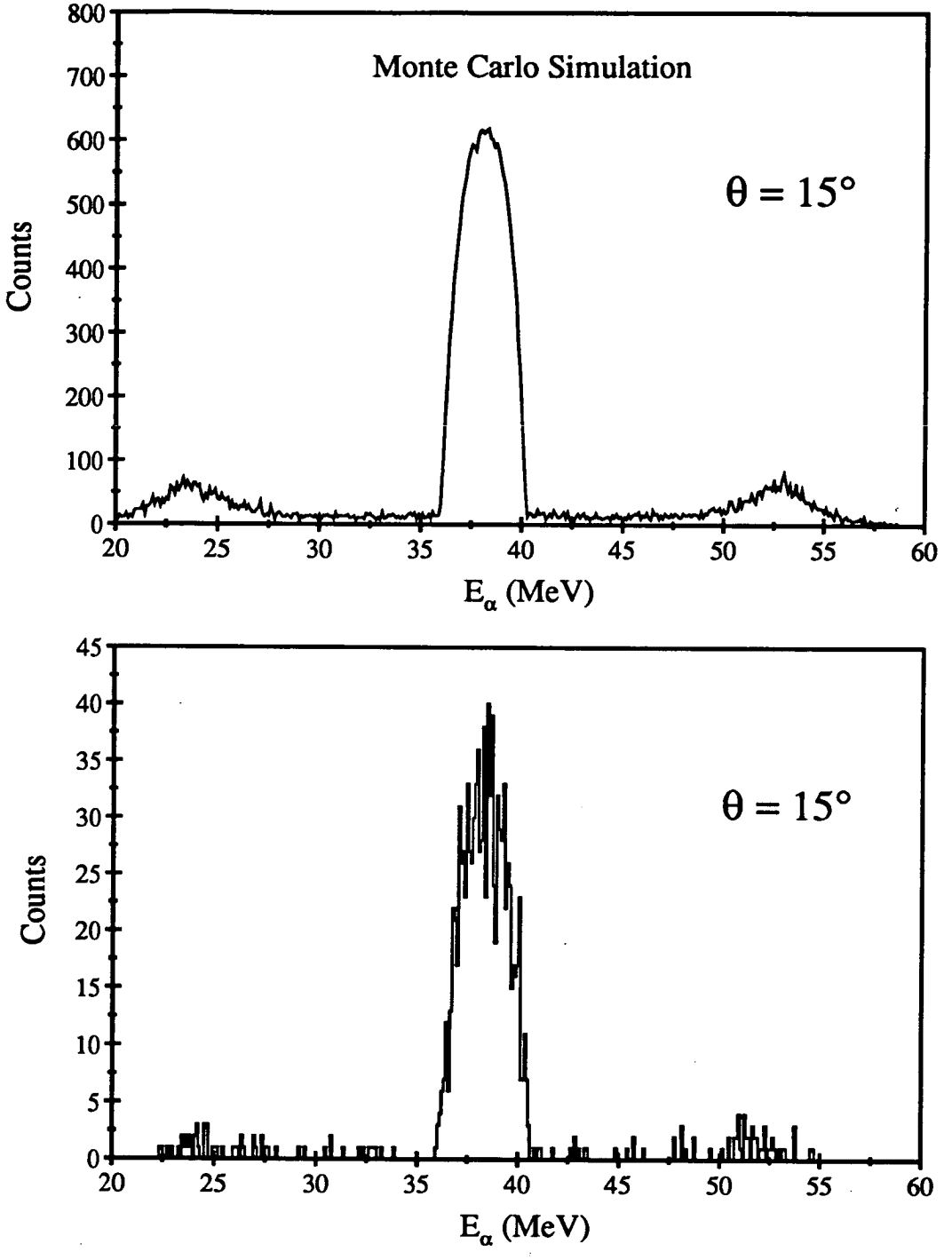

Figure 5.26: *The top figure shows a Monte Carlo simulation of the reaction* $^{120}Sn(^{7}Li, ^{8}Be_{g.s.,2.94} \rightarrow \alpha + \alpha)^{119}In_{g.s.,0.31}$. *The lower figure shows a projected energy spectrum of the data acquired for the reaction* $^{120}Sn(^{7}Li, \alpha + \alpha)^{119}In_{g.s.,0.31}$. *No data other than that which corresponds to a sequential reaction is observable.*

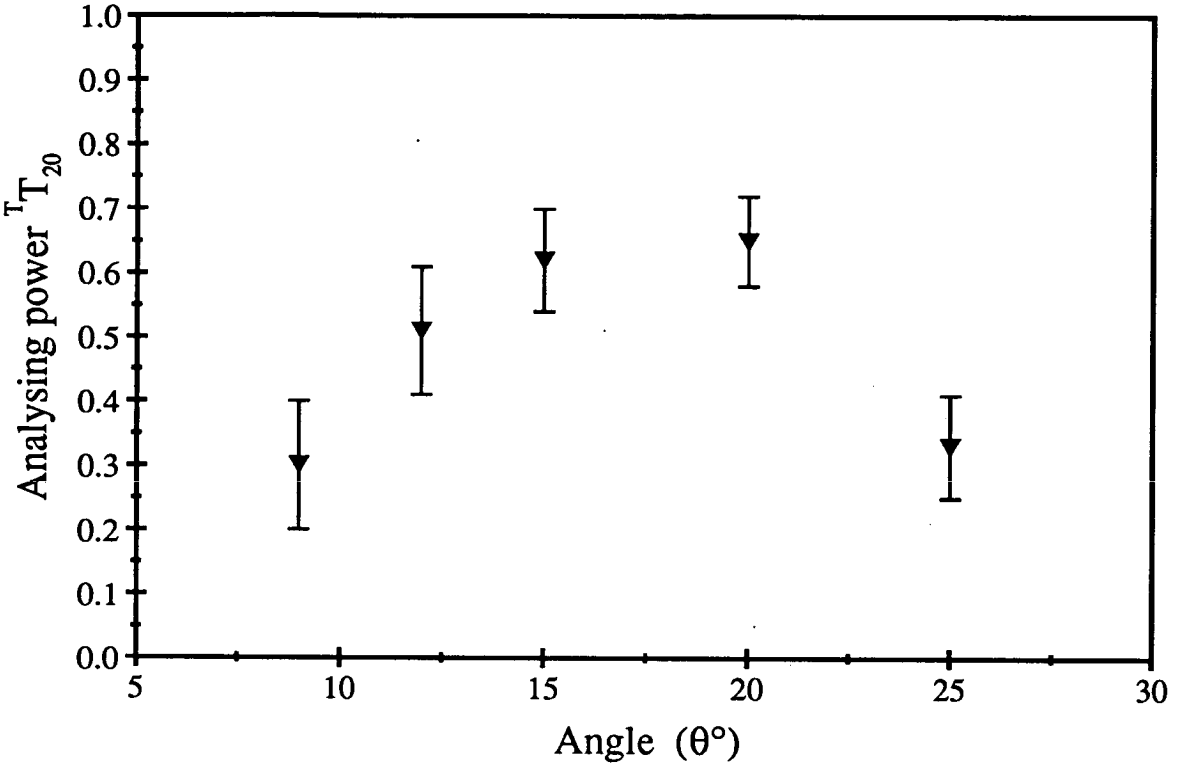

Figure 5.27: *The analysing powers* $^{T}T_{20}$ *for the reaction* $^{120}Sn(^{7}Li, ^{8}Be_{g.s.} \rightarrow \alpha + \alpha)^{119}In_{g.s.,0.31}$

This would increase the relative difference in the proximity of the two nuclei in the two phases thus increasing the analysing power. After $\sim 18°$ however $^{T}T_{20}$ starts to fall off. This occurs just before the grazing angle (21.3°) suggesting that the occurrence of nuclear overlap must now be allowed for. As the impact parameter decreases nuclear overlap will first occur in the phase where t_{20} is positive. The breakup cross section in this phase should therefore, with increasing angle beyond the grazing angle, initially decrease relative to that in the $-$ phase. This would account for the observed fall in the analysing power.

Cross sections

Differential cross sections were calculated for the reaction $^{120}Sn(^{7}Li, ^{8}Be_{g.s.} \rightarrow \alpha + \alpha)^{119}In_{g.s.,0.31}$. The data are shown in figure 5.28 along with the data of [Da87]. The trend in the data is seen to be the same except for an apparent

difference around 12°. The down turn at forward angles observable in the data of [Da87] is not observable in the present data set. It may be that as in the case of the sequential α, t coincidence data oscillations occur at forward angles and that none of the present data set happen to lie in the dip in the data. The difference in magnitude observed in the α, t and α, d coincidences cases is once again observable here.

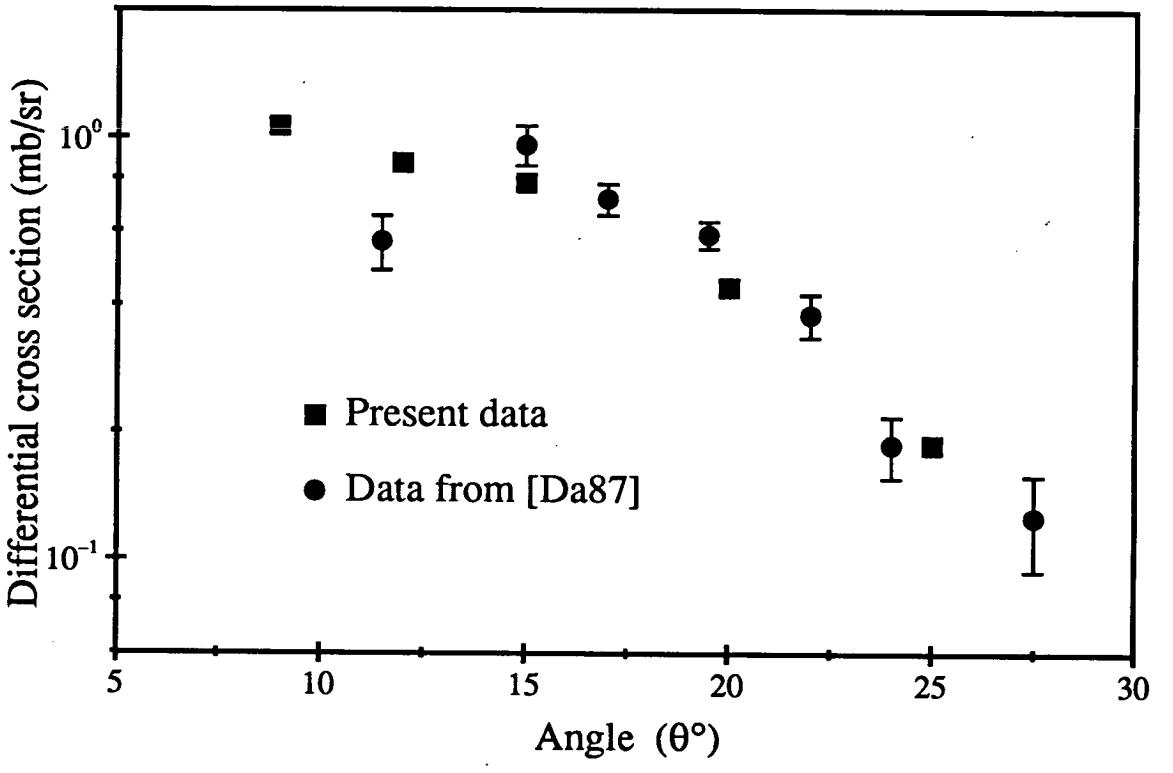

Figure 5.28: *Differential cross sections for the reaction* $^{120}Sn(^7Li, ^8Be_{g.s.} \rightarrow \alpha + \alpha)^{119}In_{g.s.,0.31}$

Chapter 6

Summary and Conclusion

This work was performed in order to investigate the mechanism involved in the direct breakup of ^7Li into an α and a t. The experiment used a polarized 70MeV ^7Li beam and a ^{120}Sn target. The motivation for performing this work came from the work of Shotter et al. [Sh81, Sh84] and Davinson [Da87]. They performed experiments with unpolarized beams using a number of targets including ^{120}Sn. Several attempts have been made to fit these data with varying degrees of success. Of all the calculations described in chapter 1 the only one that managed to describe the forward angle differential cross section data well when using a Coulomb interaction was the semi-classical calculation of Shotter et al. [Sh84]. At angles below the grazing angle one would expect the interaction in some degree at least to be Coulomb therefore any successful calculation must be able to include this interaction satisfactorially. The semi-classical Coulomb calculation used to determine differential cross sections does however possess certain limitations. The nuclear matrix elements required to describe the transitions were obtained from the data on the fusion reaction $\alpha(t,\gamma)^7Li$. This inclusion of experimental data in the calculation presents obvious difficulties. The determination of the experimental effective solid angles using a Monte Carlo code (see chapter 4) also requires a knowledge of the relative energy population function if relative energies are to be integrated over. This method was used in reference [Sh84].

The above considerations prompted the present work and the merits of po-

larized beams were exploited to provide a further test of the semi-classical model of breakup. Polarized beams are inherently better probes than unpolarized ones because the magnetic substate populations are not random and hence the effects of these states upon the reaction in question may be measured.

A semi-classical calculation for ${}^{T}T_{20}$ was described in chapter 2. It does not suffer from the limitations of the differential cross section calculation performed by Shotter et al. [Sh84] using the same formalism because for transitions depending on only one multipole λ, the transition matrix element is not required. A comparison of this calculation with the measured analysing powers for the direct breakup of ${}^{7}Li$ into an α and a t (see figure 5.11) shows that at angles 9°, 12° and 15° the data is consistent with the calculation. This shows that at these angles the direct breakup of ${}^{7}Li$ is a predominantly $\lambda = 1$ process which is consistent with a mainly Coulomb reaction. This work therefore supports the work of Shotter et al. that showed an agreement between the calculation and the differential cross section at 11.5°, but it also extends the agreement between the data and the semi-classical calculation to an angle of 15°. Additional confirmation of the agreement between the semi-classical calculation and the data was obtained by dividing the data into two relative energy bins. The calculation is not relative energy dependent and to within errors neither are the experimental analysing powers at angles 9°, 12° and 15°. It therefore appears that the direct breakup reaction of ${}^{7}Li$ is strongly Coulomb in nature between 9° and 15°. An unexplained feature of the data that occurs between 9° and 15° however is the reversal of the asymmetry observed in the projected energy spectra. It is not possible to simply explain this if a Coulomb interaction is the only one allowed for. This feature of the data is therefore in conflict with the evidence from the analysing power data because it cannot simply be accommodated by a Coulomb interaction even if final state interactions are allowed for. The results of this work therefore are not as conclusive as it was originally hoped they would be. In summary further evidence for the Coulomb nature of the breakup reaction has been provided by the analysing power data which has overcome many of the limitations of the cross section data. The

acquisition of data at smaller angles than has hitherto be achieved has however revealed the puzzling feature of the data commented upon above.

The analysing powers for the sequential breakup data $^{120}Sn(^{7}Li, ^{7}Li^{*}_{4.63} \rightarrow \alpha + t)^{120}Sn_{g.s.}$ disagreed with the semi-classical calculation at all angles. This does not support the observation of Shotter et al. [Sh89]. They found an agreement between their measured differential cross sections and their calculation at 11.5° and 15°. The origin of this difference may lie with the multipolarity of the transition concerned. The lowest possible multipolarity contributing to this transition is $\lambda = 2$. For such a transition any nuclear contribution might be expected to be more comparable to the Coulomb E2 contribution than in the case of a $\lambda = 1$ transition (see for example the DWBA calculation of Bertulani [Be91]). It is therefore possible that the nuclear contribution may be large enough to cause a discrepancy between the analysing power data and calculation, but not large enough to significantly affect the differential cross section data.

An understanding of the mechanism of the direct breakup of ^{7}Li is not only of interest in itself, but is also of astrophysical significance. The inverse i.e. fusion reaction $\alpha(t,\gamma)^{7}Li$ is an important nucleosynthetic reaction in the Big Bang Standard Model at low baryon densities. An accurate knowledge of its cross section is therefore important. The cross section must be deduced from the Coulomb part of the breakup of ^{7}Li as the reaction that is the inverse of the fusion reaction involves the absorption by ^{7}Li of a virtual photon.

If it can be established that an element's origin lies in the Big Bang then a great deal of information can be deduced from its present abundance. Of the elements heavier than A = 4 whose abundances cannot be explained by stellar processes ^{7}Li appears uniquely to have its origin in the Big Bang [Ro]. The origins of the other light elements (e.g. ^{6}Li, ^{9}Be etc.) may be explained by galactic cosmic ray spallation. The comparison of the observed abundance of ^{7}Li with that predicted by the standard model therefore provides a good test of the model. The abundances of various light elements particularly ^{4}He, may be used as tests of variations on the standard model. ^{7}Li however is unique in providing a test of the

existence or otherwise of primordial neutrino degeneracy [Bo85]. The abundances of light elements other than ^7Li could be consistent with several degenerate models, but because the production of ^7Li depends on the competition between several processes, one is able to exclude many sets of conditions that would otherwise be indistinguishable. An understanding of the breakup mechanism of ^7Li is thus seen to be of importance in more than just one field.

The extraction of the fusion cross section, σ_{fus} from the breakup data is however not entirely straight forward. The breakup cross section, given by

$$d\sigma(\varepsilon,\theta) = C\frac{\varepsilon}{E_\gamma^3}\sigma_{fus}(\varepsilon)df(\varepsilon,\theta) \tag{6.1}$$

apparently gives a simple way of determining σ_{fus}. However in order to use it the relative energy with which the breakup is associated must be known. The existence of final state interactions make this task difficult. The experimental relative energy, E_r, can only be deduced from the observed energies and angles of the α and t fragments. If equation 6.2, where $\cos\theta_{1-2}$ is the angle between the

$$E_{12} = \frac{m_2E_1 + m_1E_2 - 2(m_1m_2E_1E_2)^{1/2}\cos\theta_{1-2}}{m_1+m_2} \tag{6.2}$$

laboratory velocity vectors of the fragments, is used to determine E_r then any final state interactions causing the fragments to deviate from the orbitals followed at the point of breakup will result in $E_r \neq \varepsilon$. A recent calculation by Shotter et al. [Sh90, Sh91] which allows for final state interactions shows that E_r is shifted up in energy and has a finite width. This calculation assumes classical orbits, but the probability of the projectile breaking up at any particular position along its trajectory and the initial fragment separation are determined from the projectile's internal wavefunction. The subsequent calculation takes account of the three body nature of the final channel. Thus though at first sight the extraction of fusion cross sections from direct breakup data appears to be an excellent method of overcoming the difficulties of the direct measurement of σ_{fus}, final state interactions considerably complicate the matter.

In addition to data for the reaction $^{120}Sn(^{7}Li, \alpha + t)$ data was acquired for the reactions $^{120}Sn(^{7}Li, \alpha + d)^{121}Sn$ and $^{120}Sn(^{7}Li, \alpha + \alpha)^{119}In$. Calculations for the analysing powers for these reactions do not at present exist. The sign and perhaps the angular distribution can however be qualitatively understood in terms of the proximity of the nuclear surfaces in the two polarized phases. In the phase where the nuclear surfaces of the targets and the projectile are closest together, the transfer of a nucleon between the two nuclei is easier, resulting in a higher yield for this phase. This causes the analysing power $^{T}T_{20}$ to be positive. The increase in $^{T}T_{20}$ with increasing scattering angle, at angles less than the grazing angle, may also be explained in terms of nuclear surface proximities. As the impact parameter decreases with increasing scattering angle the change in distance between the target and the projectile in the two phases remains the same, but the average distance between the two nuclei decreases. The relative importance of the distance change in the two phases therefore increases, increasing the difference in yield between the two phases causing $^{T}T_{20}$ to increase so long as this simplistic model is applicable. The onset of a strong nuclear interaction at about the grazing angle initially causes a decrease in the breakup cross section in the + phase relative to the − one because of the greater nuclear overlap. This results in a decrease in the analysing power, with decreasing impact parameter, from its maximum just before the grazing angle.

6.1 Future Work

While the measurement of analysing powers has the advantage of eliminating most sources of systematic error they do possess larger statistical errors than differential cross sections for the same total number of counts. This disadvantage would not be a problem if it were not for the fact that data is required at small scattering angles where the count rate of elastically scattered ^{7}Li nuclei is high. The ΔE detectors cannot function properly at count rates much larger than $\sim 10^{4}$ counts/s. The maximum usable beam current is therefore set by the elastic scat-

tering. The most obvious method of overcoming this problem is to use magnetic spectrometers. In order to measure analysing powers in the way described in this thesis however one would require two spectrometers simultaneously at small angles. This is obviously fairly difficult to achieve. It is possible to measure ${}^{T}T_{20}$ using only one spectrometer by running two sequential situations which would be equivalent to having a detector set on one side of the beam and then moving it to the other side. This is achieved by rotating the polarization axis through an angle of 180° about the beam direction. This however is not a very practical method it is much easier to change phase than polarization axis. An alternative method would be run in three phase where two of the phases are polarized and one is unpolarized. These methods though would be subject to at least some of the systematic errors that the present setup eliminates (see section 5.4).

A different method of eliminating the elastic problem has been proposed by Shotter. The method involves the strategic use of a foil in front of the detectors to stop the elastics from reaching the detectors. A recent run at the NSF at Daresbury used a configuration that allowed a detector telescope to be placed at 0°. The foil placed in front of the detectors had a beam stop at its centre. A drawback to this method however is that low energy αs are stopped by the foil which results in only one kinematic solution being observable.

In the time available for the experiment discussed in this thesis it was only possible to measure the analysing power ${}^{T}T_{20}$. The measurement of other analysing powers such as T_{20}, T_{21} and iT_{11} as mentioned earlier is also desirable. The results of the semi-classical calculation described in section 2.5 are shown in figure 6.1. The calculation of these analysing powers requires a $\lambda = 1$ and a direct Coulomb assumption, therefore the agreement of any data with these calculations would be direct proof of the predominance of the Coulomb interaction. The determination of other analysing powers for the sequential α, t breakup at 15° would also be of interest. A recurrence of the difference in the analysing power found for the two peaks would prove that that its cause lay in the physics of the reaction.

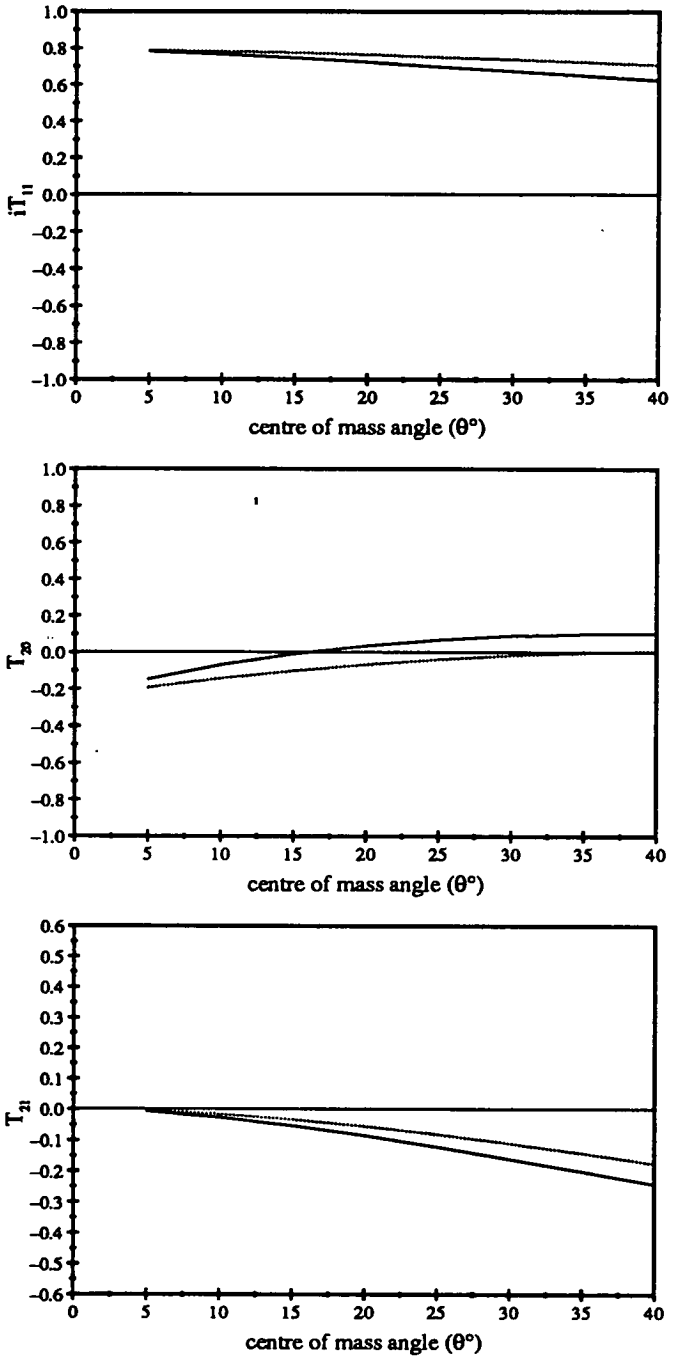

Figure 6.1: *The analysing powers T_{20}, T_{21} and iT_{11} for the direct breakup of ^7Li determined using the semi-classical calculation described in chapter 2. The solid line corresponds to a relative energy of 0MeV and the dotted to one of 2.16MeV.*

Appendix A

Data Tabulation

N.B. All quoted errors are statistical

A.1 Analysing power $^{T}T_{20}$

Data for the direct breakup reaction $^{120}Sn(^{7}Li, \alpha + t)^{120}Sn_{g.s.}$ at $E_{beam} = 70MeV$.

The diagram in figure 5.9 illustrates the gates used to obtain the analysing powers below.

All the direct data.

Angle ($\theta°$)	$^{T}T_{20}$ ($\varepsilon < 1.7$MeV)
9°	0.58 ± 0.08
12°	0.41 ± 0.07
15°	0.39 ± 0.08
20°	0.19 ± 0.11
25°	0.15 ± 0.15

Data divided into two relative energy gates.

Angle ($\theta°$)	${}^{T}T_{20}$ ($\epsilon < 0.8$MeV)	${}^{T}T_{20}$ ($\epsilon > 0.8$MeV)
9°	0.48 ± 0.12	0.70 ± 0.12
12°	0.36 ± 0.11	0.45 ± 0.10
15°	0.34 ± 0.13	0.43 ± 0.10
20°	−0.20 ± 0.19	0.37 ± 0.13
25°	0.04 ± 0.31	0.20 ± 0.17

High and low energy gates on the t spectrum illustrated in figure 5.9

Angle ($\theta°$)	${}^{T}T_{20}$ (low)	${}^{T}T_{20}$ (high)
9°	0.55 ± 0.14	0.64 ± 0.11
12°	0.35 ± 0.10	0.56 ± 0.10
15°	0.44 ± 0.10	0.35 ± 0.14
20°	0.28 ± 0.13	0.14 ± 0.23
25°	0.11 ± 0.18	0.23 ± 0.26

Data for the reaction $^{120}Sn(^{7}Li, {}^{7}Li^{*}_{4.63} \rightarrow \alpha + t)^{120}Sn_{g.s.}$ at $E_{beam} = 70$MeV.

All the sequential data.

Angle ($\theta°$)	${}^{T}T_{20}$
9°	0.67 ± 0.14
12°	—
15°	0.73 ± 0.10
20°	0.69 ± 0.08
25°	0.76 ± 0.08

Gates on separate sequential peaks in a t spectrum.

Angle ($\theta°$)	${}^{T}T_{20}$ (low)	${}^{T}T_{20}$ (high)
9°	0.60 ± 0.20	0.80 ± 0.20
12°	—	—
15°	0.99 ± 0.10	0.51 ± 0.10
20°	0.61 ± 0.11	0.83 ± 0.10
25°	0.71 ± 0.11	0.79 ± 0.11

Data for the reaction $^{120}Sn(^{7}Li, ^{6}Li^{*}_{2.18} \rightarrow \alpha + d)^{121}Sn_{g.s.,0.06}$ at $E_{beam} = 70MeV$.

All the data.

Angle ($\theta°$)	${}^{T}T_{20}$
9°	0.47 ± 0.15
12°	0.32 ± 0.14
15°	0.62 ± 0.10
20°	0.41 ± 0.09
25°	0.34 ± 0.09

Gates on seperate sequential peaks in a d spectrum.

Angle ($\theta°$)	${}^{T}T_{20}$ (low)	${}^{T}T_{20}$ (high)
9°	0.21 ± 0.24	0.52 ± 0.18
12°	0.27 ± 0.22	0.35 ± 0.17
15°	0.49 ± 0.15	0.68 ± 0.14
20°	0.60 ± 0.13	0.26 ± 0.13
25°	0.43 ± 0.14	0.30 ± 0.12

Data for the reaction $^{120}Sn(^{7}Li, ^{8}Be_{g.s.} \rightarrow \alpha + \alpha)^{119}In_{g.s.,0.31}$ at E_{beam} = 70MeV.

Angle ($\theta°$)	$^{T}T_{20}$
9°	0.30 ± 0.10
12°	0.51 ± 0.10
15°	0.62 ± 0.08
20°	0.65 ± 0.07
25°	0.33 ± 0.08

A.2 Differential cross sections

Data for the direct breakup reaction $^{120}Sn(^{7}Li, \alpha + t)^{120}Sn_{g.s.}$ at E_{beam} = 70MeV.

Angle ($\theta°$)	$d\sigma/d\Omega$ (mb/sr)
9°	9.88 ± 0.27
12°	10.40 ± 0.25
15°	5.77 ± 0.15
20°	1.812 ± 0.06
25°	0.50 ± 0.02

Data for the reaction $^{120}Sn(^{7}Li, ^{7}Li^{*}_{4.63} \rightarrow \alpha + t)^{120}Sn_{g.s.}$ at E_{beam} = 70MeV.

Angle ($\theta°$)	$d\sigma/d\Omega$ (mb/sr)
9°	14.1 ± 0.6
12°	2.3 ± 0.2
15°	12.3 ± 0.4
20°	9.3 ± 0.2
25°	4.0 ± 0.1

Data for the reaction $^{120}Sn(^{7}Li, ^{6}Li^{*}_{2.18} \rightarrow \alpha + d)^{121}Sn_{g.s.,0.06}$ at E_{beam} = 70MeV.

Angle ($\theta°$)	$d\sigma/d\Omega$ (mb/sr)
9°	3.57 ± 0.20
12°	2.90 ± 0.16
15°	3.00 ± 0.12
20°	1.91 ± 0.07
25°	0.80 ± 0.03

Data for the reaction $^{120}Sn(^{7}Li, ^{8}Be_{g.s.} \rightarrow \alpha + \alpha)^{119}In_{g.s.,0.31}$ at E_{beam} = 70MeV.

Angle ($\theta°$)	$d\sigma/d\Omega$ (mb/sr)
9°	1.06 ± 0.04
12°	0.87 ± 0.04
15°	0.78 ± 0.02
20°	0.44 ± 0.01
25°	0.187 ± 0.005

References

[Al] K.Alder and A.Winther *Electromagnetic excitations* North-Holland Publishing Company, 1975.

[Am79a] H.Amakowa, S.Yamaji, A.Mori and K.Yazaki *Physics Letters* **82B** (1979) 13

[Am79b] H.Amakowa, K.Yazaki *Physics Letters* **87B** (1979) 159

[Am81] H.Amakowa, A.Mori, H.Nishioka, K.Yazaki and S.Yamaji *Physical Revew C* **23** (1981) 583

[Ba76] G.Baur and D.Trautman *Physics Reports* **25C** (1976) 293

[Ba84] G.Baur, F.Rosel and D.Trautmann *Physics Reports* **111,No.5** (1984) 333

[Be91] C.A.Bertulani and M.S.Hussein *Nuclear Physics* **A524** (1991) 306

[Bi82] A.N.Bice, A.C.Shotter and J.Cerny *Nuclear Physics* **A390** (1982) 161

[Bl] J.M.Blatt and V.F.Weisskopf *Theoretical Nuclear Physics* Publishers John Wiley & son 1962

[Bh81] B.K.Bhowmik, E.C.Pollacco, N.E.Sanderson, J.B.A.England and G.C.Morrison *Nuclear Physics* **A363** (1981) 516

[Bo85] A.M.Boesgaard and G.Steigman *Annual Reviews of Astronomy and Astrophysics* **23** (1985) 319

[Br] D.M.Brink and G.R.Satchler *Angular Momentum* Clarendon Press, OUP, 1975.

[Ca80] C.M.Castaneda *Physical Review C* **21** (1980) 179

[Da] S.E.Darden
Proceedings of the third international symposium on polarization phenomena in nuclear reactions. Eds H.H. Barchall and W.Haeberli. University of Winsconsin Press Madison 1970.

[Da87] T.Davinson Ph.D. thesis Edinburgh University (1987) unpublished

[de] A.deShalit and h.Feshbach *Theoretical Nuclear Physics, Volume1: Nuclear Structure* John Wiley & Sons, Inc., 1974

[Dr81] J.van Driel, S.Gonggrijp, R.V.F.Janssens, R.H.Siemssen, K.Siwek-Wilczynska and J.Wilczynski *Physics Letters* **98B** (1981) 351

[El] A.El-Lithi Fortran77 code DFVALUE unpublished

[En] J.B.A.England *Techniques in Nuclear Structure Physics* The MacMillan Press Ltd, 1974.

[Fu82] H.Fuchs *Nuclear Instruments and Methods* **200** (1982) 361

[Fu83] T.Fukuda, M.Ishihara, M.Tanaka, H.Ogata, I.Miura, M.Inoue, T.Shimoda, K.Katori and S.Wakayama *Physical Review C* **27** (1983) 2029

[Gl80] C.W.Glover, R.I.Cutler and K.W.Kemper *Nuclear Physics* **A341** (1980) 137

[Go84] P.B.Goldhoorn, G.J.Balster, H.J.Koeslag, R.J.de Meijer, R.H.Siemssen, Z.Sujkowcki and H.W.Wilschut *Physics Letters* **142** (1984) 14

[He47] A.C.Helmholtz, E.M.McMillan and D.C.Sewell *Physical Review* **72** (1947) 1003

[Ja73] L.Jarczyk, J.Lang, R.Müller, D.Balszer, P.Viatte and P.Marmier *Physical Review C* **8** (1973) 68

[Jo] R.C.Johnson
Invited papers of the 4th international conference on clustertering aspects of nuclear structure and nuclear reactions. Eds J.S.Lilly and M.A.Nagarajan. D.Reidel Publishing Company 1984.

[Jo70] R.C.Johnson and P.J.R.Soper *Physical Review C* **1** (1970) 976

[Jo88] R.C.Johnson private communication (see page 138 for short note).

[Ka89] O.Karban, W.C.Hardy K.A.Connell, S.E.Darden, C.O.Blyth, H.D. Choi, S.T.Hall, S.Roman and G.Tungate *Nuclear Instruments and Methods* **A274** (1989) 4

[Kl81] J.Klienfeller, J.Bisplinghoff, J.Ernst, T.Mayer-Kuckuk, G.Baur, B. Hoffman, R.Shayam, F.Rösel and D.Trautmann *Nuclear Physics* **A370** (1981) 205

[Kr84] D.Krämer, K.Becker, K.Blatt, R.Čaplar, D.Fick H.Gemmeke, W. Haeberli, H.Jänsch, O.Karban, L.Luh, K.-H.Möbius, V.Nečas, W.Ott, M.Tanaka, G.Tungate, I.M.Turkiewicz, A.Weller, and E.Steffens *Nuclear Instruments and Methods* **220** (1984) 123

[Ma] Madison Covention
Proceedings of the third international symposium on polarization phenomena in nuclear reactions. Eds H.H. Barchall and W.Haeberli. University of Winsconsin Press Madison 1970.

[Ma78] N.Matsuoka, A.Shimizu, K.Hosono, T.Saito, M.Kondo, H.Sakaguchi, Y.Toba, A.Goto, F.Ohtani and N.Nakanishi *Nuclear Physics* **A311** (1978) 173

[Ma80] N.Matsuoka, A.Shimizu, K.Hosono, T.Saito, M.Kondo, H.Sakaguchi, A.Goto and F.Ohtani *Nuclear Physics* **A337** (1980) 269

[Ma82] N.Matsuoka, K.Hatanaka, T.Saito, T.Itahashi, K.Hosono, A.Shimuzu, M.Kondo, F.Ohani and O.Cynshi *Nuclear Physics* **A391** (1982) 357

[Ma88] E.W.Macdonald Ph.D. thesis Edinburgh University (1988) unpublished

[Ma89] E.W.Macdonald private communication

[Me] A.Messiah *Quantum Mechanics* Publishers North-Holland Publishing Company (1966)

[Me85] R.J.Meijer and R.Kamermans *Reviews of Modern Physics* **57** (1985) 147

[Na82] M.A.Nagarajan, I.J.Thompson and R.C.Johnson *Nuclear Physics* **A385** (1982) 525

[Ne82] B.Neumann, H.Rebel, H.J.Gils, R.Planeta, J.Buschmann, H.Klewe-Nebenius, S.Zagromski, R.Shyam and W.Machiner *Nuclear Physics* **A382** (1982) 296

[Op35a] J.R.Oppenheimer *Physical Review* **47** (1935) 845

[Op35b] J.R.Oppenheimer and M.Phillips *Physical Review* **48** (1935) 500

[Os74] R.Ost, K.Bethge, H.Gemmeke, L.Lassen and D.Scholtz *Zeitschrift für Physik* **A266** 369

[Ot76] D.F.Ottewell Ph.D. thesis University of British Columbia (1976) unpublished

[Pa78] J.Pampus *Nuclear Physics* **A311** (1978) 141

[Ra81] W.D.Rae, A.J.Cole, A.Dacal, R.Legrain, B.G.Harvey, J.Mahoney, M.J.Murphy, R.G.Stokstad and I.Tserruya *Physics Letters* **105B** (1981) 417

[Ro] C.E.Rolfs and W.S.Rodney *Cauldrons in the Cosmos: Nuclear Astrophysics* The University of Chicago Press, Ltd, 1988

[Sa78] G.R.Satchler *Physics Letters* **76B** (1978) 23

[Sa79a] G.R.Satchler and W.G.Love *Physics Report* **55** (1979) 183

[Sa79b] G.R.Satchler *Physics Letters* **83B** (1979) 284

[Sa83] Y.Sakuragi, M.Yahiro and M.Kamimura *Progress in Theoretical Physics* **70** (1983) 1047

[Sa86] Y.Saguraki, M.Yahiro and M.Kamimura *Progress of Theoretial Physics Supplement* **89** (1986) 136

[Sc77] D.Schotz, H.Gemmeke, L.Lassen, R.Ost, and K.Bethge *Nuclear Physics* **A288** (1977) 351

[Se47] R.Serber *Physical Review* **72** (1947) 1008

[Sh80] R.Shayam *Physical Review C* **22** (1980) 1401

[Sh81] A.C.Shotter, A.N.Bice, J.M.Wouters, W.D.Rae and J.Cerny *Physical Review Letters* **46** (1981) 12

[Sh83] R.Shyam, G.Baur, A.Budzanowski, J. Bojowald, H. Dabrowski, G. Mayer-Böricke, W.Oelert, G.Riepe, M.Rogge, P.Turek, F.Rösel and D.Trautmann *Physical Review C* **27** (1983) 2393

[Sh84] A.C.Shotter, V.Rapp, T.Davinson, and D.Branford *Physical Review letters* **53** (1984) 1539

[Sh88a] A.C.Shotter, V.Rapp, T.Davinson, and D.Branford *Journal of Physics G* **14** (1988) L169

[Sh88b] A.C.Shotter amd M.A.Nagaragian *Journal of Physics G* **14** (1988) L109

[Sh89] A.C.Shotter *Journal of Physics G* **15** (1989) L41

[Sh90] Biennial Report of the Edinburgh Nuclear Physics Group 1989/90

[Sh91] A.C. Shotter private communication

[Si] M.Simonius *Lecture Notes in Physics* vol. 30 ed. D.Fick Publishers Springer, Berlin

[Si79] K.Siwek-Wilczynska, E.H.Du Marrchie van Voorthuysen, J.van Popta, R.H.Siemssen and J.Wilczynski *Nuclear Physics* **A330** (1979) 150

[St77] E.Steffens, W.Dreves, P.Egelhof, D.Kasen, W.Weiss, P.Zupranski and D.Fick *Revue de Physique Appliquée* **12** (1977) 1567

[Th81] I.J.Thompson and M.A.Nagaragan *Physics Letters* **106B** (1981) 163

[Th83] I.J.Thompson and M.A.Nagaragan *Physics Letters* **123B** (1983) 379

[Ut88] H.Utsunomiya, R.P.Schmitt, Y.-W.Lui, D.R.Haenni, H.Dejbakhsh, L.Cooke, P.Heimberg, A.Ray, T.Tamura and T.Udagawa *Physics Letters* **211B** (1988) 24

[Ut90] H.Utsunomiya, Y.-W.Lui, L.Cooke, H.Dejbakhsh, D.R.Haenni, P. Heimberg, A.Ray, B.K.Srivastava, R.P.Schmitt and T.Udagawa *Nuclear Physics* **A511** (1990) 379

[Ya81] M.Yahiro and M.Kamimura *Progress in Theoretical Physics* **65** (1981) 2046,2051

[Ya82] M.Yahiro, M.Nakano, Y.Iseri and M.Kamimura *Progress in Theoretical Physics* **67** (1982) 1467

[Yo87] J.Yorkston, A.C.Shotter, D.B.Syme and G.Huxtable *Nuclear Instruments and Methods* **A262** (1987) 353

[Yo89] J.Yorkston Ph.D. thesis Edinburgh University (1989) unpublished

[Zu79] P.Zupranski, W.Dreves, P.Egelhof, E.Steffens and D.Fick *Nuclear Instruments and Methods* **169** (1979) 193

[1]In the quoted communication the following argument is advanced. The predicted finite value of ${}^{T}T_{20}$ at 0° appears at first sight to be incorrect. At 0° one cannot define a reaction plane therefore defining a direction with respect to a reaction plane is not possible. This would imply that the yields for the two polarized phases would tend to the same value. If this value was finite ${}^{T}T_{20}$ ($\sigma_+ - \sigma_-/(\sigma_+ + \sigma_-)$) should also tend to zero. If one however notes that the unpolarized differential cross section is predicted to be zero at 0° then it becomes apparent that a paradox does not exist. The sum of the polarized yields is equal to the unpolarized yield. If this tends to zero then as the yields must be real and positive the difference must also tend to zero. If the measured intensities which must be used to determine ${}^{T}T_{20}$ go to zero as $\theta \rightarrow 0$ then it is not possible to determine ${}^{T}T_{20}$. The semi-classical theory is therefore valid for all angles as $\theta \rightarrow 0$, but cannot be used for $\theta = 0$.